JuLI™ Stage paper references

LS Technical Sales

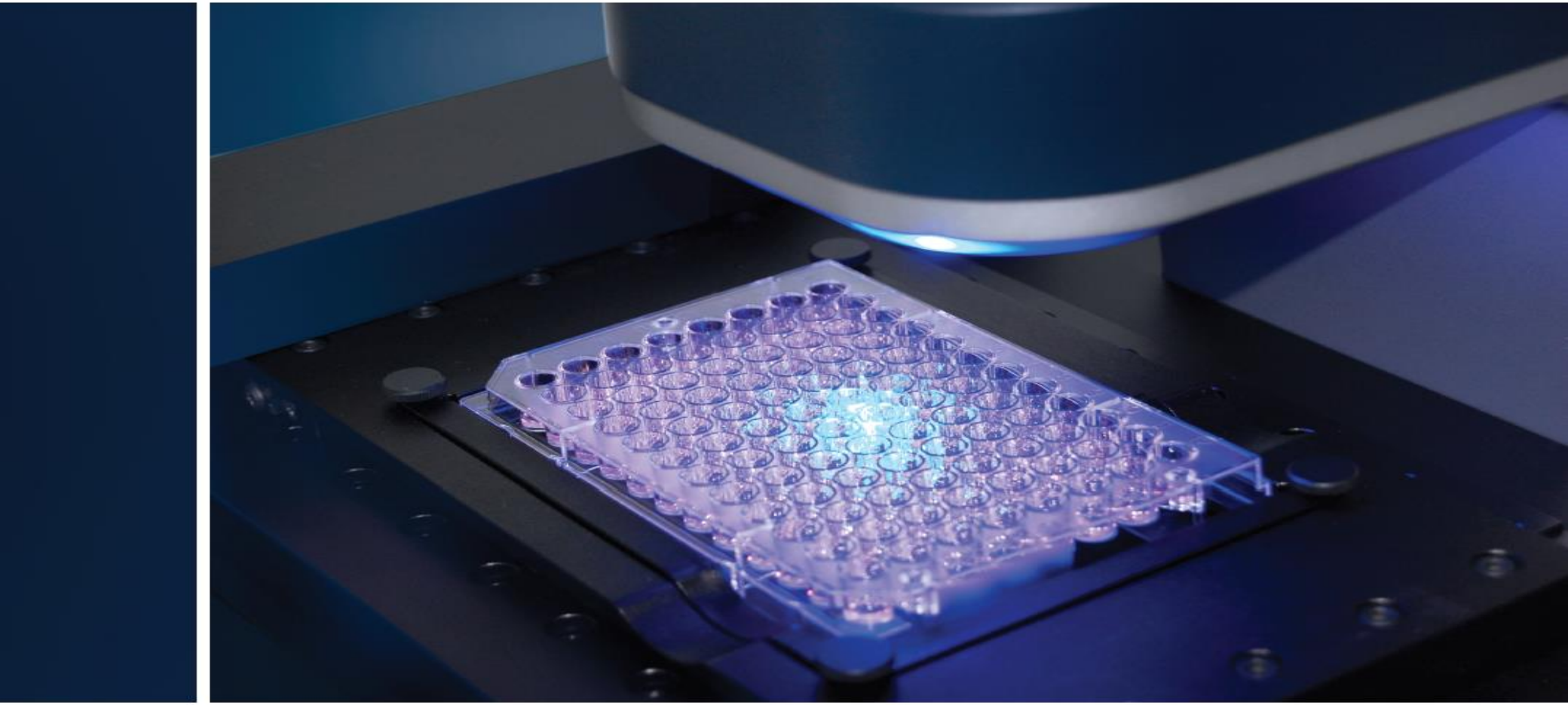

NanoEnTek

www.impactjournals.com/oncotarget/ Oncotarget, Vol. 6, No. 34

Deubiquitinating enzyme USP37 regulating oncogenic function of 14-3-3γ

Jin-Ock Kim[1], So-Ra Kim[1], Key-Hwan Lim[1], Jun-Hyun Kim[1], Brijesh Ajjappala[1], Hey-Jin Lee[1], Jee-In Choi[2], Kwang-Hyun Baek[1]

[1]Department of Biomedical Science, CHA University, Bundang CHA Hospital, Gyeonggi-Do 463-400, Republic of Korea
[2]Department of Rehabilitation Medicine, CHA University, Bundang CHA Hospital, Gyeonggi-Do 463-400, Republic of Korea

Correspondence to:
Kwang-Hyun Baek, **e-mail:** baek@cha.ac.kr

Keywords: *14-3-3, cell proliferation, deubiquitinating enzyme, ubiquitin-specific protease*

Received: *May 27, 2015* ***Accepted:*** *September 14, 2015* ***Published:*** *September 25, 2015*

ABSTRACT

14-3-3 is a family of highly conserved protein that is involved in a number of cellular processes. In this study, we identified that the high expression of 14-3-3γ in various cancer cell lines correlates with the invasiveness of the cancer cells. Overexpression of 14-3-3γ causes changes to the morphologic characteristics of cell transformation, and promotes cell migration and invasion. The cells overexpressed with 14-3-3γ have been shown to stimulate foci and tumor formation in SCID-NOD mice in concert with signaling components as reported with the 14-3-3β. In our previous study, we demonstrated that 14-3-3γ inhibits apoptotic cell death and mediates the promotion of cell proliferation in immune cell lines. Earlier, binding partners for 14-3-3γ were defined by screening. We found that USP37, one of deubiquitinating enzymes (DUBs), belongs to this binding partner group. Therefore, we investigated whether 14-3-3γ mediates proliferation in cancer cells, and 14-3-3γ by USP37 is responsible for promoting cell proliferation. Importantly, we found that USP37 regulates the stability of ubiquitin-conjugated 14-3-3γ through its catalytic activity. This result implies that the interactive behavior between USP37 and 14-3-3γ could be involved in the regulation of 14-3-3γ degradation. When all these findings are considered together, USP37 is shown to be a specific DUB that prevents 14-3-3γ degradation, which may contribute to malignant transformation via MAPK signaling pathway, possibly providing a new target for therapeutic objectives of cancer.

INTRODUCTION

Ubiquitination of proteins through the ubiquitin-proteasome pathway (UPP) is an important post-translational modification (PTM) involved in regulating the levels of most cellular proteins and eliminating misfolded proteins. PTM by ubiquitin plays an important role in a variety of cellular functions [1–3]. Protein ubiquitination is mediated by sequential enzymatic actions via ubiquitin-activating enzymes (E1), ubiquitin-conjugating enzymes (E2), and ubiquitin ligases (E3). An ubiquitination factor, (E4), which is required for efficient polyubiquitination, has been identified in yeast [4, 5]. Throughout these processes, targeted proteins are directed toward ATP-dependent hydrolysis by the 26S proteasome [6]. Deubiquitination, the reversal process of ubiquitination, is catalyzed by deubiquitinating enzymes (DUBs), which remove ubiquitin from conjugated target proteins [1, 5, 7]. The human genome codes for approximately 100 DUBs. Most DUBs are cysteine proteases, and they are classified into at least six families [8, 9].

A broad range of organisms and tissues contain 14-3-3 proteins. They have many diverse functions, including central roles in the signal transduction pathway, exocytosis, anti-apoptotic process, and cell cycle regulation. Many signaling pathways involving 14-3-3 proteins are overactivated during tumorigenesis, indicating that these proteins can bind to a number of target proteins altered in various types of cancer involving

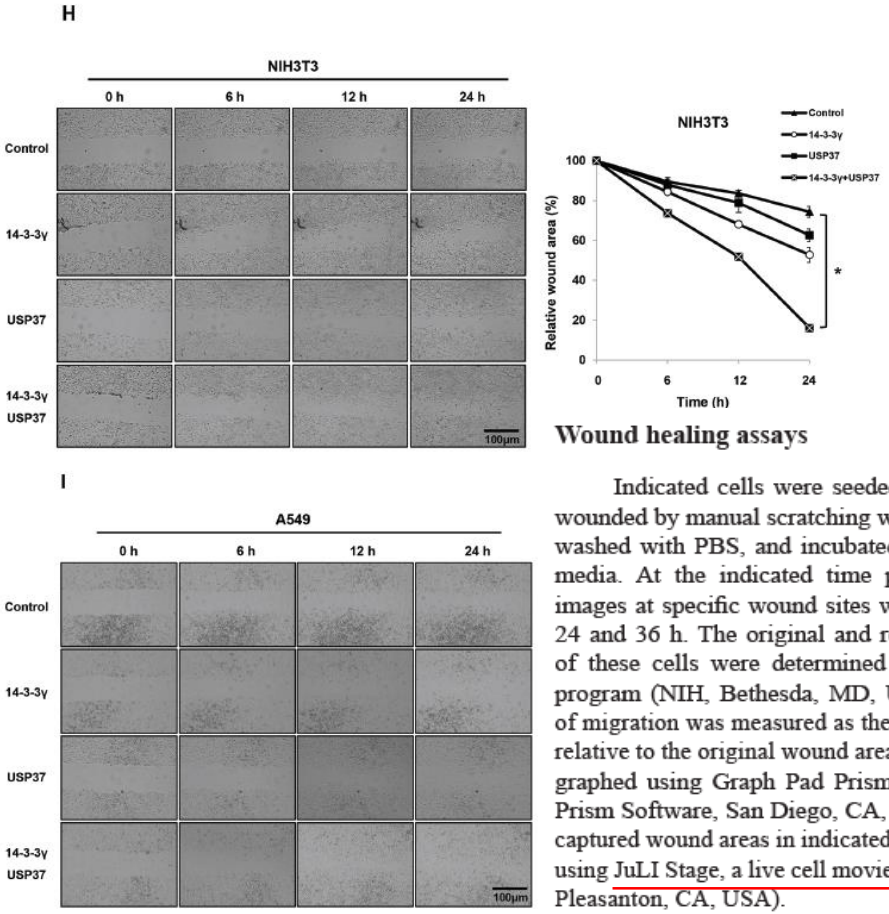

Figure 5: (*Continued*) USP37 promoted cell viability and proliferation by stabilizing 14-3-3γ. H and I. Stably transfected NIH3T3 cells with their respective constructs were used for investigating 14-3-3γ and USP37-mediated migratory and invasive potential in a wound-healing assay. The wound healing by migrated cells at 0, 6, 12 and 24 h was imaged with the JuLI Stage system (NanoEnTek, Pleasanton, CA, USA). The data are representative of four biological replicates. The percentage of the wound area was graphed using Graph Pad Prism Software. The data were presented as means ± s.d. * $P < 0.01$, $n = 4$. Scale bar = 200 μm.

Wound healing assays

Indicated cells were seeded in 6-well plates and wounded by manual scratching with 200 μl pipette tips, washed with PBS, and incubated at 37°C in complete media. At the indicated time points, phase contrast images at specific wound sites were captured at 0, 12, 24 and 36 h. The original and recovered wound areas of these cells were determined by Image J software program (NIH, Bethesda, MD, USA). The percentage of migration was measured as the recovered wound area relative to the original wound area. Tumor volumes were graphed using Graph Pad Prism program (Graph Pad Prism Software, San Diego, CA, USA). In addition, we captured wound areas in indicated cells at 0, 12, and 24 h using JuLI Stage, a live cell movie analyzer (NanoEnTek, Pleasanton, CA, USA).

Dose enhancement and cytotoxicity of gold nanoparticles in colon cancer cells when irradiated with kilo- and mega-voltage radiation

Herman Hau[a*], Dipesh Khanal[a*], Linda Rogers[b], Natalka Suchowerska[b,c], Rajiv Kumar[d], Srinivas Sridhar[d], David McKenzie[c,e], Wojciech Chrzanowski[a,d,e#]

[a]Faculty of Pharmacy, The University of Sydney, NSW 2006, Australia

[b]Chris O'Brien Lifehouse, Sydney, NSW 2006, Australia

[c]School of Physics, The University of Sydney, NSW 2006, Australia

[d]Nanomedicine Science and Technology Center and Department of Physics, Northeastern University, Boston, Massachusetts, USA

[e]Charles Perkins Centre, The University of Sydney, NSW 2006, Australia

*Authors contributed equally to this work

Correspondence to: Wojciech Chrzanowski, PhD, DSc

Address: University of Sydney, Faculty of Pharmacy, Pharmacy and Bank Building, A15 Science Road, University of Sydney, Sydney, NSW, Australia 2006

Email: wojciech.chrzanowski@sydney.edu.au

Abstract

Despite major advances in the field of radiotherapy, healthy tissue damage continues to constrain the dose that can be prescribed in cancer therapy. Gold nanoparticles have been proposed as a solution to minimise radiation associated toxicities by enhancing the radiation dose delivered locally to tumour cells. In the current study, we investigated the application of third generation gold nanoparticles in 2D and 3D cell culture and whether there is synergy between the nanoparticles and kilo- or mega-voltage radiation to cause augmented cytotoxicity. The 10 nm gold nanoparticles were found to be non-toxic in both 2D and 3D *in vitro* cultures of colon cancer cells at concentrations of up to 10 - 25 µg/mL. There was a significant increase in cell survival fraction reduction following exposure to 1 Gy of kilo-voltage (18.3%) and 2 Gy of mega-voltage (35.3%) radiation when the cells were incubated with 50 µg/mL of gold nanoparticles. The biocompatibility of the gold nanoparticles combined with their substantial synergy with radiation encourages further investigations into their application in targeted cancer treatment.

Keywords: gold nanoparticles, magnetic levitation, radiation dose enhancement, 3D cell culture, colon cancer

3D spheroid assay

The assay was carried out as previously outline[25]. Briefly, the Nanoshuttle® treated LOVO cells were levitated with neodymium magnets overnight to form aggregated 3D clusters. A cell density of 1 x 10^5 cells per well was seeded to an ultralow attachment 96 well plate placed on top of a 96 well dot shaped magnetic drive and proceeded as per the migration assay. The phase images of the spheroids after 24 hrs at each concentration were captured using the JuLi Stage (NanoEnTek, Seoul, Korea).

Drug Design, Development and Therapy

Dovepress
open access to scientific and medical research

Open Access Full Text Article

ORIGINAL RESEARCH

Real-time monitoring of cisplatin cytotoxicity on three-dimensional spheroid tumor cells

This article was published in the following Dove Press journal:
Drug Design, Development and Therapy
4 July 2016
Number of times this article has been viewed

NamHuk Baek[1,*]
Ok Won Seo[1,*]
Jaehwa Lee[1]
John Hulme[2]
Seong Soo A An[2]

[1]Department of Research and Development, NanoEntek Inc., Seoul, [2]Department of BioNano Technology, Gachon University, Gyeonggi-do, Korea

*These authors contributed equally to this work

Video abstract

Point your SmartPhone at the code above. If you have a QR code reader the video abstract will appear. Or use: http://youtu.be/dgkkEmTeKkU

Correspondence: Seong Soo A An
Department of BioNano Technology, Gachon Medical Research Institute, Gachon University, 1342 Sungnam Daero, Sungnamsi 461-701, Korea
Tel +82 31 750 8755
Fax +82 31 750 8755
Email seongsan@gachon.ac.kr

Abstract: Three-dimensional (3D) cell cultivation is a powerful technique for monitoring and understanding diverse cellular mechanisms in developmental cancer and neuronal biology, tissue engineering, and drug development. 3D systems could relate better to in vivo models than two-dimensional (2D) cultures. Several factors, such as cell type, survival rate, proliferation rate, and gene and protein expression patterns, determine whether a particular cell line can be adapted to a 3D system. The 3D system may overcome some of the limitations of 2D cultures in terms of cell–cell communication and cell networks, which are essential for understanding differentiation, structural organization, shape, and extended connections with other cells or organs. Here, the effect of the anticancer drug cisplatin, also known as cis-diamminedichloroplatinum (II) or CDDP, on adenosine triphosphate (ATP) generation was investigated using 3D spheroid-forming cells and real-time monitoring for 7 days. First, 12 cell lines were screened for their ability to form 3D spheroids: prostate (DU145), testis (F9), embryonic fibroblast (NIH-3T3), muscle (C2C12), embryonic kidney (293T), neuroblastoma (SH-SY5Y), adenocarcinomic alveolar basal epithelial cell (A549), cervical cancer (HeLa), HeLa contaminant (HEp2), pituitary epithelial-like cell (GH3), embryonic cell (PA317), and osteosarcoma (U-2OS) cells. Of these, eight cell lines were selected: NIH-3T3, C2C12, 293T, SH-SY5Y, A549, HeLa, PA317, and U-2OS; and five underwent real-time monitoring of CDDP cytotoxicity: HeLa, A549, 293T, SH-SY5Y, and U-2OS. ATP generation was blocked 1 day after addition of 50 µM CDDP, but cytotoxicity in HeLa, A549, SH-SY5Y, and U-2OS cells could be visualized only 4 days after treatment. In 293T cells, CDDP failed to kill entirely the culture and ATP generation was only partially blocked after 1 day. This suggests potential CDDP resistance of 293T cells or metabolic clearance of the drug. Real-time monitoring and ATP measurements directly confirmed the cytotoxicity of CDDP, indicating that CDDP may interfere with mitochondrial activity.

Keywords: cisplatin, real-time monitoring, cytotoxicity, 3D spheroids, ATP productions

Introduction

Cells are usually grown as two-dimensional (2D) cultures, which are reliable and convenient for the majority of developmental biology, tissue engineering, tissue formation, disease mechanism, drug development, and especially large-scale therapeutic protein production studies.[1] The recent development of three-dimensional (3D) culture systems has offered a model closer to in vivo conditions and promised to advance our understanding of cell survival, proliferation, differentiation, and gene and protein expression.[2] Morphological and other properties exhibited by cells in 3D cultures may be better suited for studies of structural organization, cell–cell communication, cell–extracellular matrix interaction, drug sensitivity, cell death, cancer cell survival, and neighboring cell networks.[3] The ensuing results could have a profound influence on studies in cancer biology, drug toxicity tests, stem cell applications, and

Materials and methods

Materials

The following cell lines were obtained from NanoEnTek Inc. (Seoul, Korea): prostate (DU145), testis (F9), embryonic fibr
ney
alve
HeL
(GH
Dull
Park
(FB
buff
0.05
red
Inc.
micr
Wal
micr
used
were
Cell
cell
mea
ratio

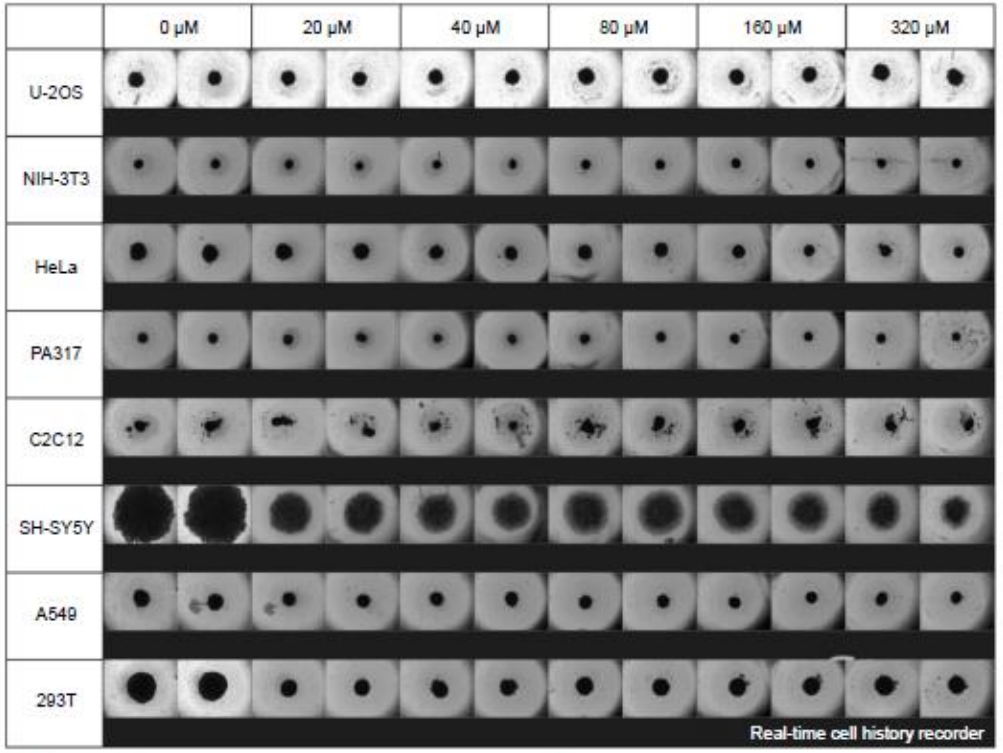

Figure 2 Compiled still shot photos of eight cell lines after 7 days from the treatment with cisplatin.
Note: Cell lines are NIH-3T3, C2C12, 293T, SH-SY5Y, A549, HeLa, PA317, and U-2OS in 96-well plates.

monitored using the JuLI Stage real-time cell history recorder (NanoEnTek). 3D cell viability was measured using the Infinite Elisa Reader (Tecan Trading AG., Männedorf, Switzerland).

All cells were commercially available, approval from the ethics committee therefore, was not required.

Identification and validation of compounds selectively killing resistant cancer: delineating cell line specific effects from P-glycoprotein-induced toxicity

András Füredi [a†], Szilárd Tóth [a†], Kornélia Szebényi [b], Veronika F.S. Pape [a], Dóra Türk [a], Nóra Kucsma [a], László Cervenák[c], József Tóvári [d] and Gergely Szakács [a,b]*

[a] Institute of Enzymology, Research Centre for Natural Sciences, Hungarian Academy of Sciences, Magyar Tudósok körútja 2, H-1117 Budapest, Hungary

[b] Institute of Cancer Research, Medical University of Vienna, Borschkegasse 8A, 1090 Vienna, Austria

[c] 3rd Department of Medicine Research Laboratory, Semmelweis University, Kútvölgyi út 4, H-1125 Budapest, Hungary.

[d] Department of Experimental Pharmacology, National Institute of Oncology, Ráth György utca 7-9, H-1122 Budapest, Hungary.

† These authors contributed equally.

Running title: Targeting P-glycoprotein in cancer

Keywords: Chelators · Cancer · Multidrug Resistance · P-glycoprotein · Collateral Sensitivity

Financial support: Momentum Grant of the Hungarian Academy of Sciences (GS), ERC (StG-260572) (GS), OTKA (K84173, K116295) (JT)

The authors declare no potential conflicts of interest.

Corresponding Author: Gergely Szakács, Institute of Enzymology, Research Centre for Natural Sciences, Hungarian Academy of Sciences, Magyar Tudósok körútja 2, H-1117 Budapest, Hungary; Phone: +36-1-382-6715; E-mail: szakacs.gergely@ttk.mta.hu

Abstract

Despite significant progress, resistance to chemotherapy is still the main reason why cancer remains a deadly disease. An attractive strategy is to target the collateral sensitivity of otherwise multidrug resistant (MDR) cancer. In this study our aim was to catalogue various compounds that were reported to elicit increased toxicity in P-glycoprotein (Pgp) overexpressing MDR cells. We show that the activity of most of the serendipitously identified compounds reported to target MDR cells is in fact cell-line specific, and is not influenced significantly by the function of Pgp. In contrast, novel 8-hydroxyquinoline derivatives that we identify in the NCI DTP drug repository possess a robust Pgp-dependent toxic activity across diverse cell lines. Pgp expression associated with the resistance of the doxorubicin resistant Brca1$^{-/-}$;p53$^{-/-}$ spontaneous mouse mammary carcinoma cells could be eliminated by a single treatment with NSC57969, suggesting that MDR-selective compounds can effectively revert the MDR phenotype of cells expressing Pgp at clinically relevant levels. The discovery of new MDR-selective compounds shows the potential of this emerging technology and highlights the 8-hydroxyquinoline scaffold as a promising starting point for the development of compounds targeting the Achilles heel of drug resistant cancer.

Video microscopy. Cells were seeded in a 96-well plate at 5000 cells/well density. After 24h 1.5 µM NSC57969 was added to every well, and annexin positivity was monitored using the Annexin V, FITC Apoptosis Detection kit (Dojindo Molecular Technologies). Briefly, cells were washed with PBS and stained for 15 min at RT in dark with 5 µl Annexin V and 5 ul PI solution in a 10-fold diluted Annexin V Binding Solution. Images were captured with a JuLI Stage Real-Time Cell History Recorder (NanoEnTek) inside an incubator using bright, GFP (ex.466/40, em.525/50) and RFP (ex.525/50, em.580LP) channels.

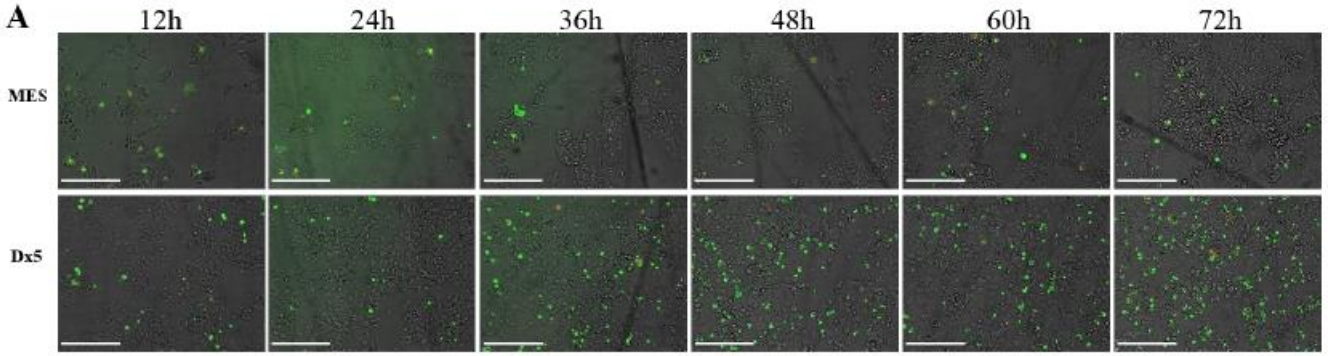

Figure 3. NSC57969 selectively induces apoptosis in Pgp-expressing cells. MES-SA (MES) and MES-SA/Dx5 (Dx5) cells were cultured in a 96-well plate at 5000 cells/well density in the presence of NSC57969 (1.5 µM). Scale bar: 250 µm. (A). The proportion of cells undergoing apoptosis at 72 hours of treatment was determined by FACS analysis (B).

OncoTargets and Therapy

Dovepress
open access to scientific and medical research

Open Access Full Text Article

ORIGINAL RESEARCH

Monitoring the effects of doxorubicin on 3D-spheroid tumor cells in real-time

This article was published in the following Dove Press journal:
OncoTargets and Therapy
22 November 2016
Number of times this article has been viewed

NamHuk Baek[1,*]
Ok Won Seo[1,*]
MinSung Kim[1]
John Hulme[2]
Seong Soo A An[2]

[1]Department of R & D, NanoEntek Inc., Seoul, Republic of Korea; [2]Department of BioNano Technology Gachon University, Gyeonggi-do, Republic of Korea

*These authors contributed equally to this work

Video abstract

Point your SmartPhone at the code above. If you have a QR code reader the video abstract will appear. Or use:
http://youtu.be/qWbeiIkkFs4

Abstract: Recently, increasing numbers of cell culture experiments with 3D spheroids presented better correlating results in vivo than traditional 2D cell culture systems. 3D spheroids could offer a simple and highly reproducible model that would exhibit many characteristics of natural tissue, such as the production of extracellular matrix. In this paper numerous cell lines were screened and selected depending on their ability to form and maintain a spherical shape. The effects of increasing concentrations of doxorubicin (DXR) on the integrity and viability of the selected spheroids were then measured at regular intervals and in real-time. In total 12 cell lines, adenocarcinomic alveolar basal epithelial (A549), muscle (C2C12), prostate (DU145), testis (F9), pituitary epithelial-like (GH3), cervical cancer (HeLa), HeLa contaminant (HEp2), embryo (NIH3T3), embryo (PA317), neuroblastoma (SH-SY5Y), osteosarcoma U2OS, and embryonic kidney cells (293T), were screened. Out of the 12, 8 cell lines, NIH3T3, C2C12, 293T, SH-SY5Y, A549, HeLa, PA317, and U2OS formed regular spheroids and the effects of DXR on these structures were measured at regular intervals. Finally, 5 cell lines, A549, HeLa, SH-SY5Y, U2OS, and 293T, were selected for real-time monitoring and the effects of DXR treatment on their behavior were continuously recorded for 5 days. A potential correlation regarding the effects of DXR on spheroid viability and ATP production was measured on days 1, 3, and 5. Cytotoxicity of DXR seemed to occur after endocytosis, since the cellular activities and ATP productions were still viable after 1 day of the treatment in all spheroids, except SH-SY5Y. Both cellular activity and ATP production were halted 3 and 5 days from the start of the treatment in all spheroids. All cell lines maintained their spheroid shape, except SHSY-5, which behaved in an unpredictable manner when exposed to toxic concentrations of DXR. Cytotoxic effects of DXR towards SH-SY5Y seemed to cause degradation of the extracellular matrix, since all cells were dismantled from the spheroid upon cell death. On the other hand, 293T spheroids revealed retarded cellular activity and ATP productions upon DXR treatment throughout the experiment. Since 293T was the embryonic kidney cells, the fast clearance or neutralizations could have made them resistant towards DXR. In conclusion, the same degree of sensitivity from the 2D system did not translate to a 3D culture system, resulting in higher IC50 values than the 2D system. The varying sensitivities and tolerances to drugs could be better understood with a 3D cell culture system.

Keywords: doxorubicin, 3D spheroid, cytotoxicity

Correspondence: John Hulme; Seong Soo A An
Department of BioNano Technology, Gachon Medical Research Institute, Gachon University, (461-701) 1342 Sungnam Daero, Sungnamsi, Republic of Korea
Tel +82 31 750 8550
Fax +82 31 750 8755
Email flp15@gachon.ac.kr; seongaan@gachon.ac.kr

Introduction

Traditionally, monolayer cell cultures were used to monitor behavior and identify effective anti-tumor activities.[1] Initial work using extracted nerve cells from the notochord of frogs highlighted the challenges of growing 3D cellular structures in vivo.[2,3] In 1951, the HeLa cell line was established by Master and Lucey et al, which jump-started the full-scale research with animal cells.[4,5] Since then, various

Materials and methods

Materials

Cell lines from the American Type Culture Collection, Manassas, VA, USA in the current study were osteosarcoma (U2OS), cervical cancer (HeLa), HeLa contaminant (HEp2), neuroblastoma (SH-SY5Y), muscle (C2C12), pituitary epithelial-like (GH3), embryo (NIH3T3), prostate (DU145), testis (F9), adenocarcinomic alveolar basal epithelial (A549), embryonic kidney (293T), and embryo (PA317) cells. For cell culture, Dulbecco's Modified Eagle's Medium (DMEM) and Roswell Park Memorial Institute (RPMI) medias, Dulbecco's phosphate-buffered saline (DPBS), fetal bovine serum (FBS), trypsin (0.05%)-ethylenediaminetetraacetic acid (EDTA) (0.002%), and penicillin-streptomycin were from WELGENE, Inc. (Seoul, Republic of Korea). Spheroid microplates (96 well, C. 4520) in 3D-spheroid formation assay was purchased from Corning Inc. (Corning, NY, USA). Dimethyl sulfoxide (DMSO) and DXR for the 3D cancer spheroid screening and cell anti-proliferation assay were obtained from Sigma-Aldrich Co. (St Louis, MO, USA) and LC Laboratories (Woburn, MA, USA), respectively. CellTiter-Glo® reagent for measuring 3D ATP level in the 3D cell viability assay was purchased from Promega Corporation (Fitchburg, WI, USA). Automated Fluorescence Cell Counter Arthur (NanoEnTek, Seoul, Korea) was used to count the cells. 3D-spheroid cell cultures were monitored and confirmed by JuLI Stage: Real-Time Cell History Recorder (NanoEnTek). 3D cell viabilities were measured by Infinite Elisa Reader (Tecan, Männedorf, Switzerland).

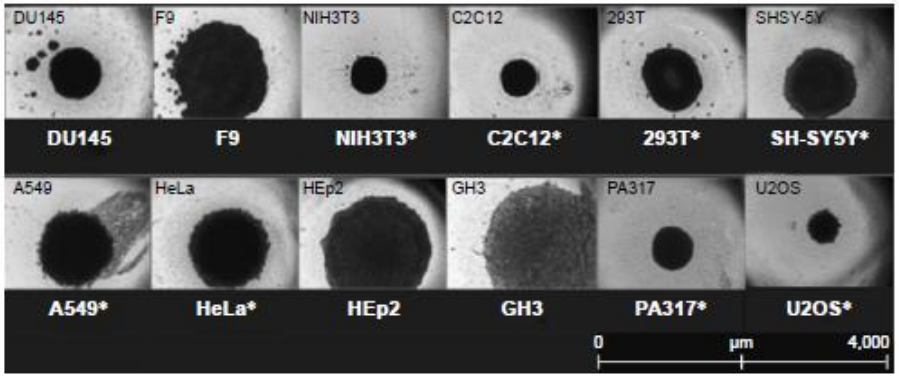

Figure 1 Formation of 3D-spheroids after 3 days of culturing 12 cell lines: prostate (DU145), testis (F9), embryo (NIH3T3), muscle (C2C12), embryonic kidney (293T), neuroblastoma (SH-SY5Y), adenocarcinomic alveolar basal epithelial (A549), cervical cancer (HeLa), HeLa contaminant (HEp2), pituitary epithelial-like (GH3), embryo (PA317) and osteosarcoma (U2OS) cells. *Indicates eight cell lines selected for further DXR cytotoxicity study.
Abbreviation: DXR, doxorubicin.

World Journal of Gastroenterology

Submit a Manuscript: http://www.wjgnet.com/esps/
Help Desk: http://www.wjgnet.com/esps/helpdesk.aspx
DOI: 10.3748/wjg.v23.i6.964

World J Gastroenterol 2017 February 14; 23(6): 964-975
ISSN 1007-9327 (print) ISSN 2219-2840 (online)

ORIGINAL ARTICLE

Basic Study

Long-term culture-induced phenotypic difference and efficient cryopreservation of small intestinal organoids by treatment timing of Rho kinase inhibitor

Sung-Hoon Han, Sehwan Shim, Min-Jung Kim, Hye-Yun Shin, Won-Suk Jang, Sun-Joo Lee, Young-Woo Jin, Seung-Sook Lee, Seung Bum Lee, Sunhoo Park

Sung-Hoon Han, Sehwan Shim, Min-Jung Kim, Hye-Yun Shin, Won-Suk Jang, Sun-Joo Lee, Young-Woo Jin, Seung-Sook Lee, Seung Bum Lee, Sunhoo Park, Laboratory of Radiation Exposure and Therapeutics, National Radiation Emergency Medical Center, Korea Institute of Radiological and Medical Science, Seoul 01812, South Korea

Author contributions: Lee SB and Park S contributed equally to this work; Han SH performed the majority of experiments and analyzed the data; Shim S, Kim MJ, Shin HY and Jang WS participated in care/treatment of animals and performed the molecular biochemical investigations; Lee SJ, Jin YW and Lee SS designed and coordinated the research; Lee SB and Park S analyzed the data and wrote paper; all the authors contributed to this manuscript.

Supported by a grant of the Korea Institute of Radiological and Medical Sciences, funded by Ministry of Science, ICT and Future Planning, South Korea, No. 1711031810/50586-2016 and No. 1711031808/50581-2016.

Institutional review board statement: The study was revised and approved by the Korea Institute of Radiological and Medical Sciences Institutional Review Board.

Institutional animal care and use committee statement: All procedures involving animals were reviewed and approved by the Institutional Animal Care and Use Committee of the Korea Institute of Radiological and Medical Sciences in Korea (IACUC protocol number: kirams2016-0043).

Conflict-of-interest statement: The authors declare that they have no potential conflicts of interest.

Data sharing statement: No additional data are available.

Manuscript source: Unsolicited manuscript

Correspondence to: Sunhoo Park, MD, PhD, Laboratory of Radiation Exposure and Therapeutics, National Radiation Emergency Medical Center, Korea Institute of Radiological and Medical Science, 75 Nowon-ro, Nowon-gu, Seoul 01812, South Korea. sunhoo@kirams.re.kr
Telephone: +82-2-9701274
Fax: +82-2-9702430

Received: September 5, 2016
Peer-review started: September 6, 2016
First decision: October 20, 2016
Revised: November 3, 2016
Accepted: November 23, 2016
Article in press: November 23, 2016
Published online: February 14, 2017

Abstract

AIM

To investigate a suitable long-term culture system and optimal cryopreservation of intestinal organoid to improve organoid-based therapy by acquiring large numbers of cells.

METHODS

Crypts were isolated from jejunum of C57BL/6 mouse. Two hundred crypts were cultured in organoid medium with either epidermal growth factor/Noggin/R-spondin1 (ENR) or ENR/CHIR99021/VPA (ENR-CV). For subculture, organoids cultured on day 7 were passaged using enzyme-free cell dissociation buffer (STEMCELL Technologies). The passage was performed once per week until indicated passage. For cryopreservation, undissociated and dissociated organoids were resuspended in freezing medium with or without Rho kinase inhibitor subjected to different treatment times. The characteristics of intestinal organoids upon extended passage and freeze-thaw were analyzed using EdU staining, methyl thiazolyl tetrazolium assay, qPCR and time-lapse live cell imaging.

RESULTS

We established a three-dimensional culture system for murine small intestinal organoids using ENR and ENR-CV media. Both conditions yielded organoids with a crypt-villus architecture exhibiting Lgr5$^+$ cells and differentiated intestinal epithelial cells as shown by morphological and biochemical analysis. However, during extended passage (more than 3 mo), a comparative analysis revealed that continuous passaging under ENR-CV conditions, but not ENR conditions induced phenotypic changes as observed by morphological transition, reduced numbers of Lgr5$^+$ cells and inconsistent expression of markers for differentiated intestinal epithelial cell types. We also found that recovery of long-term cryopreserved organoids was significantly affected by the organoid state, *i.e.*, whether dissociation was applied, and the timing of treatment with the Rho-kinase inhibitor Y-27632. Furthermore, the retention of typical morphological characteristics of intestinal organoids such as the crypt-villus structure from freeze-thawed cells was observed by live cell imaging.

CONCLUSION

The maintenance of the characteristics of intestinal organoids upon extended passage is mediated by ENR condition, but not ENR-CV condition. Identified long-term cryopreservation may contribute to the establishment of standardized cryopreservation protocols for intestinal organoids for use in clinical applications.

Key words: Intestinal organoid; Rho kinase inhibitor; Three-dimensional culture; Cryopreservation; Long-term culture

Time-lapse live cell imaging

Live cell imaging was performed on a JuLi stage system (NanoEnTek, Seoul, South Korea). A culture dish placed on the microscope stage was covered with a chamber in 5% CO_2 at 37 ℃. Images for the growth of crypts were an acquired at 60-min intervals. The data were processed using JuLi stage software v1.0 (NanoEnTek).

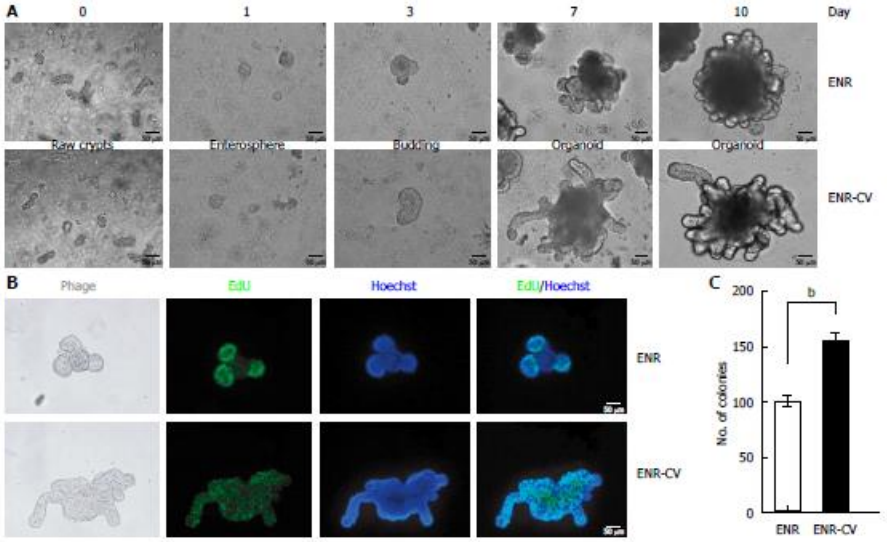

Figure 1 Establishment of small intestinal organoid culture under epidermal growth factor/noggin/r-spondin1 and epidermal growth factor/noggin/r-spondin1/CHIR99021/VPA conditions. Crypts were isolated from the small intestines of C57/B6 mice at ages 9-12 wk and were resuspended in growth factor-reduced Matrigel. A: Time course of the growth of isolated crypts at passage 0 (P0) under two different culture media. Enterospheres formed on day 1, budding appeared on day 3, and robust budding was observed on days 5-10. Scale bars: 50 μm. B: Organoids were incubated with the thymidine analog EdU (green) for 1 h, and freshly isolated crypts were cultured for 6 d. Images were analyzed by fluorescence microscopy, and nuclei were double stained with Hoechst (blue). Scale bars: 50 μm. C: Numbers of organoids grown in two different media for 7 d. Organoids exhibiting at least two budding structures in each group were counted. The data are shown as means ± SDs of triplicate experiments ($^bP < 0.01$, Student's *t*-tests).

Arch Dermatol Res (2017) 309:55–62
DOI 10.1007/s00403-016-1703-2

ORIGINAL PAPER

3D modeling of keloid scars in vitro by cell and tissue engineering

Dutsadee Suttho[1,2,3,4] · Samlee Mankhetkorn[1] · Delphine Binda[2,4] · Lionel Pazart[2,4] · Philippe Humbert[2,3,4] · Gwenaël Rolin[2,3,4]

Received: 3 May 2016 / Revised: 17 November 2016 / Accepted: 28 November 2016 / Published online: 9 December 2016

Abstract Keloids are pathologic scars defined as dermal fibrotic tumors resulting from a disturbance of skin wound healing process. Treatments against keloids are multiple, sometimes empirical and none of them really provides an effective tool for physicians. The lack of effective treatments is correlated with the poor understanding of keloid pathogenesis. To fill this gap, researchers need strong models mimicking keloids as closely as possible. The objective of this study was to establish in vitro a new reconstructed keloid model (RKM), by combining fibroblasts extracted from the three major area of a keloid (center, periphery, non-lesional) in a three-dimensional biomaterial. To this aim, fibroblasts of three keloid locations were extracted and characterized, and then integrated in a hydrated collagen gel matrix during a three-step procedure. The heterogeneity of fibroblasts was assessed according to their proliferative and remodeling capacities. RKMs were further visualized and characterized by both light and scanning electron microscopy. This reconstructed keloid model should be very useful for investigating keloid fibroblasts function in conditions mimicking in vivo situation. Moreover, RKM should also be a suitable model for either drug study and discovery or innovative approaches using medical devices both during cancer and cancer-like disease investigation.

Keywords Keloid scar · Fibroblasts · 3D model · Tissue engineering

✉ Gwenaël Rolin
grolin@chu-besancon.fr

[1] Laboratory of Physical Chemistry, Molecular and Cellular Biology, Department of Radiologic Technology, Faculty of Associated Medical Sciences, Center of Excellence for Molecular Imaging, Chiang Mai University, Chiang Mai, Thailand

[2] Clinical Investigation Center, Inserm CICB 1431, University Hospital of Besançon, 2 Place St Jacques, 25000 Besançon, France

[3] Inserm UMR 1098, Engineering and Cutaneous Biology Team, Besançon, France

[4] University of Bourgogne Franche-Comté, SFR FED 4234, Besançon, France

Introduction

Keloids are pathologic scars defined as dermal fibrotic tumors resulting from a disturbance of skin wound healing process [3]. Even if keloids are known to have no malignant potential, extended ones can induce a large loss of quality of life to patients. Indeed, the major clinical features of keloids are their progression beyond the initial site of skin injury, their persistence during time and the lack of natural regression [6]. When they are extended, keloids lead to physical (pruritus, inflammation, pain) and psychical alterations for patients [2], especially when the face is affected.

Treatments against keloids are multiple and sometimes empirical. In 2013, Ud-Din and Bayat [35] have published an exhaustive review about the management of keloid disease and show clearly the multitude of existing clinical approaches. These treatments involve intralesional steroid injection, application of silicone gel, radiotherapy, photodynamic therapy, electrical stimulation, surgical excision, cryosurgery and use of DNA synthesis inhibitor, immune modulator or bleomycin. However, none of these treatments (or combination) really provides an effective tool for the physicians.

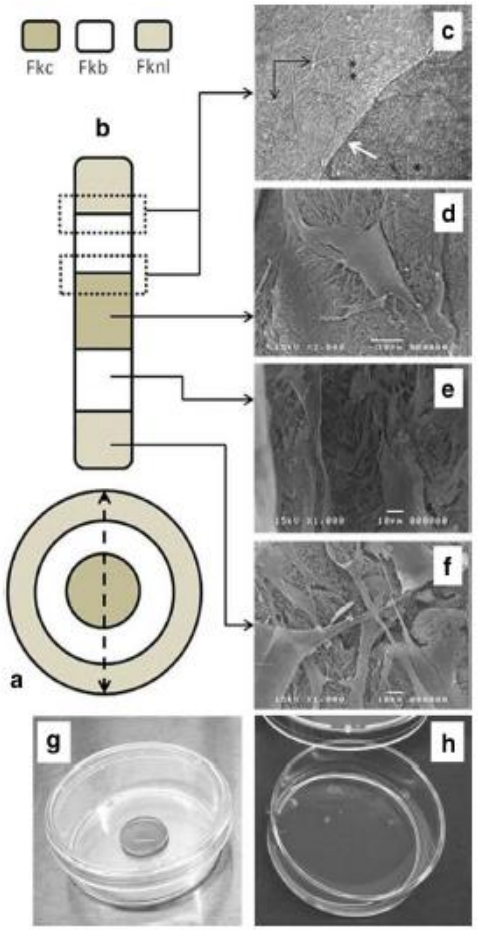

Fig. 4 Image processing of RKM. **a**, **b** Respectively, the *upper* and *front view* of RKM composed of three collagen gel subparts including FKc (*brown*), FKp (*white*) and FKnl (*gray*). **c** Limit (*white arrow*) between each area observed by light microscopy. *Black arrows* fibroblasts, (*asterisk*) FKc and (*double asterisks*) FKp. **d**, **e**, **f** Scanning electronic microscopy of fibroblasts attached to collagen fibers in three different reconstructed areas. **g** The first reconstructed part (*center*) of the entire model **h**

Conclusion and perspectives

Reconstructed keloid model (RKM) is based on the observation that cells and tissue organization is highly complex in keloid scar tissue. RKM was developed according to a desire to propose a most appropriate model of keloid in the family of 3D experimental collagen tissue-models, suitable to investigate normal and pathological fibroblasts [5]. Inspired from existing collagen gel models [10], our RKM is easy to perform and could be upgraded to a more complete evolutionary model. For this, three levers can be used to improve the RKM model: cells, scaffold and culture medium. From the cells point of view, the three main compartments of keloid scar (center, periphery and non-lesional skin) were reconstructed. Because cell migration is a phenomenon that is complex and crucial for tissue repair and tumor invasion [23], one of the major uses of RKM could concern dynamic studies to follow cell–cell and cell–matrix interactions as well as cell movement between compartments during migration in 3D. To this aim, migrating cells can be monitored in real time using video–time-lapse microscopy [12] directly from the cell culture incubator (i.e, with devices such as JuLI™ Stage) where pictures are taken at regular intervals. Subsequently, recorded data can be statistically analyzed to determine cells trajectory and interactions [38]. Moreover, since cells can be tracked both in light and fluorescent microscopy, this could allow seeding and follow-up of GFP-transfected cells to qualitatively and quantitatively track proteins (involved for example in adhesion and migration, apoptosis, autophagy…) during 3D dynamic culture. Then, RKM model could also be interestingly used in silencing assay

www.impactjournals.com/oncotarget/ Oncotarget, 2017, Vol. 8, (No. 5), pp: 7265-7275

Priority Research Papers: Gerotarget

Overactive mTOR signaling leads to endometrial hyperplasia in aged women and mice

Preety Bajwa[1], Sarah Nielsen[2], Janine M. Lombard[3,4], Loui Rassam[2,3], Pravin Nahar[3,5], Bo R. Rueda[6], J. Erby Wilkinson[7], Richard A. Miller[8] and Pradeep S. Tanwar[1]

[1] Gynaecology Oncology Group, School of Biomedical Sciences and Pharmacy, Callaghan, New South Wales, Australia

[2] Hunter Cancer Biobank, Callaghan, New South Wales, Australia

[3] School of Medicine and Public Health, University of Newcastle, Callaghan, New South Wales, Australia

[4] Department of Medical Oncology, Gynaecology Oncology, Calvary Mater Newcastle, Waratah, New South Wales, Australia

[5] Gynaecology and Obstetrics, John Hunter Hospital, New Lambton, New South Wales, Australia

[6] Vincent Department of Obstetrics and Gynecology and Department of Obstetrics & Gynecology, Vincent Center for Reproductive Biology, Massachusetts General Hospital and Gynecologic Oncology Division, Massachusetts General Hospital, Harvard Medical School, Boston, MA, USA

[7] Department of Pathology, Unit for Laboratory Animal Medicine, University of Michigan School of Medicine, Ann Arbor, MI, USA

[8] Department of Pathology and Geriatrics Center, University of Michigan, Ann Arbor, MI, USA

Correspondence to: Pradeep S. Tanwar, email: pradeep.tanwar@newcastle.edu.au

Keywords: endometrial, mTOR, rapalogs, aging, PI3K, Pten, Gerotarget

Received: October 11, 2016 *Accepted:* December 05, 2016 *Published:* December 12, 2016

ABSTRACT

During aging, uncontrolled epithelial cell proliferation in the uterus results in endometrial hyperplasia and/or cancer development. The mTOR signaling pathway is one of the major regulators of aging as suppression of this pathway prolongs lifespan in model organisms. Genetic alterations in this pathway via mutations and/or amplifications are often encountered in endometrial cancers. However, the exact contribution of mTOR signaling and uterine aging to endometrial pathologies is currently unclear. This study examined the role of mTOR signaling in uterine aging and its implications in the development of endometrial hyperplasia. The hyperplastic endometrium of both postmenopausal women and aged mice exhibited elevated mTOR activity as seen with increased expression of the pS6 protein. Analysis of uteri from *Pten* heterozygous and *Pten* overexpressing mice further confirmed that over-activation of mTOR signaling leads to endometrial hyperplasia. Pharmacological inhibition of mTOR signaling using rapamycin treatment suppressed endometrial hyperplasia in aged mice. Furthermore, treatment with mTOR inhibitors reduced colony size and proliferation of a PTEN negative endometrial cancer cell line in 3D culture. Collectively, this study suggests that hyperactivation of the mTOR pathway is involved in the development of endometrial hyperplasia in aged women and mice.

INTRODUCTION

The mammalian uterus is one of the most regenerative organs that undergoes the cyclical process of degeneration and regeneration during each oestrous cycle [1]. The uterus plays a critical role in pregnancy and child birth. The mammalian uterus is divided into three compartments, namely endometrium (luminal and glandular epithelial cells), stroma, and myometrium (smooth muscle cells) [1]. After fertilization of an egg in the fallopian tube, the resulting embryo moves to the uterine cavity where its interaction with the receptive endometrium initiate a cascade of events leading to implantation, decidualization, and the establishment of pregnancy. Any aberrations during this process lead to premature termination of pregnancy and abortion [2].

3D cell viability and ATP assays

Cell viability in 3D cell culture was assessed using CellTiter-Glo® Luminiscent cell viability assay (Promega, NSW, Australia) as per the manufacturer's instructions. Briefly, 5000 cells/well were seeded onto either 96-well ultra-low attachment plates or tissue culture plates coated with matrigel. Cells were allowed to grow for 24h for spheroid formation followed by desired drug treatments. Cell growth was monitored and images were photographed using JuLI™ Stage Real time cell history recorder (NanoEnTek Inc., USA). At 72h post- treatment, cells were incubated with CellTiter-Glo® 3D Reagent for 30 minutes at room temperature and luminescence signal was recorded using the FLUOstar OPTIMA (BMG Labtech, VIC, Australia).

Report

Cell Reports

Huntingtin Inclusions Trigger Cellular Quiescence, Deactivate Apoptosis, and Lead to Delayed Necrosis

Graphical Abstract

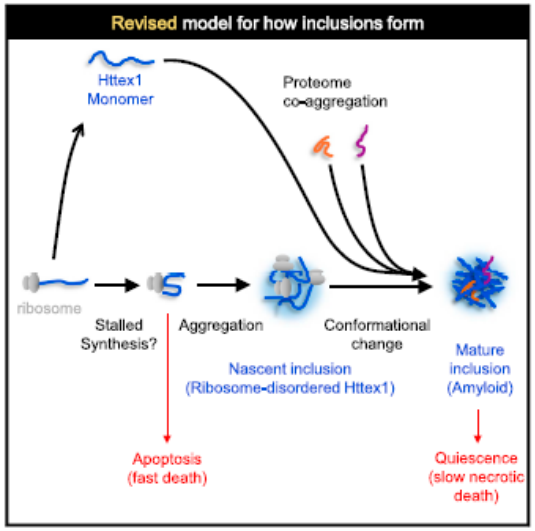

Highlights

- Soluble mutant Huntingtin exon 1 (Httex1) triggers apoptosis
- Httex1 inclusions deactivate apoptosis but activate delayed necrosis
- Nascent inclusions form from disordered Httex1 and ribosomes
- Upon maturation, Httex1 converts into amyloid and co-recruits prion domain proteins

Authors

Yasmin M. Ramdzan, Mikhail M. Trubetskov, Angelique R. Ormsby, ..., David B. Ascher, Gavin E. Reid, Danny M. Hatters

Correspondence

dhatters@unimelb.edu.au

In Brief

Httex1 aggregation into inclusions has paradoxically been reported as either toxic or beneficial in Huntington's disease. Ramdzan et al. define a dual mechanism of toxicity that explains this paradox. Soluble Httex1 triggers a fast death by apoptosis, whereas Httex1 inclusions invoke quiescence and redirect death to a slower necrotic pathway.

Accession Numbers

PXD005120

ReAsH Staining, Stripping, and Restaining

For ReAsH staining, after 24 hr transfection (or transduction in the case of neurons), cells were washed twice with HBSS and stained with 1 μM ReAsH and 10 μM 1,2-ethanedithiol in Hank's balanced salt solution (HBSS) for 30 min at 37°C. The cells were then washed with 250 μM BAL for 15 min at 37°C, followed by a wash with HBSS.

For the stripping and restaining experiments, AD293 cells expressing pT-REx-Httex1^{TC9}(97Q)-Cerulean were labeled with ReAsH 24 hr after transfection as described above. The cells were imaged with a JuLI-stage microscope (NanoEnTek). ReAsH was stripped by 15-min treatment with 50 mM BAL in HBSS at 37°C followed by three washes with HBSS and then imaged again. Cells were then restained with ReAsH as described above at the time points indicated in the figures. Data were analyzed as described under Survival Analyses.

Survival Analyses

AD293 cells were co-transfected with pT-REx-HttEx1^{TC9}(97Q)-Cerulean (or pT-REx-HttEx1^{TC9}(97Q)-FT-Fast) and pT-REx-mCherry (or pT-Rex-Cerulean). 24 hr after transfection, the medium was refreshed. To block caspases, QVD-OPh (50 μM) was added at 24 hr. Cells were imaged longitudinally with a JuLI-stage fluorescence microscope (NanoEnTek). For analysis of cells assessing mechanism of death, apoptosis was measured using CellEvent caspase-3/7 green detection reagent (Life Technologies, catalog number C10423) according to the manufacturer's instructions.

AD293 cells were treated with MitoProbe DiOC$_2$(3) (50 nM) or CellROX (5 μM) for 30 min in a cell culture incubator at 37°C, washed with PBS, and analyzed by flow cytometry as described previously (Ramdzan et al., 2012).

HeLa tet Repressor Experiments

HeLa tet repressor cells were co-transfected with pGW-Httex1-mCherry and pT-REx-Emerald. 24 hr after transfection, the medium was refreshed and supplemented with 1 μg/mL tetracycline. The cells were imaged for 48 hr with a JuLI-stage live-cell imaging fluorescence microscope (NanoEnTek).

Ramdzan et al., 2017, Cell Reports 19, 919–927
May 2, 2017 © 2017 The Authors.
http://dx.doi.org/10.1016/j.celrep.2017.04.029

CellPress

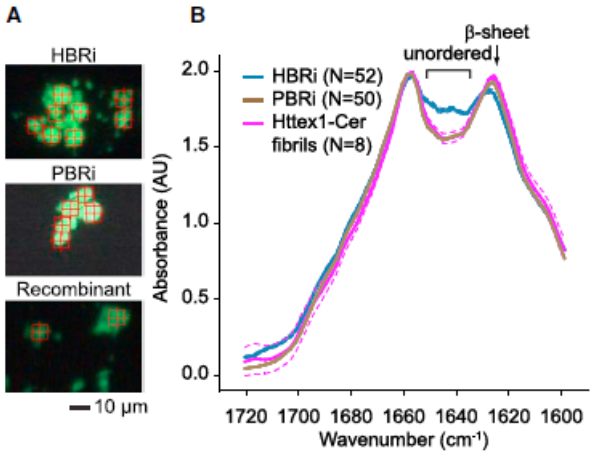

Figure 2. Httex1 Is Disordered in Early-Formed Inclusions and Converts to Amyloid over Time

(A) Fluorescence micrograph of inclusions and amyloid fibrils formed by purified Httex1-Cerulean for FTIR analysis (red cross-hairs mark representative beam clipping windows).

(B) Mean FTIR spectra with replicates referring to individual inclusions. Solid lines show means, and dashed lines show SEM.

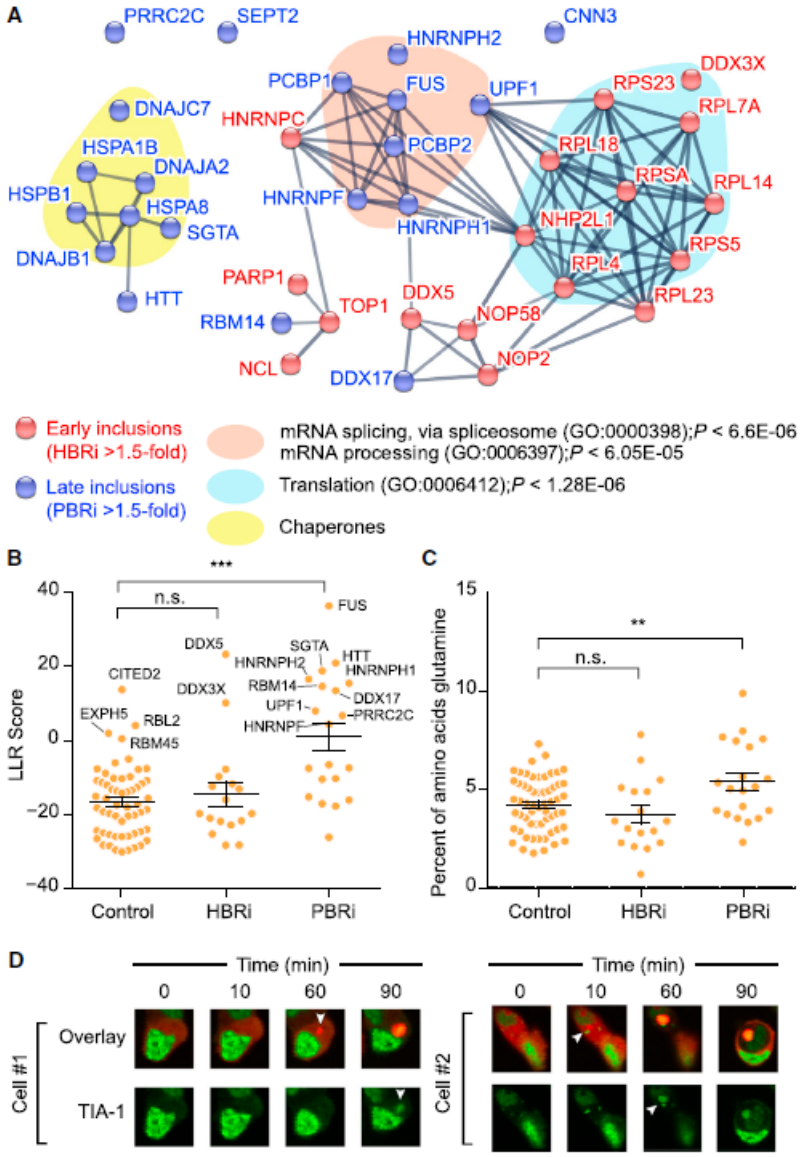

Figure 4. Early Inclusions Recruit Translational Machinery, whereas Mature Inclusions Attract Proteins with Predicted Prion-like Domains

(A) Protein-protein interaction network (STRING v10) of proteins identified in inclusions (the full list of proteins can be found in Table S2).

(B) Analysis of prion domains using the PLAAC algorithm. Higher log-likelihood ratios (LLR) relate to sequences in proteins more likely being a prion domain.

(C) Glutamine content versus control dataset of random human proteins (listed in Table S2).

(D) Recruitment of GFP-tagged prion domain protein TIA-1 (green) into Httex1(97Q)-Cherry inclusions (red) after the inclusion has formed. Two representative cells are shown in a time-lapse series.

Oncogene (2017) 36, 6490–6500

www.nature.com/onc

ORIGINAL ARTICLE

Oncosis and apoptosis induction by activation of an overexpressed ion channel in breast cancer cells

AA Peters[1,8], SYN Jamaludin[1,8,9], KTDS Yapa[1], S Chalmers[1], AP Wiegmans[2], HF Lim[1], MJG Milevskiy[3], I Azimi[1,4], FM Davis[1,4], KS Northwood[3], E Pera[1], DL Marcial[1], E Dray[5], NJ Waterhouse[6], PJ Cabot[1], TJ Gonda[1], PA Kenny[7], MA Brown[3], KK Khanna[6], SJ Roberts-Thomson[1] and GR Monteith[1,4]

The critical role of calcium signalling in processes related to cancer cell proliferation and invasion has seen a focus on pharmacological inhibition of overexpressed ion channels in specific cancer subtypes as a potential therapeutic approach. However, despite the critical role of calcium in cell death pathways, pharmacological activation of overexpressed ion channels has not been extensively evaluated in breast cancer. Here we define the overexpression of transient receptor potential vanilloid 4 (TRPV4) in a subgroup of breast cancers of the basal molecular subtype. We also report that pharmacological activation of TRPV4 with GSK1016790A reduced viability of two basal breast cancer cell lines with pronounced endogenous overexpression of TRPV4, MDA-MB-468 and HCC1569. Pharmacological activation of TRPV4 produced pronounced cell death through two mechanisms: apoptosis and oncosis in MDA-MB-468 cells. Apoptosis was associated with PARP-1 cleavage and oncosis was associated with a rapid decline in intracellular ATP levels, which was a consequence of, rather than the cause of, the intracellular ion increase. TRPV4 activation also resulted in reduced tumour growth *in vivo*. These studies define a novel therapeutic strategy for breast cancers that overexpress specific calcium permeable plasmalemmal ion channels with available selective pharmacological activators.

Oncogene (2017) **36,** 6490–6500; doi:10.1038/onc.2017.234; published online 31 July 2017

INTRODUCTION

The oncogenic process is associated with many molecular changes, including remodelling of specific calcium (Ca^{2+})-permeable ion channels. Ion channel expression changes are seen in different cancers including those of the breast, brain, prostate, ovary and colon.[1–6] These include elevated levels of calcium channel, voltage-dependent, L-type, alpha 1D subunit ($Ca_v1.3$) in aggressive castrate-resistant prostate cancer compared with primary prostate cancer,[7] and pronounced increases in transient receptor potential (TRP) cation channel C6 (TRPC6) in high-grade human gliomas.[2] Ca^{2+} channel expression can also differ between cancers of the same tissue origin but of different subtypes, for example, in breast cancer, elevated TRPV6 is more common in oestrogen receptor-negative breast cancer.[8]

Calcium signalling regulates a variety of diverse cellular functions by precisely controlling the nature of the calcium signal. For example, the amplitude and duration of increases in cytosolic-free Ca^{2+} ($[Ca^{2+}]_{cyt}$) and the cellular location of changes in Ca^{2+} levels can all differentially regulate cellular processes.[9,10] Selective regulation of the calcium permeable ion channels of the plasma membrane, which are encoded for by over 50 human genes, facilitates this precise control.[10] However, pathophysiological-induced alterations in the expression of specific Ca^{2+} permeable ion channels, and subsequent alterations in Ca^{2+} signalling can contribute to tumourigenesis through the promotion of specific hallmarks of cancer. Examples of these contributions include enhanced proliferation of prostate cancer cells via the remodelling of Orai3 Ca^{2+} channel expression,[11] the reduction of MCF-7 breast tumour growth with Orai1 channel silencing,[12] and the association between TRPM7 channel expression and metastatic potential of breast cancer cells.[13] Identifying Ca^{2+} channels that are over-expressed in breast cancers of the basal subtype would represent a therapeutic opportunity to exploit a pathophysiological change. Basal breast cancers are associated with poor prognosis and overlap with breast cancers negative for the oestrogen, progesterone and human epidermal growth factor receptor 2 (HER2) receptors,[14] limiting the use of effective hormonal and molecularly targeted therapies.

The intrinsic ability of the Ca^{2+} ion to promote pathways key in cancer cell proliferation and invasion has led to a focus on inhibiting channel activity as the therapeutic paradigm. Such an approach is exemplified by both silencing and pharmacological inhibition of Orai1 attenuating the migration and invasion of breast cancer cells *in vitro* and *in vivo*.[15] An alternative therapeutic strategy is Ca^{2+} channel activation and associated effects on processes sensitive to major and sustained elevations of intracellular free Ca^{2+}, which include promotion of cell death or suppression of cell cycle progression. Disruption of ion gradients occurs in a variety of cell death pathways including apoptosis[16]

[1]School of Pharmacy, The University of Queensland, Brisbane, Queensland, Australia; [2]Tumour Microenvironment Laboratory, QIMR Berghofer Medical Research Institute, Brisbane, Queensland, Australia; [3]School of Chemistry and Molecular Biosciences, The University of Queensland, Brisbane, Queensland, Australia; [4]Mater Research Institute, The University of Queensland, Translational Research Institute, Brisbane, Queensland, Australia; [5]Institute of Health and Biomedical Innovation and School of Biomedical Sciences, Queensland University of Technology, Translational Research Institute, Brisbane, Queensland, Australia; [6]Signal Transduction Laboratory, QIMR Berghofer Medical Research Institute, Brisbane, Queensland, Australia and [7]Kabara Cancer Research Institute, Gundersen Medical Foundation, La Crosse, WI, USA. Correspondence: Professor GR Monteith, School of Pharmacy, The University of Queensland, 20 Cornwall Street, Woolloongabba, 4102, Brisbane, QLD, Australia.
E-mail: gregm@uq.edu.au
[8]These authors contributed equally to this work.
[9]Current address: Faculty of Medicine, Universiti Sultan Zainal Abidin, Kuala Terengganu, Terengganu, Malaysia.
Received 21 September 2016; revised 1 June 2017; accepted 2 June 2017; published online 31 July 2017

Morphological assessment of cell death

MDA-MB-468 cells were plated in 96-well plates at 3×10^3 cells per well or 7×10^3 cells per well for siRNA studies, after 24 h cells were treated with media containing 8% serum or siRNA and after 72 h cells were treated with vehicle (0.1% DMSO) or GSK1016790A (1–100 nM). Live cell imaging was performed using a JuLI Stage automated imaging system (NanoEntek, Seoul, Korea) with a 10x objective or for siRNA studies an Olympus IX81 Inverted fluorescent microscope (Notting Hill, VIC, Australia, with a Solent Scientific incubator (Segensworth, UK) and a Hamamatsu Orca Flash 2.8 Megapixel CMOS camera, Hamamatsu City, Japan) with a 10x objective. Images were acquired approximately every 60 s for 48 h. Cell morphology was characterised in cells in five pre-defined regions (104×140 µm) or for siRNA studies one identical region for each treatment type (169×169 µm). Cell morphology was defined as survived (cell mitosis or no morphological change at the end of the experiment), apoptosis (cell condensed and underwent blebbing and dispersed into at least five multiple distinct bodies; time of death was the time at which at least five distinct cellular packages were observed), failed mitosis (cell with multiple nuclei underwent blebbing after failed attempts of daughter cell separation), oncosis (a major and sudden change in cell contrast usually immediately preceded by swelling of the cell; time of death was the time at which the sudden change in contrast was observed), other (morphological changes associated with cell death that did not fit the aforementioned criteria; often mixed morphological changes, for example, swelling and blebbing). Cells that migrated out of the field or became obstructed from view were excluded.

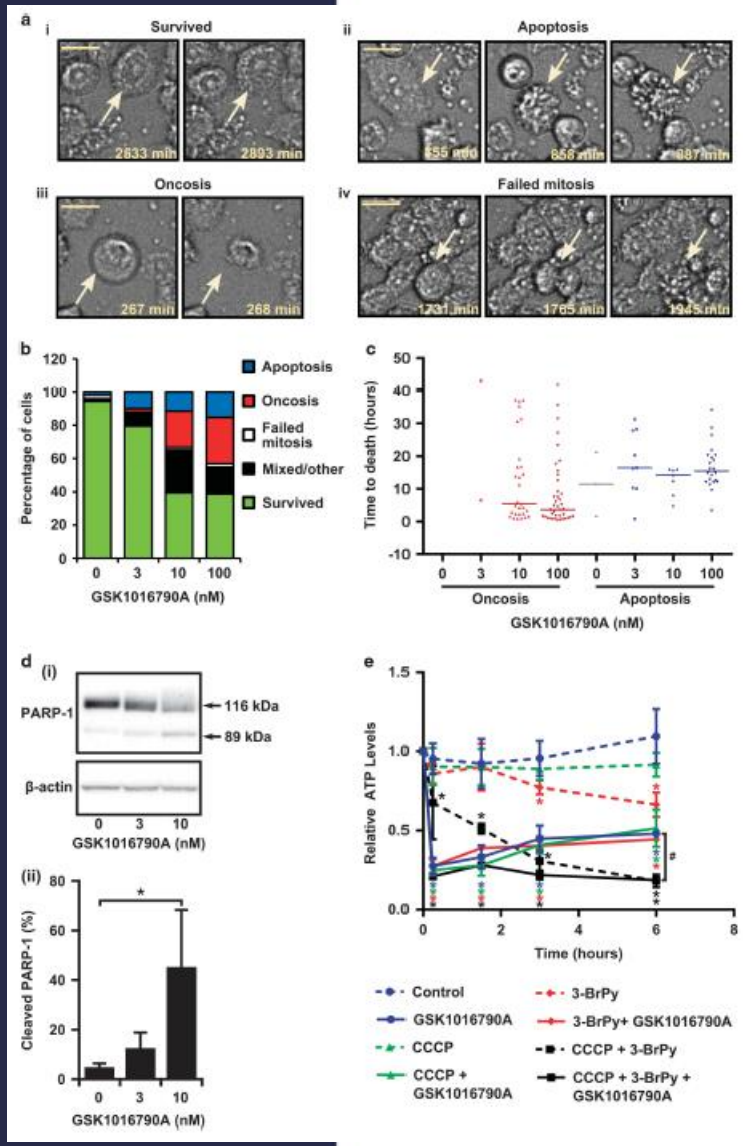

Figure 5. The TRPV4 activator GSK1016790A induces multiple cell death mechanisms in MDA-MB-468 breast cancer cells. (**a–c**) MDA-MB-468 cells were treated with GSK1016790A (0–100 nM) and bright field images were captured approximately every 60 s for 48 h. Data are from three independent experiments. (**a**) Representative images of cells treated with 100 nM GSK1016790A that were defined as morphologies representing cells that (i) survived, or (ii) underwent apoptosis, (iii) oncosis or (iv) failed mitosis. Scale bar represents 20 μM. (**b**) Quantification of cell fate was assessed in three independent experiments in a total of 577 individual cells. The percentage of cells undergoing each morphological change over the 48-h assessment period is shown for increasing concentrations of GSK1016790A. (**c**) Scatter plot of the time to cell death for oncosis and apoptosis of individual cells treated with each concentration of GSK1016790A assessed, horizontal line represents the median time for the observed event. (**d**) Assessment of PARP-1 cleavage induced by 24 h incubation with GSK1016790A, 96 h after plating (i) significant PARP-1 cleavage was observed with 10 nM GSK1016790A after 24 h (ii) mean % cleaved PARP-1 cleavage ± s.d. from three independent experiments ($n = 3$; $^*P < 0.05$, one-way analysis of variance (ANOVA) with Dunnett's multiple comparison test). (**e**) The effect of GSK1016790A (100 nM) on ATP levels in MDA-MB-468 breast cancer cells in the presence and absence of an oxidative phosphorylation inhibitor (carbonyl cyanide 3-chlorophenylhydrazone (CCCP), 4 μM) or a glycolysis inhibitor (3-bromopyruvic acid (3-BrPy), 100 μM) or both inhibitors. Data are shown as mean ± s.d. from three independent ($n = 3$, $^*P < 0.05$, compared with baseline (0 h) for each treatment group (one-way ANOVA with Dunnett's multiple comparison test), $^*P < 0.05$, compared with different treatments in the presence of GSK1016790A at 6 h (two-way ANOVA with Tukey's multiple comparison test).

Short Communication

Skin Pharmacology and Physiology

Skin Pharmacol Physiol 2017;30:190–196
DOI: 10.1159/000477356

Received: January 19, 2017
Accepted after revision: May 8, 2017
Published online: June 30, 2017

Antimelanogenic Efficacy of Melasolv (3,4,5-Trimethoxycinnamate Thymol Ester) in Melanocytes and Three-Dimensional Human Skin Equivalent

John Hwan Lee[a, e] Eun-Soo Lee[a] Il-Hong Bae[a, d] Jeong-Ah Hwang[a]
Se-Hwa Kim[b, c] Dae-Yong Kim[d] Nok-Hyun Park[a] Ho Sik Rho[a] Yong Jin Kim[a]
Seong-Geun Oh[e] Chang Seok Lee[a]

[a]Amorepacific Corporation R&D Center, Yongin, [b]Department of Medical Physics, University of Science and Technology, and [c]Center for Nano-Bio Measurement, Korea Research Institute of Standards and Science, Daejeon, [d]College of Veterinary Medicine, Seoul National University, and [e]Department of Chemical Engineering, Hanyang University, Seoul, Republic of Korea

Keywords
Melasolv · Melanogenesis · Depigmentary agent · Three-dimensional human skin equivalent

Abstract

Background/Aims: Excessive melanogenesis often causes unaesthetic hyperpigmentation. In a previous report, our group introduced a newly synthesized depigmentary agent, Melasolv™ (3,4,5-trimethoxycinnamate thymol ester). In this study, we demonstrated the significant whitening efficacy of Melasolv using various melanocytes and human skin equivalents as in vitro experimental systems. ***Methods:*** The depigmentary effect of Melasolv was tested in melan-a cells (immortalized normal murine melanocytes), α-melanocyte-stimulating hormone (α-MSH)-stimulated B16 murine melanoma cells, primary normal human melanocytes (NHMs), and human skin equivalent (MelanoDerm). The whitening efficacy of Melasolv was further demonstrated by photography, time-lapse microscopy, Fontana-Masson (F&M) staining, and 2-photon microscopy. ***Results:*** Melasolv significantly inhibited melanogenesis in the melan-a and α-MSH stimulated B16 cells. In human systems, Melasolv also clearly showed a whitening effect in NHMs and human skin equivalent, reflecting a decrease in melanin content. F&M staining and 2-photon microscopy revealed that Melasolv suppressed melanin transfer into multiple epidermal layers from melanocytes as well as melanin synthesis in human skin equivalent. ***Conclusion:*** Our study showed that Melasolv clearly exerts a whitening effect on various melanocytes and human skin equivalent. These results suggest the possibility that Melasolv can be used as a depigmentary agent to treat pigmentary disorders as well as an active ingredient in cosmetics to increase whitening efficacy.

John Hwan Lee and Eun-Soo Lee contributed equally to this work. Seong-Geun Oh and Chang Seok Lee are co-corresponding authors.

Chang Seok Lee, PhD
Amorepacific Corporation R&D Center
1920 Yonggu-daero, Giheung-gu
Yongin, Gyeonggi-do, 17074 (Republic of Korea)
E-Mail cslee2010@amorepacific.com

Seong-Geun Oh, PhD
Department of Chemical Engineering, Hanyang University
Wangsimni-ro, Seongdong-gu, Seoul, 04763 (Republic of Korea)
E-Mail seongoh@hanyang.ac.kr

KARGER

E-Mail karger@karger.com
www.karger.com/spp

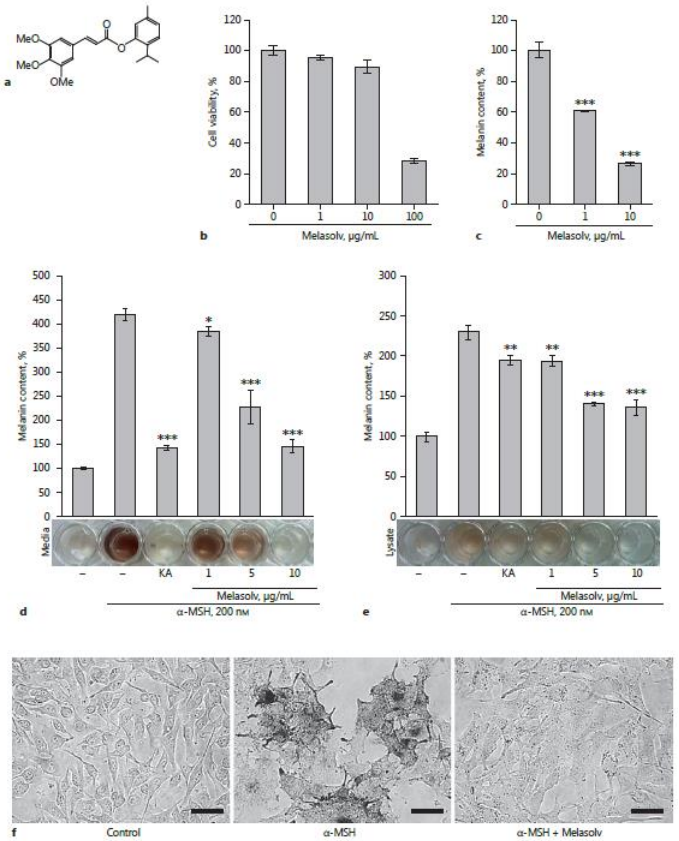

Fig. 1. The depigmentary efficacy of Melasolv in melan-a and B16 murine cell line. **a** Chemical structure of Melasolv. **b** Effects of Melasolv on the viability of melan-a cells. Cells were treated with the indicated concentrations of Melasolv for 72 h. Values are means ± SD of 3 determinations, expressed as a percentage of the control. **c** Effects of Melasolv on melanin synthesis in melan-a cells. Values are means ± SD of 3 determinations expressed as a percentage of the control. Effects of Melasolv on secreted (extracellular) melanin (**d**) and intracellular melanin (**e**) contents in α-MSH-stimulated B16 cells. B16 cells were treated with the indicated concentrations of Melasolv and α-MSH for 3 days. Then, the lysates were estimated by absorbance at 405 nm. The melanin contents were normalized for total protein contents. Kojic acid (KA; 50 μg/mL) is used as a reference compound, which is a representative antimelanogenic agent [4]. **f** Bright-field images of B16 melanoma cell line treated with α-MSH(200 nM) ± Melasolv (10 μg/mL) for 72 h. Dark dot-like patterns indicate intracellular melanosome. Scale bar, 50 μm. * $p < 0.05$; ** $p < 0.01$; *** $p < 0.001$.

Time-Lapse Melanin Imaging

For melanin assays, B16 cells were cultured in a 12-well plate for 24 h at 37°C in a 10% CO_2 incubator. Then, after treatment of each group with α-MSH and Melasolv, bright-field images of live cell cultures in a 10% CO_2 incubator were recorded every hour for 70 h using a JuLI Stage real-time cell history recorder (NanoEnTek, South Korea) connected to a JuLI Stage microscope equipped with a ×20 objective lens. Three different regions per group were randomly selected and analyzed. Dark dot signals in B16 cells in the bright-field images indicate intracellular melanin. The LED light conditions used in this study caused no phototoxicity (data not shown).

Cancer Letters 403 (2017) 48–58

Contents lists available at ScienceDirect

Cancer Letters

journal homepage: www.elsevier.com/locate/canlet

Original Article

BCL2 induced by LAMTOR3/MAPK is a druggable target of chemoradioresistance in mesenchymal lung cancer

Ok-Seon Kwon [a, 1], Soon-Ki Hong [a, 1], Soo-Jung Kwon [a], Young-Hyun Go [a], Ensel Oh [b], Hyuk-Jin Cha [a, *]

[a] College of Natural Sciences, Department of Life Sciences, Sogang University, Seoul, Republic of Korea
[b] Laboratory of Cancer Genomics and Molecular Pathology, Samsung Biomedical Research Institute, Samsung Medical Center, Seoul, Republic of Korea

ARTICLE INFO

Article history:
Received 7 January 2017
Received in revised form
24 April 2017
Accepted 24 May 2017

Keywords:
Chemoradioresistance
ERK
BCL2
LAMTOR3
Mesenchymal cancer cells
Druggable target

ABSTRACT

Mesenchymal-type cancers after epithelial mesenchymal transition (EMT) were recently shown to acquire chemoresistance through expressing EMT specific transcription factors. However, druggable (or actionable) target(s) for chemoresistance in mesenchymal-type lung cancers remain unidentified. Here, we used a public clinical genomic database and mesenchymal lung cancer cells (MLCC) model derived from the A549 lung adenocarcinoma cell line to demonstrate that *BCL2* expression, which is highly induced in mesenchymal-type lung cancers, as a predictor of poor prognosis in mesenchymal lung cancer patients and association with acquired chemoradioresistance. Thereby, combination treatment with BH3 mimetics, such as ABT-263 and ABT-737, clearly attenuated chemoresistance in MLCCs. *BCL2* expression in MLCCs was induced by ERK1 activity through the upregulation of the MEK1/ERK1 scaffold protein MEK partner-1 (MP1). Interfering with the MEK1/MP1/ERK1 axis using a MEK1 inhibitor or MP1 depletion repressed *BCL2* expression and sensitized MLCCs to chemoradiotherapy. Taken together, our results suggest that targeting druggable proteins in the MEK1/MP1/ERK1/*BCL2* axis, such as MEK1 or *BCL2*, with currently available FDA approved drugs is a currently feasible approach to improve clinical outcomes of mesenchymal lung cancer patients.

Introduction

Despite substantial advances in lung cancer diagnosis and therapy, chemoradioresistance still remains an important obstacle in the treatment of cancer. Epithelial mesenchymal transition (EMT) is a cellular process defined by the loss of epithelial markers such as E-cadherin (encoded by *CDH1*) and the gain of mesenchymal makers such as N-cadherin (encoded by *CDH2*) resulting in consequent acquisition of mesenchymal phenotypes (e.g., increased migration and invasiveness, a typical metastatic properties) [41]. Recent studies revealed that the EMT process is highly involved in chemoresistance in pancreatic cancer [44] and breast cancer [14] rather than in metastasis. Depletion of Snail or Twist [44] or expression of microRNA (miR)-200 [14], which is repressed by Zeb1 [34], sensitizes cancer cells to chemotherapeutic drugs. However, the druggable (or actionable) target(s) in this process to sensitize the mesenchymal cancer cells has yet to be determined.

Most conventional cytotoxic chemotherapies for stage I and II non small cell lung carcinoma (NSCLC), such as etoposide and cisplatin [35], induce apoptosis [28] by upregulating pro-apoptotic genes and activating the mitochondrial apoptotic pathway. Cancer cells evade mitochondrial apoptosis by upregulating anti-apoptotic genes such as *BCL2* family to stabilize mitochondrial membrane potential (MMP) [17], making anti-apoptotic factors promising therapeutic targets [21]. Accordingly, ABT-263 (Navitoclax®), a *BCL2* homology 3 (BH3) mimic small molecule inhibitor, is awaiting FDA approval as a 'first-in-class' drug [30], and its effect on chemoresistance was demonstrated in multiple types of cancer cells [11]. On the other hand, induction of BCL-XL, a *BCL2* family anti-apoptotic protein, enhances chemoresistance in mesenchymal breast cancer cells [22], while BCL-XL promotes metastasis in an anti-apoptotic independent manner [12]. Similar results were reported with *BCL2* [45] or BCL-W [23], suggesting that *BCL2* family proteins contribute to mesenchymal cancer characteristics, and are involved not only in metastasis or invasion but also in chemoresistance.

Accordingly, mesenchymal cancer cell properties (e.g. chemoresistance) can be determined by signaling pathways associated with the modulation of *BCL2* expression. *BCL2* transcription is

* Corresponding author. College of Natural Sciences, Department of Life Sciences, Sogang University, 35 Baekbeom-ro, Mapo-gu, Seoul, 04107, Republic of Korea.
E-mail address: hjcha@sogang.ac.kr (H.-J. Cha).
[1] These authors contribute equally.

http://dx.doi.org/10.1016/j.canlet.2017.05.019
0304-3835/

Cell viability assay and proliferation assay

To measure the cell viability, Cell proliferation assay kit II (XTT) (Roche) was applied followed by manufacture's instruction. For the growth curve with cell proliferation, JuLI stage (NanoEntek) was used. After cells seeded, cells were loaded on JuLI stage for two days. The cell growth was monitored in timely dependent manner.

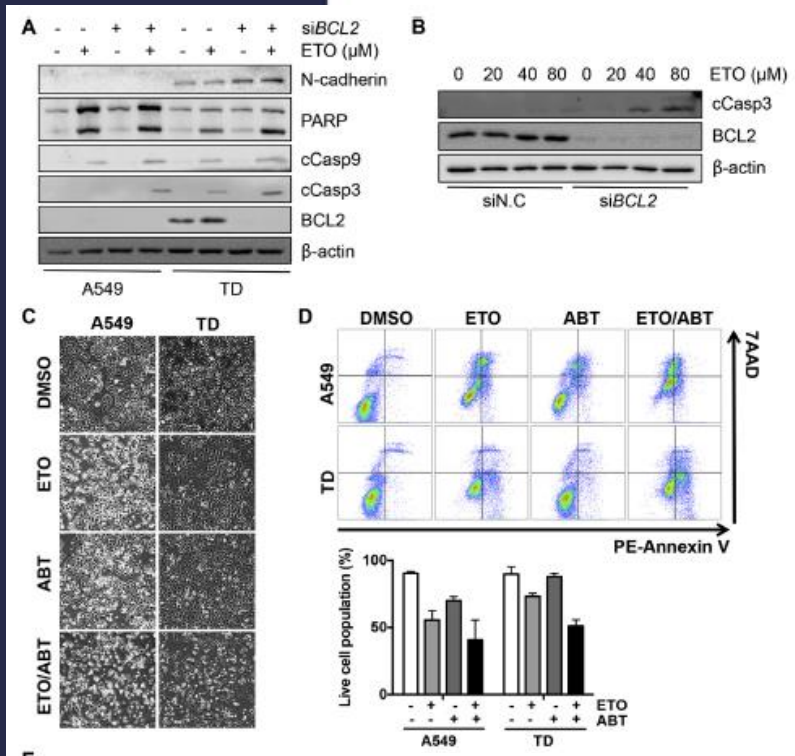

Fig. 4. Inhibition of *BCL2* overcomes chemoresistance in TD cells. (A) Cell death with Etoposide (ETO: 80 μM) treatment after *BCL2* siRNA transfection (siBCL2) was measured with immunoblotting for N-cadherin, PARP, cCasp9 and cCasp3. β-actin was used as an equal loading control. (B) Immunoblotting for cCasp3 with Etoposide (ETO; μM) treatment in dose dependent manner after *BCL2* siRNA transfection. (C and D) Light microscopic image (ABT: ABT-263, ETO/ABT: co-treatment). (C) Flow cytometry plot of Annexin V and 7-AAD (D, upper panel) and quantification bar graph of flow cytometry (D, lower panel) of A549 and TD cells after indicated treatment of Etoposide (ETO; 80 μM) and ABT-263 (ABT: 2 μM). (E) Cell death were measured with Immunoblotting for PARP after combination treatment of ABT-263 (ABT: 2 μM) and Etoposide (ETO) concentration dependent manner. α-tubulin was used as an equal loading control. (F) Immunoblotting for PARP, cCasp9 and cCasp3 after combination treatment with single dose of ABT-263 (ABT: 2 μM) and Etoposide (ETO: 80 μM). (G) Flow cytometry plot of MMP (left) and quantification graph (right) after indicated treatment of ABT-263 (ABT: 2 μM) and Etoposide (ETO: 80 μM).

Biochemistry and Biophysics Reports 11 (2017) 161–173

Contents lists available at ScienceDirect

Biochemistry and Biophysics Reports

journal homepage: www.elsevier.com/locate/bbrep

An evolutionary perspective on the role of mesencephalic astrocyte-derived neurotrophic factor (MANF): At the crossroads of poriferan innate immune and apoptotic pathways

Dayane Sereno, Werner E.G. Müller, Melanie Bausen, Tarek A. Elkhooly, Julia S. Markl, Matthias Wiens*

Institute for Physiological Chemistry, University Medical Center, Johannes Gutenberg-University, Duesbergweg 6, D-55128 Mainz, Germany

ARTICLE INFO

Keywords
MANF
Evolution
Porifera
Apoptosis
Innate immunity
ER stress

ABSTRACT

The mesencephalic astrocyte-derived neurotrophic factor (MANF) belongs to a recently discovered family of neurotrophic factors. MANF can be secreted but is generally resident within the endoplasmic reticulum (ER) in neuronal and non-neuronal cells, where it is involved in the ER stress response with pro-survival effects. Here we report the discovery of the MANF homolog SDMANF in the sponge *Suberites domuncula*. The basal positioning of sponges (phylum Porifera) in the animal tree of life offers a unique vantage point on the early evolution of the metazoan-specific genetic toolkit and molecular pathways. Since sponges lack a conventional nervous system, SDMANF presents an enticing opportunity to investigate the evolutionary ancient role of these neurotrophic factors. SDMANF shares considerable sequence similarity with its metazoan homologs. It also comprises a putative protein binding domain with sequence similarities to the Bcl-2 family of apoptotic regulators. In Suberites, SDMANF is expressed in the vicinity of bacteriocytes, where it co-localizes with the toll-like receptor SDTLR. In transfected human cells, SDMANF was detected in both the organelle protein fraction and the cell culture medium. The intracellular SDMANF protein level was up-regulated in response to both a Golgi/ER transport inhibitor and bacterial lipopolysaccharides (LPS). Upon LPS challenge, transfected cells revealed a decreased caspase-3 activity and increased cell viability with no inducible Bax expression compared to the wild type. These results suggest a deep evolutionary original cytoprotective role of MANF, at the crossroads of innate immune and apoptotic pathways, of which a neurotrophic function might have arisen later in metazoan evolution.

1. Introduction

Neurotrophic factors are growth factors with key regulatory function in various processes such as development, differentiation, and apoptosis of neurons and associated cells. In vertebrates, several structurally and functionally related neurotrophic factors have been well characterized and grouped into a common family termed neurotrophins, including nerve growth factor (NGF), brain-derived neurotrophic factor (BDNF), and neurotrophin-3, and -4/5 [1]. However, neurotrophic signaling does not only occur in vertebrates but several protein homologs of neutrophins and their receptors have already been discovered in hemichordate [2], echinoderm [2], ecdysozoan (insects [3]; crustaceans [4]), and lophotrochozoan species (mollusks [5]; annelids [6]). In contrast, in early branching Metazoa no such homologs have been identified, although a neuronal system is present in Cnidaria [7]; and even for Placozoa (Trichoplax) and Porifera (sponges), with their simple body plan, their limited number of cell types and lack of conventional tissues, structural and molecular evidence has been gathered for some kind of neuronal-like signaling and a (pre-)nervous system [8,9].

With the mesencephalic astrocyte-derived neurotrophic factor (MANF; also known as ARMET [arginine-rich, mutated in early stage tumors]) and its paralog, the cerebral dopamine neurotrophic factor (CDNF), a novel family of neurotrophic factors was previously discovered that is structurally and functionally unrelated to classical neurotrophins [10,11]. In contrast to these neurotrophins, both proteins reside mostly in the ER and Golgi complex and only a small portion is secreted [12,13]. MANF and CDNF are expressed in a wide range of neuronal and non-neuronal tissue types in both embryonic and adult organisms [14]. Both proteins promote cell survival, possibly by inhibiting ER stress-induced apoptotic pathways [12,15,16]. This type of cell death is generally associated with neurodegenerative, neurode-

* Corresponding author.
E-mail address: wiens@uni-mainz.de (M. Wiens).

http://dx.doi.org/10.1016/j.bbrep.2017.02.009
Received 22 December 2016; Received in revised form 17 February 2017; Accepted 27 February 2017
Available online 18 March 2017

For live cell imaging, cells were cultivated in 24-well plates to 40% confluency before LPS treatment. At the same time, the medium was supplement per well with (i) 5 µM NucView 488 caspase-3 substrate, 50 µl propidium iodide (PI), and (iii) 50 µl Hoechst 33342. The latter two reagents were part of the ReadyProbes Cell Viability Imaging Kit (Thermo Fisher Scientific) and used for staining nuclei of dead cells with compromised cell membranes (PI) or nuclei of all cells (Hoechst). Fluorescence was monitored in real-time with an automated cell imaging system (JuLI Stage; VWR) using the following wavelength settings: $Ex_{466\ nm}/Em_{525\ nm}$ (NucView 488), $Ex_{525\ nm}/Em_{580\ nm}$ (PI), and $Ex_{390\ nm}/Em_{452\ nm}$ (Hoechst).

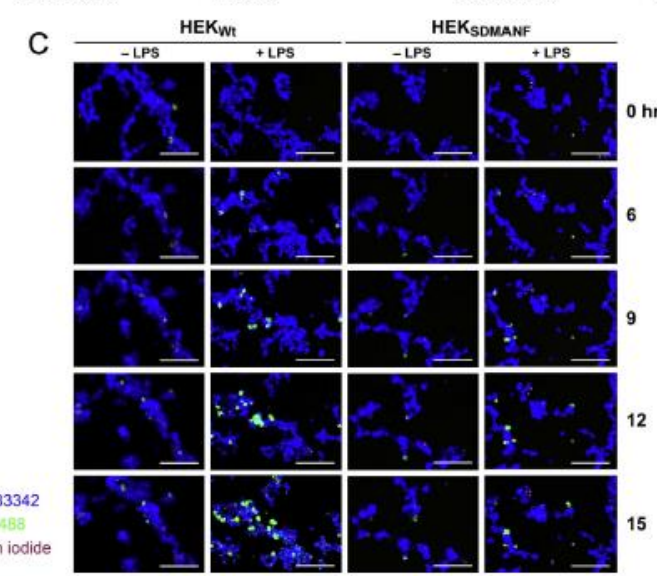

Fig. 7. Viability and caspase activity of HEK cells upon exposure to LPS. Activities of intracellular live-cell proteases (viability, A) and caspase-3 (B) were assessed with the cell-permeant fluorogenic substrates GF-AFC and NucView 488 respectively. Fluorescence was measured in wild type (Wt), mock transfected, and SDMANF-transfected cells that had remained untreated (white bars) or that had been incubated with LPS for 12 h (gray). Values are expressed as the mean ± SD of four independent experiments, compared by ANOVA, followed by the post-hoc Tukey HSD test. *$p < 0.01$ versus untreated control. (C) Fluorescence micrographs of HEK cells recorded in real-time with an automated cell imaging system. Wild type (HEK_{Wt}) and SDMANF-transfected cells (HEK_{SDMANF}) were exposed to LPS for the indicated time. Concurrently, the cells were incubated with Hoechst 33342 to stain nuclei of all cells (blue), NucView 488 to detect caspase-3 activity (green), and propidium iodide to stain nuclei of dead cells (red). Scale bars, 200 µm.

INTERNATIONAL JOURNAL OF ONCOLOGY 52: 201-210, 2018

Anticancer effects of methanol extract of *Myrmecodia platytyrea* Becc. leaves against human hepatocellular carcinoma cells via inhibition of ERK and STAT3 signaling pathways

ANNA JU, YOUNG-CHANG CHO, BA REUM KIM, SEWOONG LEE, HIEN THI THU LE, HUONG LAN VUONG and SAYEON CHO

Laboratory of Molecular and Pharmacological Cell Biology, College of Pharmacy, Chung-Ang University, Seoul 06974, Republic of Korea

Received August 24, 2017; Accepted October 7, 2017

DOI: 10.3892/ijo.2017.4178

Abstract. *Myrmecodia platytyrea* Becc., a member of the Rubiaceae family, is found throughout Southeast Asia and has been traditionally used to treat cancer. However, there is limited pharmacological information on this plant. We investigated the anticancer effects of the methanol extract of *Myrmecodia platytyrea* Becc. leaves (MMPL) and determined the molecular mechanisms underlying the effects of MMPL on metastasis in human hepatocellular carcinoma (HCC) cells. MMPL dose-dependently inhibited cell migration and invasion in SK-Hep1 and Huh7 cells. In addition, MMPL strongly suppressed the enzymatic activity of matrix metalloproteinases (MMP-2 and MMP-9). Diminished telomerase activity by MMPL resulted in the suppression of both telomerase activity and telomerase-associated gene expression. The levels of urokinase-type plasminogen activator receptor (uPAR) expression as well as the phosphorylation levels of signal transducer and activator of transcription 3 (STAT3) and extracellular signal-regulated kinase (ERK) were also attenuated by MMPL. The above results collectively suggest that MMPL has anticancer effects in HCC and that MMPL can serve as an effective therapeutic agent for treating human liver cancer.

Introduction

Cancer is one of the greatest public health burdens worldwide, causing abnormal cell growth through DNA mutation that often leads to death (1). Meta result in 90% of human cancer de contributes to both morbidity and challenging target of effective can cells detach from the primary t through the circulatory or lym and proliferate in distant organs able and fatal diseases (3,4). Rec understanding the precise mechan prevent various steps in the proces

In addition, there is emergin is a promising target for the de therapies (6,7). Elevated telomer in approximately 90% of cancer be immortalized by maintaining is regulated by telomerase. Reactivation or increased expression of telomerase leads to continuous proliferation of cancer cells (9).

Natural products have been used in human medicine since ancient times. For several decades, plants and plant-derived compounds have been used to combat cancer often with fewer side effects than traditional treatments (10). Since plants have been a useful source of approved anticancer agents, many efforts have been undertaken to investigate the wide range of pharmacological effects of plants against various types of cancer (11,12).

Myrmecodia (Rubiaceae) is a genus of the epiphytic myrmecophytes or ant-plant, which is locally known as Sarang Semut. This genus is native to Southeast Asia, but it can also be found in Myanmar, Indochina, and northern Queensland in Australia (13). *Myrmecodia* plants contain a highly specialized tuber and modified stems, which are used by ant colonies (14). *Myrmecodia* species have traditionally been used to treat diseases such as ulcers, tumors, cancer, hepatitis, and coronary artery disease (15).

In pharmacological studies, *Myrmecodia pendens* and *tuberose* are both considered to be potential anticancer agents. Water extracts of *Myrmecodia pendens* have been shown to inhibit HeLa and MCM-B2 cancer cell growth (16). Five flavonoids of *Myrmecodia pendens*, kaempferol, luteolin, rutin, quercetin, and apigenin, were identified and quantified, and

Correspondence to: Professor Sayeon Cho, Laboratory of Molecular and Pharmacological Cell Biology, College of Pharmacy, Chung-Ang University, 84 Heukseok-Ro, Dongjak-Gu, Seoul 06974, Republic of Korea
E-mail: sycho@cau.ac.kr

Key words: methanol extract of *Myrmecodia platytyrea* leaves, urokinase-type plasminogen activator receptor, extracellular signal-related kinase, signal transducer and activator of transcription 3

Wound healing assay. SK-Hep1 and Huh7 cells were seeded in 6-well plates (0.5-1x10^6 cells/well) and cultured until they reached 90% confluence. The wound area was created using a scratcher tip (0.5 mm; SPL Life Sciences, Gyeonggi-do, Korea). The detached cells were removed with phosphate-buffered saline (PBS) supplemented with media containing 1% FBS and treated with the indicated concentration of MMPL for 24 h. The cells that migrated into the wound surface were observed using a JuLI Stage Real-Time Cell History Recorder (NanoEnTek Inc., Seoul, Korea). The change in wound closure is represented as the percent of wound recovery. All experiments were performed in triplicate.

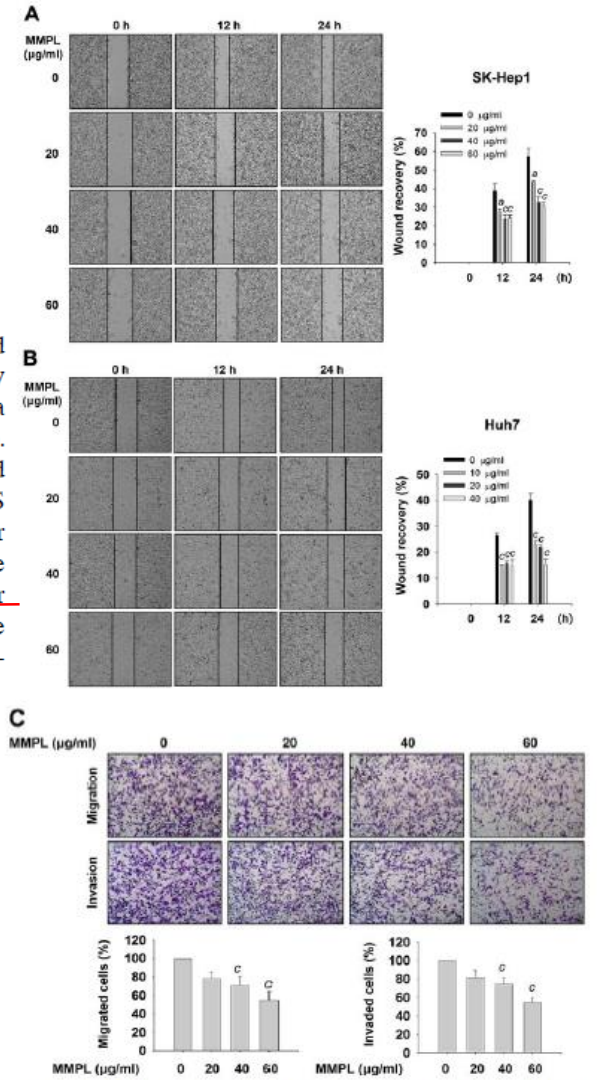

Figure 2. Effects of MMPL on cell migration and invasion. After SK-Hep1 and Huh7 cells were scratched with a scratcher tip, (A) SK-Hep1 cells with MMPL (0, 20, 40 and 60 μg/ml) and (B) Huh7 cells with MMPL (0, 10, 20 and 40 μg/ml) were incubated in cell culture media containing 1% FBS for 24 h. Cell motility was quantified by measuring the percent of wound recovery area compared to the zero time-point. (C) SK-Hep1 cells with MMPL (0, 20, 40 and 60 μg/ml) in media containing 1% FBS were seeded into upper chamber wells that were coated with or without the Matrigel. The lower chambers were filled with media containing 10% FBS. After incubation for 18 h, cells that penetrated the lower surface of the filter were fixed and stained with crystal violet. Quantification of migrated and invaded cells was performed by counting cells in five random fields. Data shown are a representative of three experiments and expressed as the means ± SEM (n=3). ^{a}p<0.05 and ^{c}p<0.001 relative to the MMPL-untreated control group.

Biomaterials 143 (2017) 65–78

Contents lists available at ScienceDirect

Biomaterials

journal homepage: www.elsevier.com/locate/biomaterials

An ultra-effective method of generating extramultipotent cells from human fibroblasts by ultrasound

Yong Seung Lee [a, b, 1], Hyejung Heo [a, b, 1], Jonghwan Lee [a, b], Sung Ung Moon [a, b], Woon Yong Jung [c], Yong Keun Park [d], Min Geun Park [d], Seung-Hun Oh [e], Soonhag Kim [a, b, *]

[a] Institute for Bio-Medical Convergence, College of Medicine, Catholic Kwandong University, Gangneung-si, Gangwon-do, 270-701, Republic of Korea
[b] Catholic Kwandong University International St. Mary's Hospital, Incheon Metropolitan City, 404-834, Republic of Korea
[c] Department of Pathology, Catholic Kwandong University International St. Mary's Hospital, Incheon Metropolitan City, 404-834, Republic of Korea
[d] Department of Surgery, Catholic Kwandong University International St. Mary's Hospital, Incheon Metropolitan City, 404-834, Republic of Korea
[e] Department of Neurology, CHA Bundang Medical Center, CHA University, Seongnam, Republic of Korea

ARTICLE INFO

Article history:
Received 5 June 2017
Accepted 24 July 2017
Available online 25 July 2017

Keywords:
Ultrasound
Influx of extracellular environment
Chromatin remodeling
Cellular reprogramming
Multipotent cells
Human fibroblast

ABSTRACT

Multipotent cells have similar basic features of all stem cells but limitation in ability of self-renewal and differentiation compared with pluripotent cells. Here, we have developed an ultra effective, gene- and chemical-free method of generating extra multipotent (xpotent) cells which have differentiation potential more than limited cell types, by the mechanism of ultrasound-directed permeation of environmental transition-guided cellular reprogramming (Entr). Ultrasound stimulus generated a massive number of Entr-mediated xpotent (x/Entr) spheroids from human dermal fibroblasts (HDFs) 6 days after treatment. The emergence of x/Entr was first initiated by the introduction of human embryonic stem cell (ESC) environments into the HDFs to start fast cellular reprogramming including activation of stress-related kinase signaling pathways, subsequent chromatin remodeling, and expression of pluripotent-related genes via transient membrane damage caused by ultrasound-induced cavitation. And then, pluripotent markers were transported into their adjacent HDFs via direct cell-to-cell connections in order to generate xpotent clusters. The features of x/Entr cells were intermediate between pluripotency and multipotency in terms of pluripotency with three germ layer markers, multi-lineage differentiation potential, and no teratoma formation. This physical stimulus-mediated reprogramming strategy was cost-effective, simple, quick, produced significant yields, and was safe, and can therefore provide a new paradigm for clinical application.

1. Introduction

Pluripotent stem cells are clinically important as disease models and transplants because they can give rise to any type of cell or tissue in the body. However, teratoma formation, which is associated with the tumorigenic potential of pluripotent cells, is a major concern for their clinical application [1]. Therefore, stem cells possessing the advantages of both pluripotent and multipotent cells could provide a safe source for cellular therapy. However, since global gene expression has been shown to differ more than 10% between somatic cells and their derived reprogrammed cells [2], it may be difficult to achieve safe, fast, and efficient cellular reprogramming with current molecular and chemical methods, which target only a few pluripotent or multipotent genes. Cells are composed primarily of water, inorganic molecules, and organic molecules; genetic elements are only a small constituent. Therefore, an environmental influx that triggers a polygenic trait is one alternative for efficiently generating the phenotypic features of reprogrammed cells. Ultrasound-induced cavitation, which causes cellular uptake of biomolecules from the environment, has been shown to have a positive effect on cellular development [3–8]. Here we employed ultrasound-directed permeation of environmental transition-guided cellular reprogramming (Entr), which uses

* Corresponding author. Institute for Bio-Medical Convergence, College of Medicine, Catholic Kwandong University, Gangneung-si, Gangwon-do, 270-701, Republic of Korea.
E-mail address: kimsoonhag@empas.com (S. Kim).
[1] These authors contributed equally to this work.

http://dx.doi.org/10.1016/j.biomaterials.2017.07.033
0142-9612/

2.24. Time-lapse imaging

For live cell microscopic imaging of spheroid formation, images were acquired for 50 h at a rate of one frame every 5 min for UCUM-S and UCUM-A and for 3 days at a rate of one frame every 10 min for mUCUM-S using a JuLI™ FL instrument (NanoEnTek Inc, Seoul, Korea). To monitoring *Oct4* expression of x/Entr cells after ultrasound stimulus, we infected HDF cells with lentivirus containing pGreenZeo-*hOct4* reporter vector (pGreenZeo™ pGZ-*hOct4* Reporter Construct, SBI, Mountain View, USA). The pGreenZeo-*hOct4* reporter vector contain promoter regions for *Oct4* gene that indicate pluripotency. The infected HDF cells are showed *GFP* fluorescence (excitation/emission, 482/502 nm) when *Oct4* expression. Virus was added a multiplicity of infection (MOI) of 5 to HDF cells, and then cultured in DMEM culture media supplemented with 10% FBS and 5 μl/ml TransDux (SBI). After 3 days incubation, the virus was removed and fresh culture media (except TransDux) added. The infected HDF cells were treated with ultrasound energy (1 W/cm^2, 5 s), and the expression of *GFP* in x/Entr cell was captured at a rate of one frame every 10 min for 42 h 20 min on an IX3-ZDC fluorescence microscope (Olympus). Cells were incubated at 37 °C in a 5% CO_2 atmosphere throughout image collection. A single cluster of x/Entr or m-x/Entr cells was plated in an incubator chamber (LCI, Seoul, Korea) on day 6 for the proliferation assay. Images were captured at a rate of one frame every 10 min for 3 days or 36 h on an IX3-ZDC fluorescence microscope stage while cells were maintained at 37 °C in a 5% CO_2 atmosphere. Immediately after ultrasonic stimulation, x/Entr cells in the incubator chamber were stained with the Live/Dead assay kit and imaged at a rate of one frame every 10 min for 66 h on an IX3-ZDC fluorescence microscope stage maintained at 37 °C in a 5% CO_2 atmosphere. QD605s were added to the medium of x/Entr cells, and the influx of QD605s into x/Entr cells or a single x/Entr cell was monitored at a rate of one frame every 10 min for 18 h using a JuLI™ Stage instrument (NanoEnTek Inc) or at a rate of one frame every 3 s for 1 h on a confocal laser scanning microscope (LSM 700, Carl Zeiss), respectively.

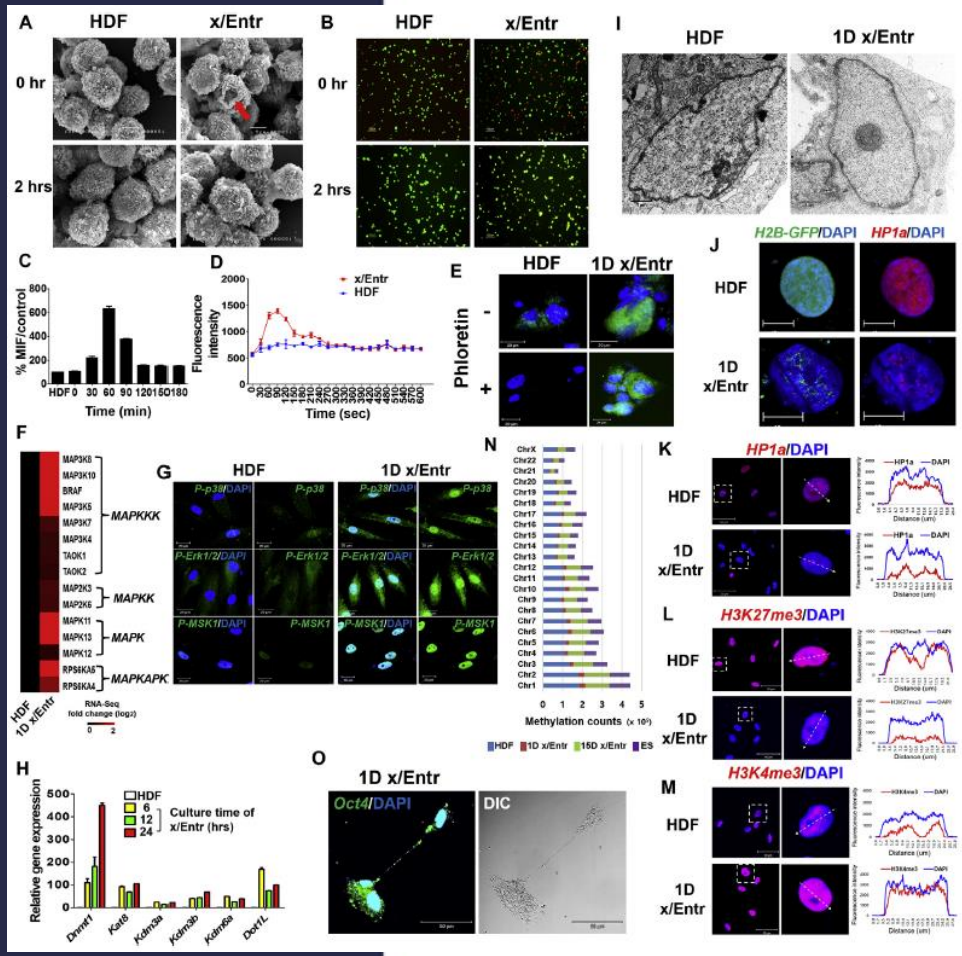

Fig. 3. Mechanisms of generating x/Entr cells. (**A**), Scanning electron microscope images of x/Entr cells immediately (0 h) and 2 h after ultrasonic stimulation. Red arrow; pore formed on membrane by ultrasound stimulus. Scale bars, 5 μm. (**B**), Membrane damage and recovery of x/Entr cells immediately (0 h) and 2 h after ultrasonic stimulation. Live/dead kit staining of x/Entr cells was separately conducted 0 and 2 h after ultrasonic stimulation. Live cell or intact membrane; green, Dead cell or damaged membrain; red, Partial damage; double staining. Scale bars, 100 μm. (**C**), Fluorescence analysis of H_2O_2 levels in x/Entr cells for 3 h after ultrasound stimulus using the CM-H2DCFDA dye. (**D**), Analysis of intracellular Ca^{2+} concentrations in x/Entr cells for 10 min after ultrasound stimulus by Fluo-4 dye. Blue line; HDF cells, Red line; x/Entr cells. (**E**), Confocal microscopy analysis of glucose uptake of 1-day-old x/Entr cells in the absence (−) or presence (+) of phloretin. Glucose uptake was indicated to green fluorescent by Glu-Tracker reagent. Phloretin was used as a glucose uptake blocker. Scale bars, 20 μm. (**F**), RNA-Seq analysis of MAPK-mediated upstream and downstream kinase signaling pathways of 1-day-old x/Entr cells. (**G**), Confocal microscopy images of phosphorylated *p38, Erk1/2,* and *MSK1* of 1-day-old x/Entr cells. Scale bars, 20 μm. (**H**), Relative mRNA expression of epigenetic regulators of 1-day-old x/Entr cells for 24 h by real-time PCR analysis. The quantitative results of mRNA was normalized by GAPDH. (**I**), Transmission electron micrographs of 1-day-old x/Entr cells. scale bars, 1 μm. (**J**), Confocal microscopy analysis of *H2B* and *HP1α* in an x/Entr cell at 24 h post-ultrasonic stimulation. *GFP* (green) designates *H2B*, which compacts DNA into chromatin (indicated by *H2B-GFP*). Scale bars, 10 μm. Immunocytochemical analysis of *HP1α* (**K**), *H3K27me3* (**L**) and *H3K4me3* (**M**) in 1-day-old x/Entr cells. White dotted arrows of the zoomed cells (white boxes) indicate the line scans of showing the intensity plots. Scale bars, 50 μm. (**N**), Total number of methylation peaks per chromosome for 1-day-old x/Entr cells (1D x/Entr). 15-day-old x/Entr cells (15D x/Entr) were used as a reference. (**O**), *Oct4* transport by direct cell-to-cell interaction of x/Entr cells. Scale bars, 50 μm. (For interpretation of the references to colour in this figure legend, the reader is referred to the web version of this article.)

ARTICLE IN PRESS

The American Journal of Pathology, Vol. 188, No. 1, January 2018

ELSEVIER

The American Journal of PATHOLOGY

ajp.amjpathol.org

TUMORIGENESIS AND NEOPLASTIC PROGRESSION

Neurotrophin Receptors TrkA, p75^{NTR}, and Sortilin Are Increased and Targetable in Thyroid Cancer

Sam Faulkner,*† Philip Jobling,*† Christopher W. Rowe,†§ S.M. Rodrigues Oliveira,*† Severine Roselli,*† Rick F. Thorne,† Christopher Oldmeadow,†¶ John Attia,†‡ Chen Chen Jiang,†‡ Xu Dong Zhang,*† Marjorie M. Walker,†‖ and Hubert Hondermarck*†

From the School of Biomedical Sciences & Pharmacy, Faculty of Health and Medicine, the Hunter Medical Research Institute,† the School of Mathematical and Physical Sciences,¶ Faculty of Science and Information Technology, and the School of Medicine & Public Health,‡ Faculty of Health and Medicine, University of Newcastle, Callaghan, New South Wales; and the Departments of Endocrinology§ and Anatomical Pathology,‖ John Hunter Hospital, Callaghan, New South Wales, Australia*

Accepted for publication September 21, 2017.

Address correspondence to Hubert Hondermarck, Ph.D., School of Biomedical Sciences & Pharmacy, University of Newcastle, Life Sciences Building, Callaghan, NSW 2308, Australia. E-mail: hubert.hondermarck@newcastle.edu.au.

Neurotrophin receptors are emerging targets in oncology, but their clinicopathologic significance in thyroid cancer is unclear. In this study, the neurotrophin tyrosine receptor kinase TrkA (also called NTRK1), the common neurotrophin receptor p75^{NTR}, and the proneurotrophin receptor sortilin were analyzed with immunohistochemistry in a cohort of thyroid cancers (n = 128) and compared with adenomas and normal thyroid tissues (n = 62). TrkA was detected in 20% of thyroid cancers, compared with none of the benign samples (P = 0.0007). TrkA expression was independent of histologic subtypes but associated with lymph node metastasis (P = 0.0148), suggesting the involvement of TrkA in tumor invasiveness. Nerves in the tumor microenvironment were positive for TrkA. p75^{NTR} was overexpressed in anaplastic thyroid cancers compared with papillary and follicular subtypes (P < 0.0001). Sortilin was overexpressed in thyroid cancers compared with benign thyroid tissues (P < 0.0001). Neurotrophin receptor expression was confirmed in a panel of thyroid cancer cell lines at the mRNA and protein levels. Functional investigations using the anaplastic thyroid cancer cell line CAL-62 found that siRNA against TrkA, p75^{NTR}, and sortilin decreased cell survival and cell migration through decreased SRC and ERK activation. Together, these data reveal TrkA, p75^{NTR}, and sortilin as potential therapeutic targets in thyroid cancer. *(Am J Pathol 2018, 188: 1–13; https://doi.org/10.1016/j.ajpath.2017.09.008)*

Thyroid cancer is the most common endocrine malignant tumor. Most tumors are derived from thyroid follicular epithelial cells, including papillary thyroid carcinoma (PTC), follicular thyroid carcinoma (FTC), and undifferentiated anaplastic thyroid carcinoma (ATC), whereas medullary thyroid carcinoma (MTC) is derived from neuroendocrine parafollicular cells. Worldwide, the incidence of thyroid cancer is increasing.[1] In part, this is explained by increased detection of indolent disease,[2] and there is a need for improved diagnostic strategies for clinically significant carcinomas.[3] However, recent data have indicated an increase in mortality during the past 3 decades for patients diagnosed with advanced thyroid cancer, suggesting not only a true increase in incidence but also the need for novel treatment strategies for this subgroup.[4] In particular, ATC, the most lethal histologic subtype, carries a high mortality rate, with median survival of <1 year after diagnosis.[5] Thus, the identification of new targets for the diagnosis and treatment of clinically significant thyroid cancer is essential.

Neurotrophin receptors are known to be overexpressed in some human cancers, where they participate in the stimulation of tumor growth and dissemination.[6,7] In particular, recent data have indicated the crucial stimulatory impact of nerve growth factor (NGF) in gastric[8] and pancreatic cancer,[9] where targeting NGF resulted in a strong reduction of tumor growth and metastasis. In thyroid cancer, the overexpression of the precursor for NGF (proNGF) has been

Supported by the University of Newcastle (Australia) and the Hunter Cancer Research Alliance.

Disclosures: None declared.

https://doi.org/10.1016/j.ajpath.2017.09.008

FLA 5.5.0 DTD ■ AJPA2749_proof ■ 16 November 2017 ■ 4:49 am ■ EO: 2017_308

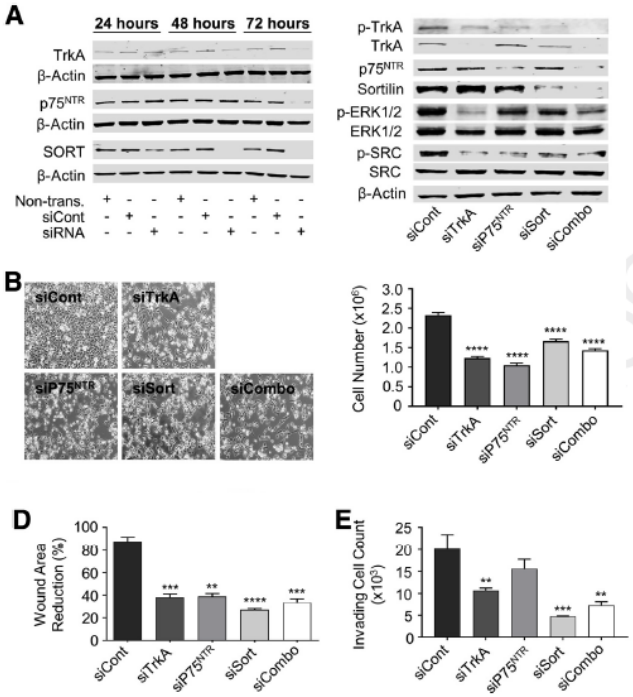

Figure 6 Impact of targeting TrkA, p75^{NTR}, and sortilin in the CAL-62 anaplastic thyroid cancer cell line. CAL-62 cells were transfected with siRNA against TrkA (siTrkA), p75^{NTR} (siP75^{NTR}), and sortilin (siSort), alone and in combination (siCombo), as well as with a universal negative control siRNA (siCont). **A:** Effect of siRNA on protein levels and cell signaling. The impact of siRNA transfection in inhibiting the protein level of TrkA, p75^{NTR}, and sortilin was measured by Western blot analysis 24, 48, and 72 hours after transfection. Non-transfected cells (nontrans.) were also analyzed. β-Actin protein expression was used as an equal loading control. TrkA protein level significantly decreases after 48 hours and further at 72 hours. p75^{NTR} protein level is inhibited after 72 hours. Sortilin is completely decreased after 48 and 72 hours. For cell signaling, siTrkA and siCombo decreased the level of phosphor-TrkA (p-TrkA), phosphor-ERK1/2 (p-ERK1/2), and phospho-SRC (p-SRC). siP75^{NTR} and siSort decrease p-ERK1/2 and p-SRC. **B:** Cell growth. The number of cells was measured by cell counting at 72 hours after transfection, and siRNA-treated cells were compared with siCont cells. SiRNA against TrkA, p75^{NTR}, and sortilin, alone or combined (siCombo), all significantly inhibit cell growth. **C:** Apoptosis. The proportion of apoptotic cells was measured in flow cytometry using Annexin V, and siRNA-treated cells were compared with siCont cells. siRNA against TrkA, p75^{NTR}, and sortilin, alone or in combination, all increase the percentage of apoptotic cells compared with siCont. The numbers indicate the percentages of the cells represented by alive, apoptotic, and dead populations. **D:** Cell migration. Scratching of the cell monolayer was performed 72 hours after transfection with siRNA, and reduction in gap area was measured 20 hours later. Targeting of all three receptors, alone and in combination (siCombo), resulted in the inhibition of wound scratch healing. **E:** Cell invasion. Transwell assays were set up 72 hours after siRNA transfection, and cells were allowed to invade for 20 hours. Only siSort and siTrkA, and siCombo significantly inhibited cancer cell invasion. Data are expressed as means ± SD (**B**, **D**, and **E**). Data are representative of at least three technical replicates, each consisting of at least three biological replicates. $^{**}P < 0.01$, $^{***}P < 0.001$, and $^{****}P < 0.0001$.

Cell Migration and Wound-Healing Assay

A total of 5 × 10^5 ATC cells (CAL-62 and 8505c) were seeded on 6-well plates in complete growth medium (RPMI containing 10% FCS and 2 mmol/L L-glutamine) and were allowed to adhere overnight in a humidified incubator at 37°C and 5% CO_2. Cells were transfected the following day with siTrkA, siP75^{NTR}, siSort, a combination of the three siRNAs (siCombo), or control siRNA (siCont). After 72 hours, during which the cells were allowed to grow to confluence, the cell monolayer was scratched with a 200-μL pipette tip, rinsed three times with phosphate-buffered saline to remove floating cellular debris, and replaced with media that contained 0.1% (v/v) FCS. The wound area that resulted from the scratch was monitored using the JuLI Stage automated cell imaging system (NanoEnTek Inc., Seoul, Korea). Images were taken automatically every 5 hours during a 20-hour postscratch period. Results are shown as the percentage reduction of the wound area, measured using ImageJ version 1.60_20 (NIH, Bethesda, MD; *http://imagej.nih.gov/ij*).

Laboratory science

Paracrine effects of mesenchymal stem cells on the activation of keratocytes

Zhixin Jiang,[1,2,3] Guangjie Liu,[4] Fanlan Meng,[1] Weiyi Wang,[5] Peng Hao,[1,2,3] Yang Xiang,[1] Yuchuan Wang,[1,2,3] RuiFang Han,[1,2,3] Fang Li,[2] Liming Wang,[1,2,3] Xuan Li[1,2,3]

[1]Clinical College of Ophthalmology, Tianjin Medical University, Tianjin, China
[2]Nankai University Eye Hospital, Tianjin, China
[3]Tianjin Eye Hospital, Tianjin Eye Institute, Tianjin Key Lab of Ophthalmology and Visual Science, Tianjin, China
[4]Department of Respiratory Medicine, Beijing Tongren Hospital, Capital Medical University, Beijing, China
[5]Department of Ophthalmology, Tianjin Huanhu Hospital, Tianjin, China

Correspondence to
Dr Xuan Li, Tianjin Eye Hospital 300020, Tianjin, China; xuanli08@yahoo.com

ZJ, GL and FM contributed equally.

Received 7 December 2016
Revised 20 June 2017
Accepted 30 July 2017
Published Online First 26 August 2017

ABSTRACT

Aims The purpose of this study is to investigate the impact of mesenchymal stem cell (MSC)-derived soluble factors on the function of keratocytes, with a particular focus on the processes involved in wound healing, including keratocyte activation, migration and proliferation as well as extracellular matrix (ECM) synthesis.

Methods Primary cultured rabbit keratocytes were treated with MSC-conditioned medium (MSC-CM). The paracrine factors released by bone marrow MSCs were examined by ELISA. Time-lapse microscope was used to examine wound closure in vitro. Mouse model of corneal injury was made by epithelial scraping after ethanol injury.

Results MSC-CM significantly increased the wound closure rate of corneal stromal cells in vitro. This enhancement of wound closure by MSC-CM was due to the promotion of cell migration. MSC-CM enhanced keratocyte survival following ethanol injury via inhibiting apoptosis. The expression of ECM component genes in keratocytes was upregulated by MSC-CM. In addition, MSC-CM promoted corneal epithelial wound healing following chemical injury. A number of wound healing mediators were detected in MSC-CM, including vascular endothelial growth factor (VEGF), platelet-derived growth factor (PDGF), hepatocyte growth factor (HGF), transforming growth factor beta 1 (TGFβ1), interleukin 8 (IL8), interleukin 6 (IL6) and monocyte chemoattractant protein 1 (MCP1).

Conclusion MSC secretes certain factors that accelerate corneal re-epithelialisation. The paracrine effects of MSC on corneal wound healing including improvements in cell viability, migration and ECM formation.

INTRODUCTION

The cornea is an avascular tissue of the eye that is transparent to properly refract light. Approximately 90% of the corneal volume consists of the stroma, which is composed of a mixture of lamellae of collagen fibrils, proteoglycans and keratocytes. Keratocytes are responsible for the development and maintenance of collagen and proteoglycans. The unique arrangement of collagen fibrils in the stroma is crucial for corneal transparency. Keratocytes are neural crest-derived mesenchymal cells. On injury, some keratocytes undergo apoptosis, while a fraction of the remaining keratocytes lose their quiescence and transition into activated phenotypes that migrate to the wound site, proliferate and produce the new matrix needed for wound repair.[1] However, in certain types of wounds, some keratocytes transform into myofibroblasts in a process identified to be the primary biological event responsible for the disruption of corneal transparency.[2] Therefore, novel techniques for controlling corneal stromal cells during wound repair events may help to reduce the occurrence of corneal opacity.

Mesenchymal stem cells (MSCs) are multipotent cells derived primarily from adult bone marrow, although recent reports have shown that MSCs are also present in a wide variety of foetal and adult tissues, including adipose tissue, placenta, umbilical cord, dental pulp and cornea.[3 4] MSCs provide an attractive source of cells for tissue repair and regeneration. Current studies of myocardial infarction, acute kidney failure and stroke have shown that MSC therapy has the potential to inhibit cell death and stimulate endogenous regeneration programs.[5] The effects of MSC transplantation are thought to be mediated by an increase in cell protective, angiogenic and mitogenic factors, in addition to the differentiation of transplanted MSCs into specific cell types.[6] It has been shown that the therapeutic effects of MSCs are at least partially mediated by paracrine trophic factors secreted by cells. A number of different growth factors, cytokines and extracellular matrix (ECM) proteins have been identified as constituents of MSC culture media. Reports have shown that soluble factors produced by stem cells have beneficial effects on corneal epithelial recovery from chemical injury.[7] However, few studies have assessed the effects of MSC paracrine factors on corneal keratocytes, which play a key role in corneal stromal wound healing.

Tissue culture models are useful tools for studying keratocyte activation in vitro. When keratocytes isolated from the adult cornea are cultured in media without serum, they maintain a quiescent state and exhibit cellular morphology and matrix secretion similar to keratocytes in vivo. However, when cultured in media containing serum or growth factors, including TGFβ1, TGFβ2 and IL-1α, they acquire morphological and phenotypic characteristics exhibited by activated keratocytes (ie, fibroblasts or myofibroblasts) in vivo.[8 9] In the present study, we investigated the effects of MSC-conditioned medium (MSC-CM) on corneal stromal cells. Using an in vitro model of primary rabbit keratocytes, wound healing activities, such as cell migration, proliferation, survival and ECM

To cite: Jiang Z, Liu G, Meng F, et al. Br J Ophthalmol 2017;101:1583–1590.

Scratch-wound assay

The rate of wound closure in vitro was determined using time-lapse microscope. A confluent monolayer of keratocytes was wounded with a plastic micropipette tip, and the culture medium was replaced with vehicle control medium or MSC-CM. The cells were monitored using the JuLI Stage automated cell imaging system (NanoEnTek, Korea). JuLI Stage software offers image capturing and time-lapse recording with multiposition scanning. The scratch-wound assay was used to capture images at regular intervals during cell migration to close the scratch. All wound closure assays were performed in quadruplicate.

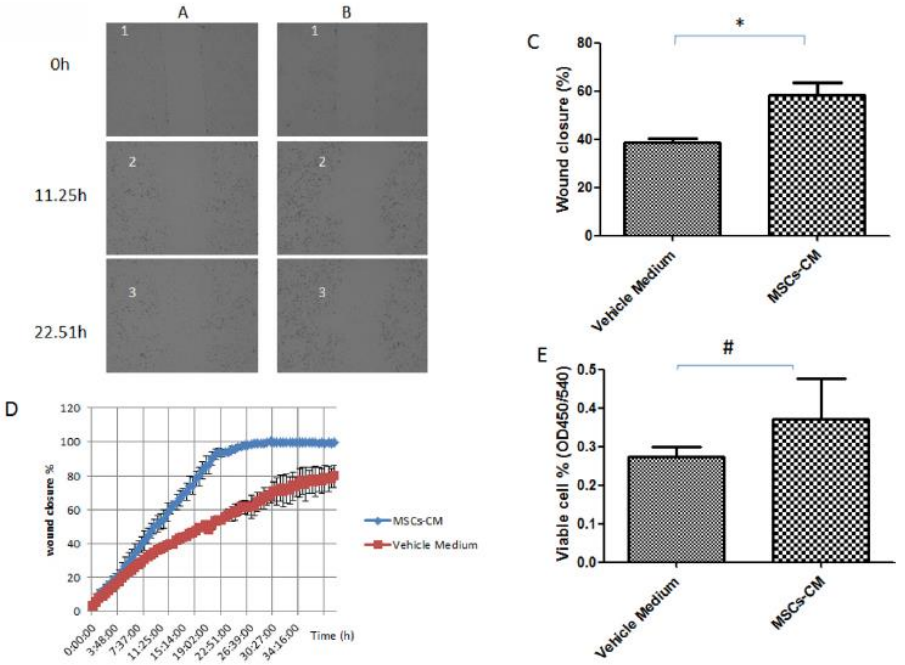

Figure 4 Mesenchymal stem cell conditioned medium (MSC-CM) enhanced the rate of wound closure by corneal stromal cells. Confluent monolayers of keratocytes were grown in MSC-CM (A1–A3) or vehicle control medium (B1–B3) and were scraped by a plastic pipette. (C) The extent of wound closure in a scrape-wound migration assay of corneal stromal cells at 11.25 hours. (D) Change in the wound closure area over time. (E) Cell proliferation (by 3-(4,5-dimethylthiazol-2-yl)−2,5-diphenyltetrazolium bromide assay) was evaluated after 36 hours of wound treatment. Data are presented as the mean±SD from at least in triplicate in three independent experiments. #p<0.05, *p<0.01.

Journal of Virological Methods 252 (2018) 57–64

Contents lists available at ScienceDirect

Journal of Virological Methods

journal homepage: www.elsevier.com/locate/jviromet

Robust real-time cell analysis method for determining viral infectious titers during development of a viral vaccine production process

Cédric Charretier[a], Aure Saulnier[a], Loïc Benair[a], Corinne Armanet[a], Isabelle Bassard[a], Sandra Daulon[a], Bertrand Bernigaud[a,1], Emanuel Rodrigues de Sousa[a], Clémence Gonthier[a], Edouard Zorn[a,2], Emmanuelle Vetter[a], Claire Saintpierre[b], Patrice Riou[a,*], David Gaillac[a]

[a] Sanofi Pasteur, 1541 avenue Marcel Mérieux, 69280, Marcy l'Etoile, France
[b] Rexia, 129 rue Servient, 69003, Lyon, France

ARTICLE INFO

Keywords:
Real-time cell analysis
Impedance
Virus titration
Virus-induced cytopathic effect
Vero cells
Label-free assay

ABSTRACT

The classical cell-culture methods, such as cell culture infectious dose 50% ($CCID_{50}$) assays, are time-consuming, end-point assays currently used during the development of a viral vaccine production process to measure viral infectious titers. However, they are not suitable for handling the large number of tests required for high-throughput and large-scale screening analyses. Impedance-based bio-sensing techniques used in real-time cell analysis (RTCA) to assess cell layer biological status *in vitro*, provide real-time data. In this proof-of-concept study, we assessed the correlation between the results from $CCID_{50}$ and RTCA assays and compared time and costs using monovalent and tetravalent chimeric yellow fever dengue (CYD) vaccine strains. For the RTCA assay, Vero cells were infected with the CYD sample and real-time impedance was recorded, using the dimensionless cell index (CI). The CI peaked just after infection and decreased as the viral cytopathic effect occurred in a dose-dependent manner. The time to the median CI (CIT_{med}) was correlated with viral titers determined by $CCID_{50}$ over a range of about 4–5 $\log_{10}$ $CCID_{50}$/ml. This in-house RTCA virus-titration assay was shown to be a robust method for determining real-time viral infectious titers, and could be an alternative to the classical $CCID_{50}$ assay during the development of viral vaccine production process.

1. Introduction

Micro-scale, high-throughput bioreactor technology is increasingly being used to optimize parameters during virus production process development for vaccine manufacturing (Bareither and Pollard, 2011; Janakiraman et al., 2015). However, the assessment of the optimization relies on classical cell-based end-point assays to measure infectious titers such as cell culture infectious dose 50% ($CCID_{50}$) and plaque forming unit (PFU) assays, which are labor-intensive, expensive and time consuming. In addition, viral infection is sometimes only visible after indirect immune-detection of the endpoint so that 'real-time' data are not available (Hsiung, 1984; Pierson and Diamond, 2007). These classical techniques need to be adapted for vaccine production process development as they are not suitable for the large number of tests required for the high-throughput and large-scale screening technologies used and the short time-frame requirements (Bareither and Pollard, 2011).

Real-time cell analysis (RTCA) systems can be used to measure electrical impedance-based signals that can provide information on the *in vitro* cell layer biological status. Impedance-based bio-sensing techniques give qualitative and quantitative information on the cells, including cell number, their adhesion and spreading, as well as cell morphology and viability, in a label-free system (Atienza et al., 2006; Giaever and Keese, 1991; Solly et al., 2004). Changes in cellular morphology and/or growth rate, referred to as cytopathic effects (CPEs), are early indicators of viral infection and the quantification of these events by measuring impedance can be used to follow and characterize viral growth kinetics (Cheung et al., 2011; Drew et al., 2010; Ebersohn et al., 2014; Fang et al., 2011; Golke et al., 2012; Marlina et al., 2015; Sharma et al., 2011; Teng et al., 2013; Witkowski et al., 2010). The

* Corresponding author at: Sanofi Pasteur, 1541 avenue Marcel Mérieux, Marcy l'Etoile, 69280, France.
E-mail addresses: cedric.charretier@sanofi.com (C. Charretier), aure.saulnier@sanofi.com (A. Saulnier), loic.benair@sanofi.com (L. Benair), corinne.armanet@sanofi.com (C. Armanet), isabelle.bassard@sanofi.com (I. Bassard), sandra.daulon@sanofi.com (S. Daulon), emanuel.rodrigues-de-sousa@sanofi.com (E. Rodrigues de Sousa), clemence.gonthier@sanofi.com (C. Gonthier), en@il-biosystems.com (E. Zorn), emmanuelle.vetter@sanofi.com (E. Vetter), patrice.riou@sanofi.com (P. Riou), david.gaillac@sanofi.com (D. Gaillac).
[1] Present address: Rexia, 129 rue Servient, 69003, Lyon, France.
[2] Present address: Bl. Biosystems, 7 Rue Sainte Odile, Schiltigheim, France.

https://doi.org/10.1016/j.jviromet.2017.11.002
Received 5 April 2017; Received in revised form 24 October 2017; Accepted 4 November 2017
Available online 14 November 2017

2.3.1. Monovalent CYD vaccine virus titration

The following day, 11 serial, 4-fold dilutions of each CYD serotype standard were prepared (concentrations ranging between 2 and 9 $\log_{10}$ $CCID_{50}$/mL depending on the serotype) in MEM supplemented with 10% FCS, 2 mM L-glutamine, 22 mM sodium bicarbonate and penicillin-dihydrostreptomycin (200 U/mL and 50 mg/L, respectively) and 20 mM HEPES. The resulting standard curve was used as a reference in each plate to determine the equivalent $CCID_{50}$ titer for the tested samples. These dilutions were distributed in duplicate and ten-fold serial dilutions of samples to be tested were distributed in triplicate in the 96-well E-plate (Fig. 1). Triplicate dilutions of an internal control, a homologous CYD vaccine virus with a known infectious titer (different from that used for the standard curve), were added to well H10 to H12. The titer of the internal control was plotted on a control chart to assess the overall inter-assay performance. The E-plate was removed from the workstation, 100 µL medium was removed from each well and replaced by 100 µL of the standard or samples dilutions. To measure the background signal, ≥1 well/plate contained only supplemented MEM and ≥1 well/plate contained only Vero cells to measure impedance for an uninfected cell control (Fig. 1). Impedance was measured every 15 min for 7 days after reloading the plate into the incubator. In parallel, time-lapse images were captured (every 60 min at 10X magnification) using a JuLI™ Stage automated imaging system (NanoEntek Inc., Seoul, Korea) from the initiation of viral infection until the end of incubation and a video was generated using JuLI™ Stage software in a classical 96-well plate (without the microelectrode arrays), prepared and seeded in an identical manner.

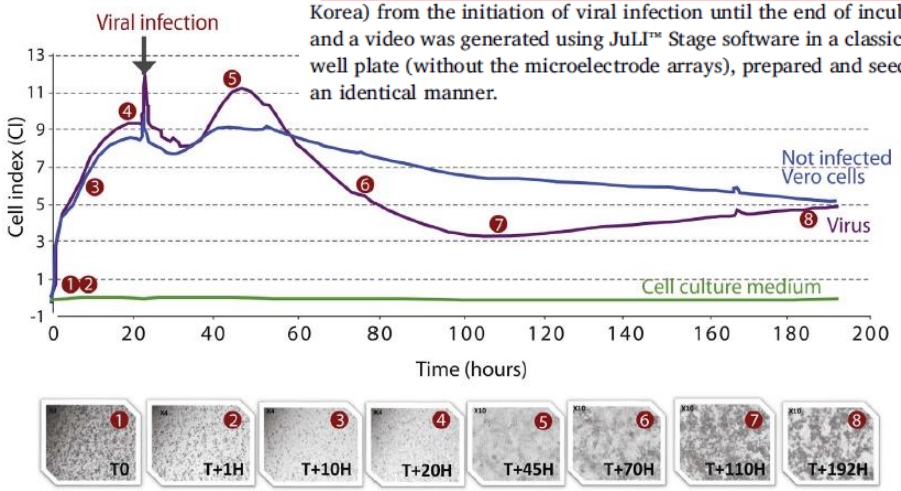

Fig. 2. Real-time cell monitoring following monovalent CYD virus infection. Real-time cell analyses (cell index, CI) showing the differences in growth profile for Vero cells infected with CYD4 compared with uninfected control Vero cells measured in a 96-well E-plate (xCELLigence™, ACEA Biosciences Inc, San Diego, CA). Modifications to the cell layer were monitored in parallel, in standard 96-well plates, through time-lapse images that were captured (using a JuLI™ Stage automated imaging system (NanoEntek Inc., Seoul, Korea); a video was generated using JuLI™ Stage software (also see Supplementary File). Images from the video taken at the times specified are shown and indicated on the timescale in the figure.

Journal of Controlled Release 261 (2017) 287–296

Contents lists available at ScienceDirect

Journal of Controlled Release

journal homepage: www.elsevier.com/locate/jconrel

Pegylated liposomal formulation of doxorubicin overcomes drug resistance in a genetically engineered mouse model of breast cancer

András Füredi[a,b], Kornélia Szebényi[b], Szilárd Tóth[a], Mihály Cserepes[a,c], Lilla Hámori[a], Veronika Nagy[a], Edina Karai[a,d], Péter Vajdovich[d], Tímea Imre[a], Pál Szabó[a], Dávid Szüts[a], József Tóvári[c], Gergely Szakács[a,b,*]

[a] Institute of Enzymology, Research Centre for Natural Sciences, Hungarian Academy of Sciences, P.O.B. 286, Budapest 1519, Hungary
[b] Institute of Cancer Research, Medical University Vienna, Vienna, Austria
[c] Department of Experimental Pharmacology, National Institute of Oncology, Budapest, Hungary
[d] Department of Clinical Pathology and Oncology, Faculty of Veterinary Science, Szent István University, Budapest, Hungary

ARTICLE INFO

Keywords:
Breast cancer
Multidrug resistance
Pegylated liposomal doxorubicin
P-glycoprotein
Genetically engineered mouse model

ABSTRACT

Success of cancer treatment is often hampered by the emergence of multidrug resistance (MDR) mediated by P-glycoprotein (ABCB1/Pgp). Doxorubicin (DOX) is recognized by Pgp and therefore it can induce therapy resistance in breast cancer patients. In this study our aim was to evaluate the susceptibility of the pegylated liposomal formulation of doxorubicin (PLD/Doxil®/Caelyx®) to MDR. We show that cells selected to be resistant to DOX are cross-resistant to PLD and PLD is also ineffective in an allograft model of doxorubicin-resistant mouse B-cell leukemia. In contrast, PLD was far more efficient than DOX as reflected by a significant increase of both relapse-free and overall survival of *Brca1*$^{-/-}$;*p53*$^{-/-}$ mammary tumor bearing mice. Increased survival could be explained by the delayed onset of drug resistance. Consistent with the higher Pgp levels needed to confer resistance, PLD administration was able to overcome doxorubicin insensitivity of the mouse mammary tumors. Our results indicate that the favorable pharmacokinetics achieved with PLD can effectively overcome Pgp-mediated resistance, suggesting that PLD therapy could be a promising strategy for the treatment of therapy-resistant breast cancer patients.

1. Introduction

Chemotherapy remains the principal therapeutic modality in cancer treatment. Despite recent successes, such as the discovery of the BCR-ABL tyrosine kinase inhibitors in chronic myeloid leukemia (CML), all-trans retinoic acid (ATRA) in acute promyelocytic leukemia (APL) and other advances in testicular cancer, pediatric leukemias and Hodgkin's lymphomas, which have demonstrated striking effects on patients survival [1], resistance and relapse remains a major obstacle [2].

Breast cancer is the most common malignancy in women. Approximately 60% of the breast cancer patients diagnosed at an early stage of the disease receive chemotherapy, but only a minor fraction of patients actually benefit from it [3]. 30% of women diagnosed with early stage breast cancer will progress to metastatic disease where there are only few treatment options [4]. Response to anthracycline- or taxane-based treatment regimens is overall weak and not long-lasting [5]. A study concluded that 50–70% of relapsing tumors from surgically removed adenocarcinomas were already drug resistant [6].

Resistance to anticancer agents is based on several mechanisms. Cancer cells can downregulate the drug target, tune down pathways leading to apoptosis, upregulate DNA repair mechanisms or increase the metabolism of drug molecules [7]. One of the most frequent and most investigated mechanisms of cellular drug resistance relies on the active efflux of the chemotherapeutical compounds from the cells. P-glycoprotein (ABCB1/Pgp), a member of the ATP Binding Cassette (ABC) transporter family was shown to extrude numerous, structurally unrelated chemotherapeutic drugs from resistant cancer cells [8]. There is ample evidence to prove the link between the activity of Pgp and clinical anticancer drug resistance. Pgp expression is an independent prognostic factor in acute myeloid leukemia (AML) [9,10] and acute nonlymphoblastic leukemia (ANLL) [11]. Pgp function in tumor cells shows negative correlation with response to the treatment and reliably predicts therapy response in AML [12].

Recently, genetically engineered mouse models (GEMMs) have been introduced to the study of drug resistance mechanisms. GEMMs closely mimic cancer in human patients and therefore offer a unique

* Corresponding author at: P.O.B. 286, Budapest 1519, Hungary.
E-mail addresses: szakacs.gergely@ttk.mta.hu, szakacs.gergely@meduniwien.ac.at (G. Szakács).

http://dx.doi.org/10.1016/j.jconrel.2017.07.010
Received 21 March 2017; Received in revised form 6 July 2017; Accepted 7 July 2017
Available online 09 July 2017
0168-3659/

Pegylated liposomal formulation of doxorubicin overcomes drug resistance in a genetically engineered mouse model of breast cancer

Authors: András Füredi[1,2], Kornélia Szebényi[2], Szilárd Tóth[1], Mihály Cserepes[1,3], Lilla Hámori[1], Veronika Nagy[1], Edina Karai[1,4], Péter Vajdovich[4], Tímea Imre[1], Pál Szabó[1], Dávid Szüts[1], József Tóvári[3], Gergely Szakács[1, 2*]

Supplementary Materials:

Supplementary Tables

Cell line	DOX	DOX + TQ	PLD
A431	0,33	-	12,30
A431-G2	0,25	-	10,98

Supplementary Table S1. In vitro toxicity (IC50) of DOX in parental PLD A430 and ABCG2-expressing AV30-G2 cells. Values represent the average of at least three independent experiments.

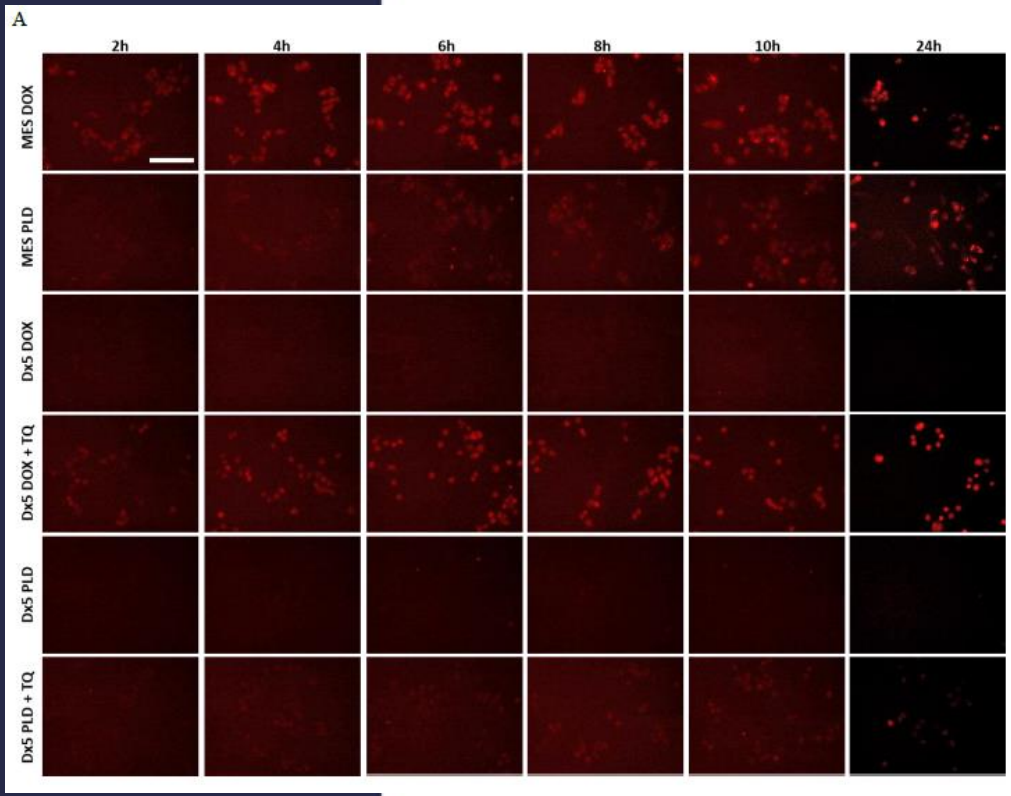

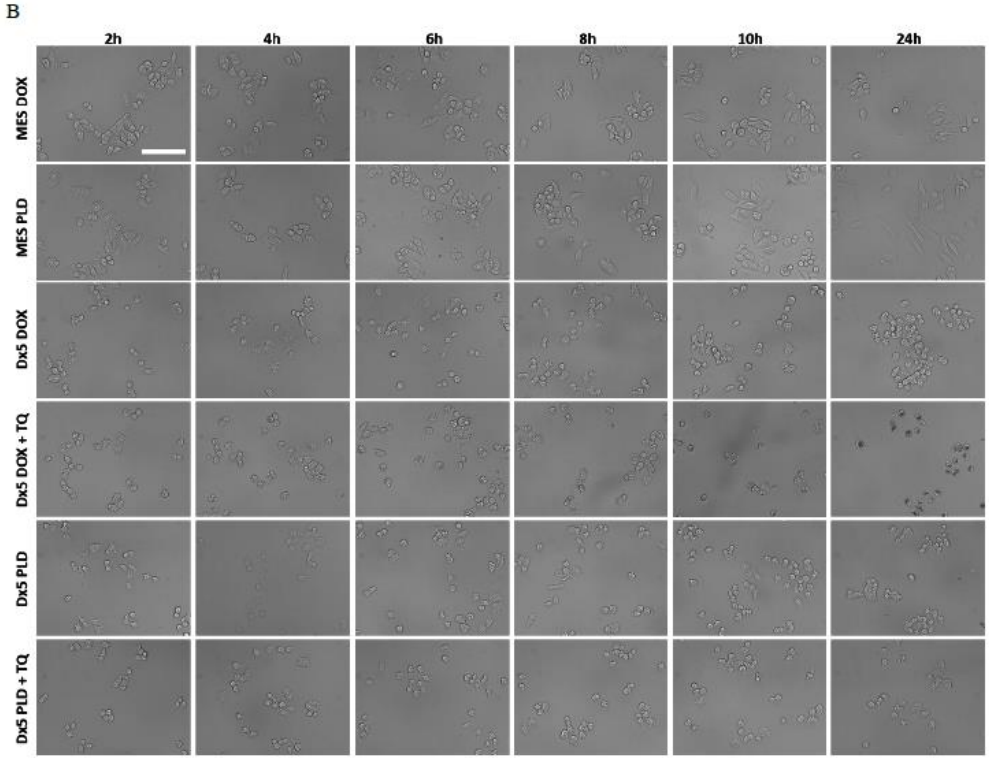

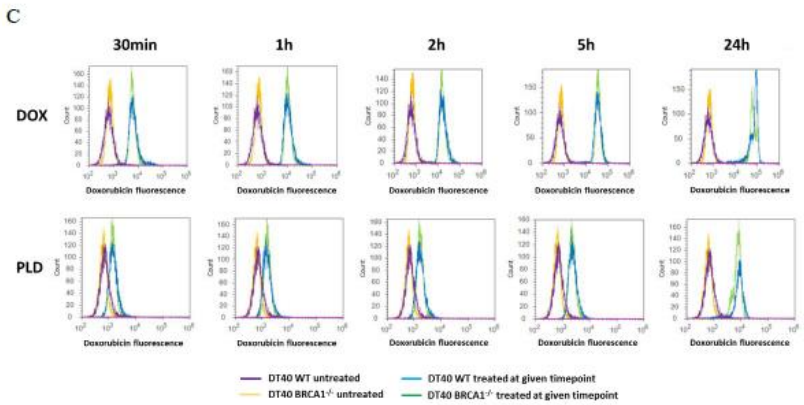

Supplementary Figure S3. In vitro studies measuring cellular fluorescence upon treatment with DOX or PLD. A. Cells seeded in 96 well plates were incubated in the presence of DOX or PLD; fluorescence was measured at the indicated time points with a JuLI Stage Real-Time Cell History Recorder (NanoEnTek). Scale bar: 100 µm. B. Bright-field image corresponding to A. C. Control and BRCA1-negative DT40 Cells were incubated with DOX or PLD at 37°C. Intercellular fluorescence was measured at the indicated time points with an Attune cytometer (Thermo).

https://doi.org/10.5607/en.2017.26.6.339
Exp Neurobiol. 2017 Dec;26(6):339-349.
pISSN 1226-2560 • eISSN 2093-8144

en
Experimental Neurobiology

Original Article

Check for updates

Osteopontin Peptide Icosamer Containing RGD and SLAYGLR Motifs Enhances the Motility and Phagocytic Activity of Microglia

Il-Doo Kim[1,2], Hahnbie Lee[1,2], Yin-Chuan Jin[3] and Ja-Kyeong Lee[1,2]*

[1]*Department of Anatomy,* [2]*Medical Research Center, Inha University School of Medicine, Incheon 22212, Korea,*
[3]*Department of Histology and Embryology, Binzhou Medical University, Yantai 264000, China*

Osteopontin (OPN) is a secreted glycoprotein that is expressed in various tissues, including brain, and mediates a wide range of cellular activities. In a previous study, the authors observed the robust neuroprotective effects of recombinant OPN and of RGD and SLAYGLR-containing OPN-peptide icosamer (OPNpt20) in an animal model of transient focal ischemia, and demonstrated anti-inflammatory and pro-angiogenic effects of OPNpt20 in the postischemic brain. In the present study, we investigated the effects of OPNpt20 on the motility and phagocytic activity of BV2 cells (a microglia cell line). F-actin polymerization and cell motility were significantly enhanced in OPNpt20-treated BV2 cells, and numbers of filopodia-like processes increased and lamellipodia-like structures enlarged and thickened. In addition, treatment of cells with either of three mutant OPN icosamers containing mutation within RGD, SLAY, or RGDSLAY showed that the RGD and SLAY motifs of OPNpt20 play critical roles in the enhancement of cell motility, and the interaction between exogenous OPNpt20 and endogenous αv and α4 integrin and the activations of FAK, Erk, and Akt signaling pathways were found to be involved in the OPNpt20-mediated induction of cell motility. Furthermore, phagocytic activity of microglia was also significantly enhanced by OPNpt20 in a RGD and SLAY dependent manner. These results indicate OPNpt20 containing RGD and SLAY motifs triggers microglial motility and phagocytic activity and OPNpt20-integrin mediated signaling plays a critical role in these activities.

Key words: osteopontin icosamer, BV2, RGD, SLAYGLR, motility, phagocytosis

INTRODUCTION

Osteopontin (OPN) is a glycoprotein expressed in macrophages/microglia and reactive astrocytes in the CNS [1, 2], and under pathological conditions, its up-regulation has been reported to have protective and anti-inflammatory effects. For example, in the subarachnoid hemorrhagic brain, recombinant OPN prevented cerebral vasospasm by inducing MAPK phosphatase (MKP)-1 (an endogenous MAPK inhibitor) and decreasing the apoptotic response [3]. OPN is also expressed in substantia nigra, and in an animal model of Parkinson's disease and its interactions with αv, β3 and β1 integrin and CD44 receptors had neuroprotective effects [4]. Protective effects of OPN have also been reported in animal models of stroke, for example, in a photothrombotic stroke model, a transient middle cerebral artery occlusion (MCAO) model, and a neonatal model of hypoxic-ischemic brain injury [5-

Received July 31, 2017, Revised November 16, 2017,
Accepted December 1, 2017

*To whom correspondence should be addressed.
TEL: 82-32-860-9893, FAX: 82-32-884-2105
e-mail: jklee@inha.ac.kr

Live cell imaging analysis

To observe cell morphologies and motilities, time-lapse images were recorded using the Juli stage (NanoEnTek Inc., Seoul, South Korea), according to the manufacturer's instructions. Mean migration distances and speeds were obtained using the Image J program.

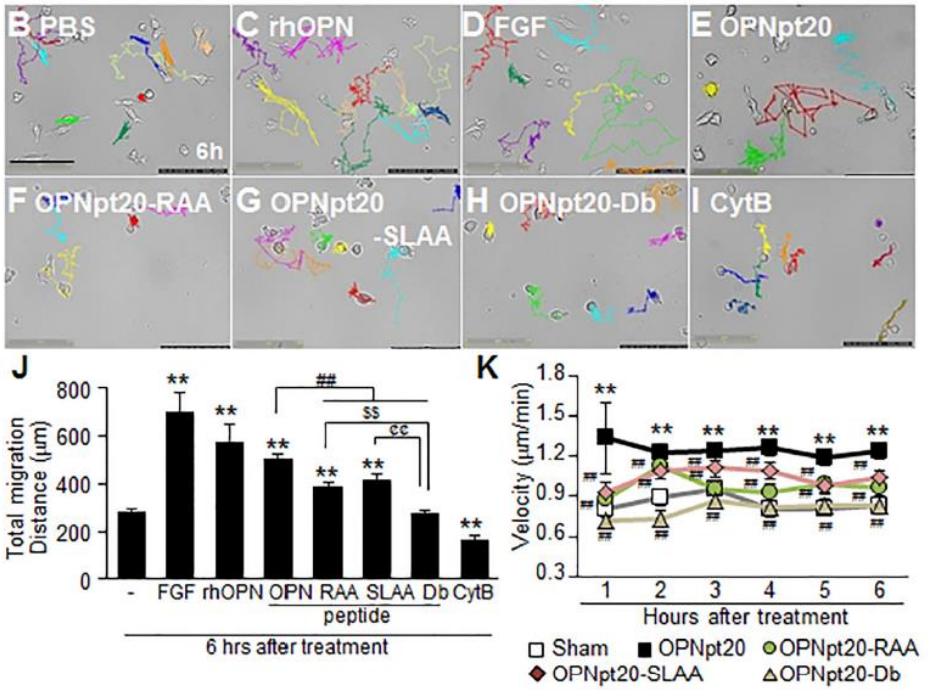

Fig. 1. Induction of microglial cell motility by OPNpt20. (A) Sequences of OPNpt20 and of the three mutant peptides. (B~I) BV2 cells were treated with FGF (C, 1 μg/ml), rhOPN (D, 1 μg/ml), OPNpt20 (E, 1 μg/ml), three mutant peptides (F~H, 1 μg/ml each), or CytB (I, 1 μg/ml) and cell motilities were monitored using a live cell imaging analyzer every 10 min for 6 hrs. Motile trajectory of each cell for 6 hrs are presented (B~I) and mean total migration distances over 6 hrs (J) and mean hourly migration speeds (K) are presented as means±SEMs (n=20). **p<0.01 versus PBS-treated controls, ##p<0.01, $$p<0.01, ^^p<0.01 between indicated groups. Scale bars represent 125 μm.

SCIENTIFIC REPORTS

OPEN

Received: 6 July 2017
Accepted: 5 December 2017
Published online: 19 December 2017

Transcriptomic analysis of mitochondrial TFAM depletion changing cell morphology and proliferation

Woo Rin Lee[1,2], Heeju Na[1], Seon Woo Lee[1], Won-Jun Lim[3,4], Namshin Kim[3,4], J. Eugene Lee[2] & Changwon Kang[1]

Human mitochondrial transcription factor A (TFAM) has been implicated in promoting tumor growth and invasion. TFAM activates mitochondrial DNA (mtDNA) transcription, and affects nuclear gene expression through mitochondrial retrograde signaling. In this study, we investigated the effects of TFAM depletion on the morphology and transcriptome of MKN45 gastric cancer cells. Morphology alteration became visible at 12 h after TFAM knockdown: the proportion of growth-arrested polygonal cells versus oval-shaped cells increased, reaching a half-maximum at 24 h and a near-maximum at 36 h. TFAM knockdown upregulated four genes and downregulated six genes by more than threefold at 24 h and similarly at 48 h. Among them, the knockdown of CFAP65 (cilia and flagella associated protein 65) or PCK1 (cytoplasmic phosphoenolpyruvate carboxykinase) rescued the effects of TFAM depletion on cell morphology and proliferation. PCK1 was found to act downstream of CFAP65 in calcium-mediated retrograde signaling. Furthermore, mtDNA depletion by 2′,3′-dideoxycytidine was sufficient for induction of *CFAP65* and *PCK1* expression and inhibition of cell proliferation, but oxidative phosphorylation blockade or mitochondrial membrane potential depolarization was not. Thus, the TFAM–mtDNA–calcium–CFAP65–PCK1 axis participates in mitochondrial retrograde signaling, affecting tumor cell differentiation and proliferation.

Human mitochondrial transcription factor A, encoded by the nuclear gene *TFAM*, plays essential roles in the transcription, replication, and packaging of circular mitochondrial genome DNA (mtDNA) into nucleoids and has critical roles in mitochondrial biogenesis. TFAM regulates mtDNA copy number by maintaining the stability of mtDNA[1], and mitochondrial biogenesis is regulated through the interaction of TFAM with mtDNA[2].

Genome-wide transcriptomic profiles of cancerous and normal tissues can provide useful information about the molecular mechanisms of cancer initiation and progression. According to the ONCOMINE database of cancer microarray assays, TFAM is upregulated in many types of cancer tissues[3]. TFAM is a key molecule in carcinogenesis, owing to its involvement in cell proliferation and invasion as well as its interference with apoptosis[4,5].

In this study, we analyzed the effects of TFAM depletion on gastric cancer MKN45 cells to gain insight into the functional role of TFAM in human cancer. Interestingly, TFAM depletion was found to decrease the rate of cell division as cells organize into polarized growth-arrested polygonal shaped colonies, which is a common phenotype observed in non-malignant cancer cells[6].

To understand the mechanism underlying this morphological shift, we first analyzed the transcriptome of TFAM-depleted MKN45 cells using next-generation RNA sequencing (RNA-Seq). Next, we assessed the functional roles of the ten most differentially expressed genes (DEGs) in promoting the phenotypic changes. In addition, we investigated how the expression of the DEGs was altered in response to mitochondrial retrograde signaling.

[1]Department of Biological Sciences, Korea Advanced Institute of Science and Technology, Daejeon, 34141, Korea. [2]Center for Bioanalysis, Korea Research Institute of Standards and Science, Daejeon, 34113, Korea. [3]Genome Editing Research Center, Korea Research Institute of Bioscience and Biotechnology, Daejeon, 34141, Korea. [4]Department of Bioinformatics, KRIBB School of Bioscience, Korea University of Science and Technology, Daejeon, 34141, Korea. Correspondence and requests for materials should be addressed to J.E.L. (email: j.eugenelee@gmail.com) or C.K. (email: ckang@kaist.ac.kr)

Cell imaging. Time-lapse photography of live cell cultures with bright-field images were taken in a humidified chamber at 37 °C and 5% CO_2 with a JuLI Stage real-time cell-history recorder (NanoEnTek, Seoul, Korea). Three-color confocal fluorescence microscopy for green, blue, and red was performed using an LSM 780 confocal laser scanning microscope (Carl Zeiss, Oberkochen, Germany).

Quantification of cell morphology changes. Image-Pro Plus software (Media Cybernetics, Silver Springs, MD) was used to count cells from the time-lapse images that were taken with the JuLI Stage and converted into 16-bit grayscale images. Total objects with select values of intensity ($\leq$24,000) and area (10–520) in the recorded images were counted as cells using the 'count and measure objects' function. Among them, cell objects with a roundness $\geq$1.3 were regarded as polygonal, and those with a roundness $<$1.3 were regarded as oval-shaped.

Quantification of cellular Ca^{2+} and ROS levels. The cellular Ca^{2+} level was assessed by 30-min incubation of 5 μM Fluo-4 AM (Thermo Fisher Scientific), a fluorogenic marker for Ca^{2+} in live cells. After incubation and washing, fluorescence was analyzed using a JuLI Stage, with excitation at 494 nm and emission at 506 nm. The cellular ROS level was assessed after 30-min incubation of 25 μM ROSstar™ 650 (LI-COR Biosciences, Lincoln, NE), a hydrocyanine probe for ROS. After incubation, cells were washed with phosphate-buffered saline buffer, and fluorescence was analyzed with a JuLI Stage, with excitation at 638 nm and emission at 656 nm. Fluorescence signals were quantified using Image-Pro® Plus software (Media Cybernetics, Silver Springs, MD) and were expressed as the mean fluorescence intensity per cell.

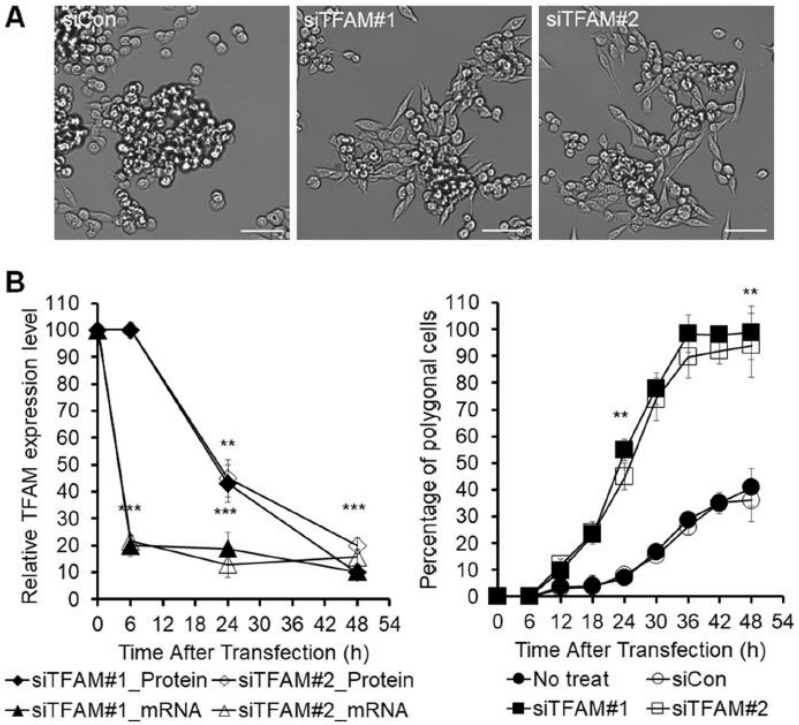

Figure 2. Screening of DEGs related to the TFAM knockdown effects on the morphology of MKN45 cells. (**A**) Representative bright-field images of morphological changes in TFAM-knockdown MKN45. The scale bar represents 50 μm. (**B**) RNA-Seq samples were prepared at 0, 6, 24, and 48 h after transfection. Left panel: time-course analysis of the TFAM mRNA and protein levels. In qPCR, relative mRNA levels were normalized to GAPDH. Relative protein levels were normalized to α-tubulin. Right panel: quantification of polygonal cells of siRNA-transfected and control MKN45 ($n = 3$, mean ± SD). Among the total cells counted with Image-Pro Plus, polygonal cells were distinguished from oval cells using the values of area and roundness. Student's t-test, $^{**}P < 0.01$, $^{***}P < 0.001$.

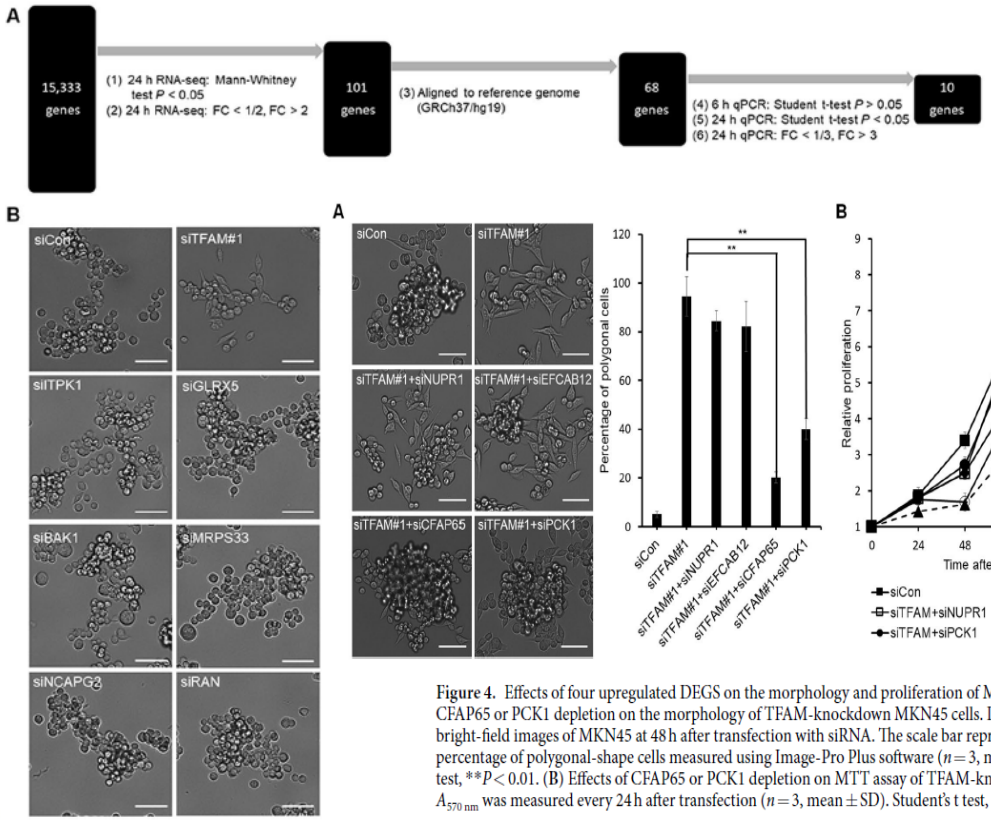

Figure 3. Effects of six downregulated DEGs on the morphology and proliferation of MKN45 cells. (**A**) Scheme of selecting DEGs of TFAM depletion using statistical filtration. From a total of 15,333 genes analyzed in Cuffdiff2, 68 genes were finally selected for quantification with qPCR for the identification of top 10 DEGs. (**B**) Effects of UBLCP1, KRT80, AP1AR, ANKRD13A, LRG1, or TMEM30B depletion on the morphology of MKN45. Left panel: representative bright-field images of MKN45 at 48 h after transfection. The scale bar represents 50 μm. Right panel: percentage of polygonal cells measured using Image-Pro Plus software. (**C**) MTT assay of UBLCP1-, KRT80-, AP1AR-, ANKRD13A-, LRG1-, or TMEM30B-depleted MKN45 cells. $A_{570\,nm}$ was measured after transfection ($n = 3$, mean ± SD). Student's t-test, $^{*}P < 0.05$, $^{**}P < 0.01$, $^{***}P < 0.001$.

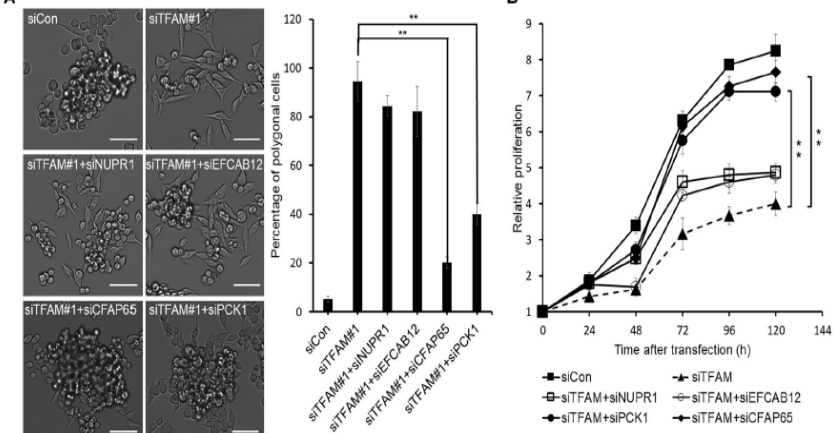

Figure 4. Effects of four upregulated DEGS on the morphology and proliferation of MKN45 cells. (**A**) Effects of CFAP65 or PCK1 depletion on the morphology of TFAM-knockdown MKN45 cells. Left panel: representative bright-field images of MKN45 at 48 h after transfection with siRNA. The scale bar represents 50 μm. Right panel: percentage of polygonal-shape cells measured using Image-Pro Plus software ($n = 3$, mean ± SD). Student's t test, $^{**}P < 0.01$. (**B**) Effects of CFAP65 or PCK1 depletion on MTT assay of TFAM-knockdown MKN45 cells. $A_{570\,nm}$ was measured every 24 h after transfection ($n = 3$, mean ± SD). Student's t test, $^{**}P < 0.01$.

Molecular and Cellular Neuroscience 83 (2017) 103–112

Contents lists available at ScienceDirect

Molecular and Cellular Neuroscience

journal homepage: www.elsevier.com/locate/ymcne

Transcriptional profiles for distinct aggregation states of mutant Huntingtin exon 1 protein unmask new Huntington's disease pathways

Nagaraj S. Moily[a], Angelique R. Ormsby[a], Aleksandar Stojilovic[a], Yasmin M. Ramdzan[a], Jeannine Diesch[b,c], Ross D. Hannan[b,d], Michelle S. Zajac[e,f], Anthony J. Hannan[e,f], Alicia Oshlack[g,*], Danny M. Hatters[a,*]

[a] Department of Biochemistry and Molecular Biology, Bio21 Molecular Science and Biotechnology Institute, The University of Melbourne, VIC 3010, Australia
[b] Research Division, Peter MacCallum Cancer Centre, 305 Grattan Street, Melbourne, VIC 3000, Australia
[c] Josep Carreras Leukaemia Research Institute, ICO-Hospital Germans Trias i Pujol, Badalona, Spain
[d] The John Curtin School of Medical Research, Australian National University, Acton, ACT, Australia
[e] Florey Institute of Neuroscience and Mental Health, Melbourne Brain Centre, University of Melbourne, Parkville, VIC, Australia
[f] Department of Anatomy and Neuroscience, University of Melbourne, Parkville, VIC, Australia
[g] Murdoch Childrens Research Institute, Royal Children's Hospital, Flemington Road, Parkville, Victoria 3052, Australia

ARTICLE INFO

Keywords:
Protein misfolding
Amyloid
Neurodegenerative disease
Huntington's disease

ABSTRACT

Huntington's disease is caused by polyglutamine (polyQ)-expansion mutations in the CAG tandem repeat of the *Huntingtin* gene. The central feature of Huntington's disease pathology is the aggregation of mutant Huntingtin (Htt) protein into micrometer-sized inclusion bodies. Soluble mutant Htt states are most proteotoxic and trigger an enhanced risk of death whereas inclusions confer different changes to cellular health, and may even provide adaptive responses to stress. Yet the molecular mechanisms underpinning these changes remain unclear. Using the flow cytometry method of pulse-shape analysis (PulSA) to sort neuroblastoma (Neuro2a) cells enriched with mutant or wild-type Htt into different aggregation states, we clarified which transcriptional signatures were specifically attributable to cells before versus after inclusion assembly. Dampened CREB signalling was the most striking change overall and invoked specifically by soluble mutant Httex1 states. Toxicity could be rescued by stimulation of CREB signalling. Other biological processes mapped to different changes before and after aggregation included NF-kB signalling, autophagy, SUMOylation, transcription regulation by histone deacetylases and BRD4, NAD + biosynthesis, ribosome biogenesis and altered HIF-1 signalling. These findings open the path for therapeutic strategies targeting key molecular changes invoked prior to, and subsequently to, Httex1 aggregation.

1. Introduction

Protein misfolding and aggregation into amyloids underlies many of the major human neurodegenerative diseases, including Alzheimer's, Parkinson's, Huntington's and motor neuron disease (Sipe et al., 2016). In these diseases, the appearance of macroscopic intracellular protein aggregates known as inclusions form as a hallmark of disease development. Huntington's disease (HD) is one of the classic examples of the amyloid diseases involving intracellular protein aggregating into inclusions. HD involves an expansion of a CAG trinucleotide repeat sequence, encoding polyglutamine (polyQ), within exon 1 of huntingtin (Htt) beyond the disease threshold of 35 repeats (MacDonald et al., 1993). The polyQ expansion leads to a greatly enhanced capacity of the Htt exon 1 (Httex1) domain to aggregate into amyloid fibrils in vitro (Scherzinger et al., 1999) and for N-terminal fragments similar in length to Httex1 to form microscopic inclusion bodies in pathology (DiFiglia et al., 1997; Kazantsev et al., 1999). The link to disease from polyQ-expanded Httex1 has been well documented. Namely, the transgenic expression of polyQ-expanded Httex1 is sufficient to produce a HD-like pathology in rodent and primate models (Davies et al., 1997; von Horsten et al., 2003; Yang et al., 2008) and confers toxicity in cell culture models as well (Arrasate et al., 2004). As such Httex1 has been used extensively to model HD biology.

An outstanding question remains as to the role of aggregation in

Abbreviations: PolyQ, Polyglutamine; Htt, Huntingtin; Httex1, Htt Exon 1; HD, Huntington's disease; PulSA, Pulse Shape Analysis; i, Cells With Inclusions; ni, Cells With Diffuse Httex1; RFU, Relative Fluorescence Units; IPA, Ingenuity Pathway Analysis; FDR, False Discovery Rate; WT, Wild-Type; GFP, Green Fluorescent Protein; ROI, Region Of Interest

* Corresponding authors.
E-mail addresses: alicia.oshlack@mcri.edu.au (A. Oshlack), dhatters@unimelb.edu (D.M. Hatters).

http://dx.doi.org/10.1016/j.mcn.2017.07.004
Received 12 April 2017; Received in revised form 23 June 2017; Accepted 21 July 2017
Available online 23 July 2017
1044-7431/

2.12. Longitudinal live cell imaging

The cells were plated at a density of 1×10^5 cells/well in a 24 well plate. After 24 h, cells were co-transfected with 72Q-Httex1-mCherry, 25Q-Httex1-mCherry or mCherry alone and GFP using Lipofectamine 3000 reagent (Life Technologies). Media was refreshed 6 h after transfection. The GFP was used as a cellular tracer of death and proxy for Httex1 expression level. After 24 h cells were imaged using a JuLI stage live cell imaging system with fluorescent images acquired at 15 min intervals for 96 h (Nanoentek, Seoul, South Korea). Cells were tracked for visible aggregate formation and the time point of death (by loss of GFP fluorescence) with image processing tool Fiji (Version 2.0.0-rc-44) (Schindelin et al., 2012). Survival curves were analyzed using Prism software. Cells that drifted from focus were censored in the analysis. Expression level was calculated by measuring mean GFP levels in an ROI within the cytosol. The cells included for analysis had a mean fluorescence ± 2 standard deviation of the sample with the lowest variance. *P*-values were determined using log-rank (Mantel Cox) test. For drug treatments, forskolin (Cayman Chemical) was added after transfection to a concentration of 0.5 μM, which corresponds to the EC_{50} dosage. CREB inhibitors SGC-CBP30 (20 nM) and I-CBP112 (150 nM) were added after transfection (Sigma-Aldrich). Both drugs were added at 6 h post transfection during media refreshment.

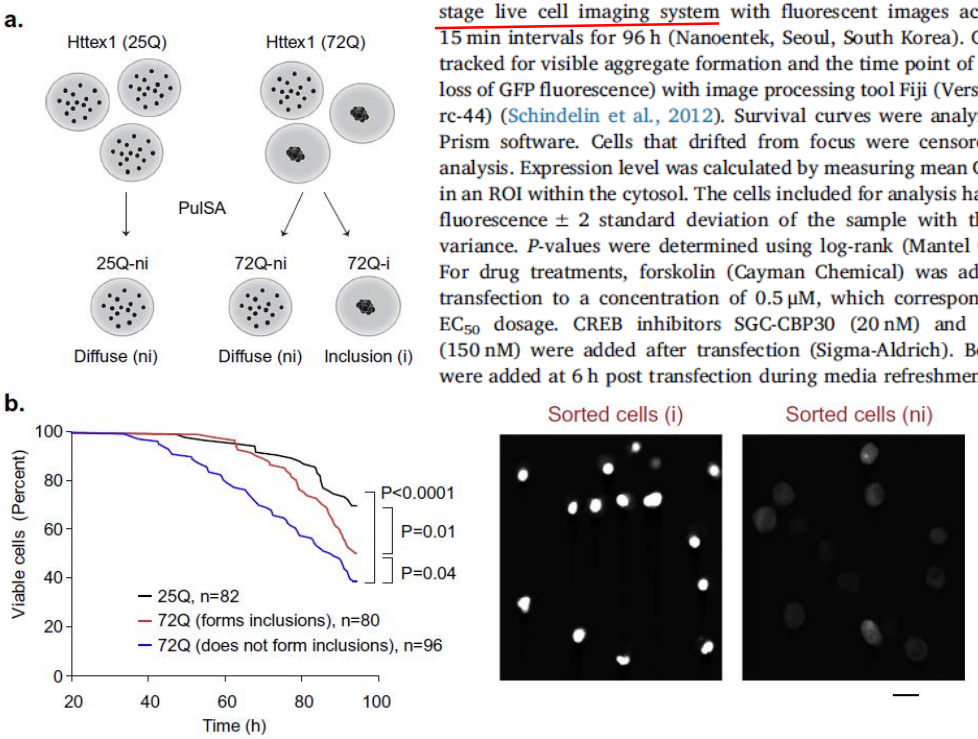

Fig. 1. Strategy to separate cells into populations enriched with polyQ-expanded Httex1 in distinct aggregation states. a) Pulse Shape Analysis (PulSA) by flow cytometry can separate cell populations heterogeneous in aggregation state. b) Neuro2a cells that form inclusions live longer than those that do not. Shown are Kaplan-Meier survival curves tracked by longitudinal imaging of Httex1-Emerald fusions from 20 h after transfection. *P*-values refer to log-rank test (Mantel Cox) on survival curves. c) Flow cytograms showing the PulSA gating strategy to sort the mixed cell populations for analysis by whole transcriptome analysis. Shown are gates for i and ni and for matched expression (red; Further details in Fig. S1). The images show representative cells collected by sorting flow cytometry and imaged for GFP fluorescence by confocal microscopy. Scale bar, 20 μm. (For interpretation of the references to colour in this figure legend, the reader is referred to the web version of this article.)

SCIENTIFIC REPORTS

OPEN

Received: 18 October 2016
Accepted: 26 October 2017
Published online: 09 November 2017

Hypoxia-induced reactive oxygen species mediate N-cadherin and SERPINE1 expression, EGFR signalling and motility in MDA-MB-468 breast cancer cells

Iman Azimi[1,2,3], Rosalie M. Petersen[1], Erik W. Thompson[3,4,5], Sarah J. Roberts-Thomson[1] & Gregory R. Monteith[1,2,3]

One of the hallmarks of the tumour microenvironment is hypoxia resulting from increased oxygen consumption by proliferative cancer cells and altered vasculature. Hypoxic tension initiates various cellular signals and can drive epithelial to mesenchymal transition (EMT), a process important in cancer progression. In this study, using the antioxidant N-acetylcysteine (NAC), we show that hypoxia-induced reactive oxygen species (ROS) in MDA-MB-468 breast cancer cells, selectively regulate hypoxia-induced increases in N-cadherin and SERPINE1, two proteins involved in cell adhesion. Treatment of cells with NAC also attenuated hypoxia-mediated activation of EGFR, but did not have any effect on hypoxia-mediated induction of HIF1α. Exogenous hydrogen peroxide phenocopied the effects of hypoxia on N-cadherin and SERPINE1 expression and EGFR activation, suggesting its possible involvement in these hypoxia-mediated events. Reflective of their effect on cell adhesion proteins and EGFR (associated with migratory phenotypes), NAC also reduced cell migration under hypoxic conditions, a crucial event in metastasis. Our findings suggest a selective role for redox signalling in the regulation of specific components of the responses to hypoxia and induction of EMT in breast cancer cells. This study provides new evidence supporting the potential of targeting ROS as a therapeutic strategy for the control of breast cancer metastasis.

Tumours rapidly exhaust the local oxygen supply creating a hypoxic environment[1]. This hypoxic microenvironment around cancer cells can promote invasion and metastasis as well as resistance to radiation therapy and anti-cancer drugs[1,2]. Cancer cells also have increased levels of reactive oxygen species (ROS) production compared to normal cells, which may contribute to tumour progression and metastasis[3–6]. ROS also play critical roles in the regulation of signal transduction pathways in a range of cellular processes and are increased by hypoxia in a number of cell types[7–9]. ROS increase in response to hypoxia occurs via the transfer of electrons from ubisemiquinone to molecular oxygen at the Q_0 site of the mitochondrial complex III[10,11].

Several groups have shown that hypoxia induces epithelial to mesenchymal transition (EMT) in breast cancer cells[12–15], a process important in tumour metastasis[16]. During EMT, cancer cells acquire features of mesenchymal-like cells including enhanced migratory and invasive abilities, changes in cellular adhesion, remodelling of the extracellular matrix, and increased resistance to stress and apoptosis[17,18]. ROS can induce EMT, however, the specificity of their action in the regulation of particular signalling pathways or EMT markers is dependent on the cellular context and type of tissue and is not fully understood[19–22]. MDA-MB-468 cells are a commonly used model in the study of EMT in triple-negative breast cancer (TNBC)[23–25], a type of breast

[1]School of Pharmacy, The University of Queensland, Brisbane, Queensland, Australia. [2]Mater Research Institute, The University of Queensland, Brisbane, Queensland, Australia. [3]Translational Research Institute, Brisbane, Queensland, Australia. [4]Institute of Health and Biomedical Innovation and School of Biomedical Sciences, Queensland University of Technology, Kelvin Grove, Queensland, Australia. [5]University of Melbourne Department of Surgery, St. Vincent's Hospital, Melbourne, Victoria, Australia. Correspondence and requests for materials should be addressed to I.A. (email: i.azimi@uq.edu.au)

Cell migration assay. Collagen matrices were prepared for the assessment of cell motility. Cell culture plates (96-well) were coated with 50 µL of a collagen mixture containing 10X PBS (8% v/v), DMEM (24% v/v), collagen type I from bovine skin (final concentration 2 mg/mL; C4243, Sigma-Aldrich), brought to physiological pH with 1 M NaOH. Collagen gels were formed by incubating plates at 37 °C, 5% CO_2 for 1 h. Cells were then seeded at a very low density (to ensure the assessment of single cell movement) of 500 cells per well on top of the collagen gel. After serum reduction (0.5% FBS) for 24 h, cells were treated with NAC (10 mM) and placed on the stage of a JuLi™ Stage Live Cell Imaging System (NanoEnTek Inc. Seoul, South Korea) housed in a hypoxia incubator. Bright field images from the centre of wells were taken every 15 min using a 4X objective. Assessment of cell motility was performed 24 h post exposure to hypoxia for a period of 12 h (between 24 h and 36 h in hypoxia). Strict criteria were implemented in the exclusion of cells for quantification of their motility. Exclusion criteria included the removal of cells that died, divided or moved in or out of the field of view during the time of assessment. After implementing these exclusion criteria, all cells within the field of view (ranging from 17 to 48 cells), were selected for assessment of their migration during the 12 h period. Cells were individually tracked using the Manual Tracking plug-in of ImageJ 1.49q software (NIH, Bethesda, MD, https://imagej.nih.gov/ij/). The position of cells in each frame taken every 15 min was recorded. Chemotaxis and Migration Tool V2.0 (Ibidi, Munich, Germany) was used for the illustration of cell movements and calculation of accumulated distance travelled by each cell.

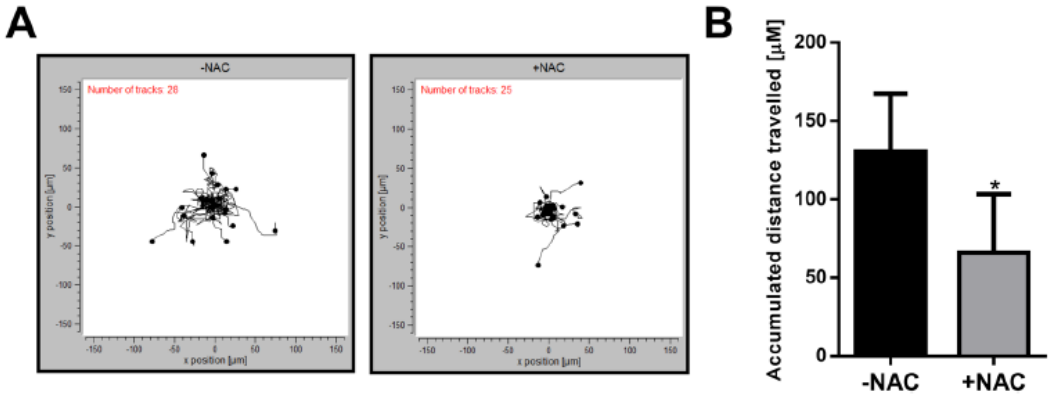

Figure 6. ROS scavenging with NAC reduces cell migration under hypoxic conditions. MDA-MB-468 cells were treated with NAC and exposed to hypoxia. Cell migration was analysed from 24 h to 36 h under hypoxic conditions. (**A**) Spatial plot of all cells from representative wells from the same experiment and (**B**) quantitative analysis of the mean accumulated distance travelled by cells from three independent experiment (duplicate wells) treated with NAC compared to the control cells without NAC treatment. *$p < 0.05$, (paired t-test).

Cold Spring Harbor Laboratory

bioRxiv
THE PREPRINT SERVER FOR BIOLOGY

New Results

Tadpole-like conformations of huntingtin exon 1 with expanded polyglutamine engenders novel interactions in cells

Estella A. Newcombe, Kiersten M. Ruff, Ashish Sethi, Angelique Ormsby, Yasmin M. Ramdzan, Archa Fox, Anthony W. Purcell, Paul R. Gooley, Rohit V. Pappu, Danny M. Hatters

doi: https://doi.org/10.1101/179663

This article is a preprint and has not been peer-reviewed [what does this mean?].

Abstract | Info/History | Metrics | Preview PDF

Abstract

Soluble huntingtin exon 1 (Httex1) with expanded polyglutamine (polyQ) engenders neurotoxicity in Huntington's disease. To uncover the physical basis of this toxicity, we performed structural studies of soluble Httex1 for wild type and mutant polyQ lengths. Nuclear magnetic resonance experiments show evidence for conformational rigidity across the polyQ region. In contrast, hydrogen-deuterium exchange shows absence of backbone amide protection, suggesting negligible persistence of hydrogen bonds. The seemingly conflicting results are explained by all-atom simulations, which show that Httex1 adopts *tadpole-like* structures with a globular head encompassing the N-terminal amphipathic and polyQ regions and the tail encompassing the C-terminal proline-rich region. The surface area of the globular domain increases monotonically with polyQ length. This stimulates sharp increases in gain-of-function interactions in cells for expanded polyQ, and one of these interactions is with the stress-granule protein Fus. Our results highlight plausible connections between Httex1 structure and routes to neurotoxicity.

Fus overexpression

Neuro2a cells were plated in 24-well format at a density of 1×10^5 cells/well. The next day, cells were transfected 4 µg plasmid DNA and 4 µL Lipofectamine 2000. Plasmids were mixed at 1:1 mass ratios of pTREX Httex1-mCherry versus pEYFP-Fus (or pTREX GFP Y66L). After 36 hours incubation, cell survival was tracked by longitudinal imaging with a JuLI-Stage live cell imager (NanoEntek, Seoul Korea) with images acquired every 20 minutes for a further 55 hours using the YFP and RFP filter channels as described (13). Cells were categorized into those that formed inclusions (at some point during the timecourse) and those that did not, and their respective survival rates were compared using the Log-rank (Mantel-Cox) test. Cells that undergo division and cells with expression levels that are outside two deviations of the population mean were excluded from the analyses.

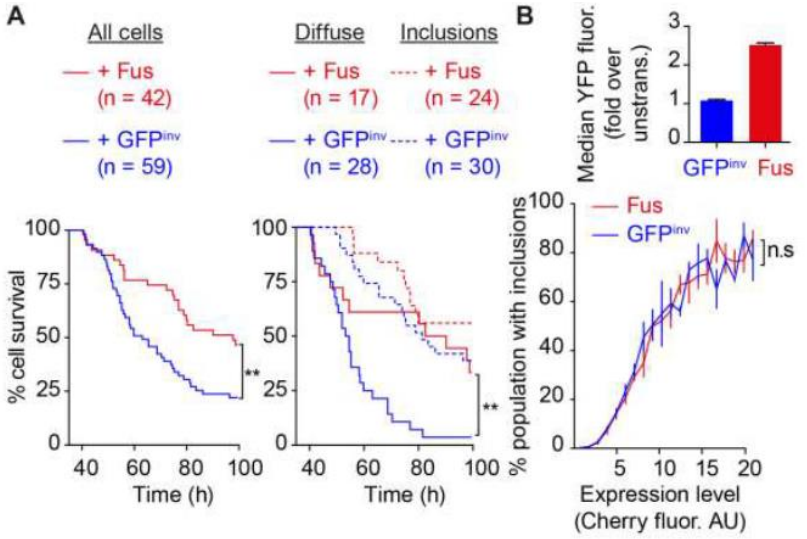

Figure 5. Fus suppresses toxicity mediated by soluble Httex1 but does not alter aggregation of Httex1. (**A**) Survival curves of Neuro2a cells co-transfected with Httex1 (46Q)-EmGFP and YFP-Fus or a non-fluorescent but folded GFP derivative GFP^{inv} (Y66L GFP mutant). Shown are Kaplan Meier curves for all cells (left) and for cells categorized into those that form inclusions and those that don't (right). Mantel-Cox Log Rank test results are indicated by **, $p<0.01$. (**B**) Flow cytometry analysis for effect of YFP-Fus overexpression on inclusion formation by Httex1(46Q)-mCherry in neuro2a cells using pulse shape analysis (83). Shown is a plot of expression levels of Fus versus control (upper graph). Shown are percentages of cells that have inclusions as a function of Httex1 levels (lower graph; n=3, mean ± SD shown).

© 2017. Published by The Company of Biologists Ltd | Disease Models & Mechanisms (2017) 10, 409-423 doi:10.1242/dmm.028175

RESEARCH ARTICLE

Heterozygous *Vangl2*^{Looptail} mice reveal novel roles for the planar cell polarity pathway in adult lung homeostasis and repair

Thanushiyan Poobalasingam[1,*], Laura L. Yates[1], Simone A. Walker[1], Miguel Pereira[2], Nina Y. Gross[1], Akmol Ali[1], Maria Kolatsi-Joannou[3], Marjo-Riitta Jarvelin[4,5,6,7], Juha Pekkanen[8,9], Eugenia Papakrivopoulou[3], David A. Long[3], Mark Griffiths[1,10], Darcy Wagner[11], Melanie Königshoff[11], Matthew Hind[1,10,12], Cosetta Minelli[2], Clare M. Lloyd[1] and Charlotte H. Dean[1,13,‡]

ABSTRACT

Lung diseases impose a huge economic and health burden worldwide. A key aspect of several adult lung diseases, such as idiopathic pulmonary fibrosis (IPF) and chronic obstructive pulmonary disease (COPD), including emphysema, is aberrant tissue repair, which leads to an accumulation of damage and impaired respiratory function. Currently, there are few effective treatments available for these diseases and their incidence is rising. The planar cell polarity (PCP) pathway is critical for the embryonic development of many organs, including kidney and lung. We have previously shown that perturbation of the PCP pathway impairs tissue morphogenesis, which disrupts the number and shape of epithelial tubes formed within these organs during embryogenesis. However, very little is known about the role of the PCP pathway beyond birth, partly because of the perinatal lethality of many PCP mouse mutant lines. Here, we investigate heterozygous *Looptail* (*Lp*) mice, in which a single copy of the core PCP gene, *Vangl2*, is disrupted. We show that these mice are viable but display severe airspace enlargement and impaired adult lung function. Underlying these defects, we find that *Vangl2*$^{Lp/+}$ lungs exhibit altered distribution of actin microfilaments and abnormal regulation of the actin-modifying protein cofilin. In addition, we show that *Vangl2*$^{Lp/+}$ lungs exhibit many of the hallmarks of tissue damage, including an altered macrophage population, abnormal elastin deposition and elevated levels of the elastin-modifying enzyme, *Mmp12*, all of which are observed in emphysema. *In vitro*, disruption of *VANGL2* impairs directed cell migration and reduces the rate of repair following scratch wounding of human alveolar epithelial cells. Moreover, using population data from a birth cohort of young adults, all aged 31, we found evidence of an interactive effect between *VANGL2* and smoking on lung function. Finally, we show that PCP genes *VANGL2* and *SCRIB* are significantly downregulated in lung tissue from patients with emphysema. Our data reveal an important novel role for the PCP pathway in adult lung homeostasis and repair and shed new light on the genetic factors which may modify destructive lung diseases such as emphysema.

KEY WORDS: Vangl2, Planar cell polarity, Lung disease, Lung homeostasis, Tissue repair, Cytoskeleton

INTRODUCTION

Globally, the burden of lung disease is enormous. For example, chronic obstructive pulmonary disease (COPD), which includes emphysema, is predicted to become the third leading cause of death worldwide by 2020 (López-Campos et al., 2016) and idiopathic pulmonary fibrosis (IPF) has a conservative incidence of 3-9 per 100,000 per year (Hutchinson et al., 2015). A key aspect of several adult lung diseases, including COPD, IPF and acute lung injury (ALI), is aberrant tissue repair, which culminates in declining lung function, tissue damage, and frequently, respiratory failure (Chilosi et al., 2013; Murray, 2012). Despite the substantial burden of degenerative lung diseases, there are currently no effective treatments available to modify repair and regeneration of damaged tissue. It has recently become apparent that adult mammalian lungs have an innate capacity for repair (Uhl et al., 2015; Butler et al., 2012). Therefore, identification of signalling pathways employed during development that are also capable of contributing to tissue repair, may lead to novel regenerative/repair approaches to treat lung disease (Kotton and Morrisey, 2014).

Lung development consists of several distinct phases; initially, the network of airways is generated via branching morphogenesis. Subsequently, the gas-exchanging region forms from the distal ends of small airways by thinning of interstitial tissue and widening of airspaces followed by formation of saccules that mature into alveoli (Herriges and Morrisey, 2014). The actin cytoskeleton has a critical role in morphogenesis by mediating organ shape and coordinated cell behaviours, including collective cell migration. Recently, the planar cell polarity (PCP) pathway has emerged as a critical regulator of tissue morphogenesis during embryonic development by directing actin cytoskeleton dynamics (Yates et al., 2010b; Munoz-Soriano et al., 2012; Wallingford, 2012). The PCP pathway

[1]Inflammation Repair and Development Section, National Heart and Lung Institute, Imperial College London, London SW7 2AZ, UK. [2]Respiratory Epidemiology, Occupational Medicine and Public Health, National Heart and Lung Institute, Imperial College London, London SW3 6LR, UK. [3]Developmental Biology and Cancer Unit, UCL Institute of Child Health, London WC1N 1EH, UK. [4]Department of Epidemiology and Biostatistics, MRC–PHE Centre for Environment & Health, School of Public Health, Imperial College London, London SW7 2AZ, UK. [5]Center for Life Course Epidemiology, Faculty of Medicine, P.O. Box 5000, University of Oulu, Oulu FI-90014 Finland. [6]Biocenter Oulu, P.O. Box 5000, Aapistie 5A, University of Oulu, Oulu FI-90014, Finland. [7]Unit of Primary Care, Oulu University Hospital, Kajaanintie 50, P.O. Box 20, Oulu FI-90220, Finland. [8]National Institute for Health and Welfare, Living Environment and Health Unit, Kuopio FI-70701, Finland. [9]University of Helsinki, Department of Public Health, Helsinki FI-00014, Finland. [10]National Institute for Health Research (NIHR) Respiratory Biomedical Research Unit at the Royal Brompton & Harefield NHS Foundation Trust and Imperial College, London SW3 6NP, UK. [11]Comprehensive Pneumology Center, Helmholtz Center Munich, Ludwig Maximilians University Munich, Munich 81377, Germany. [12]Department of Respiratory Medicine, Royal Brompton and Harefield NHS Foundation Trust, London SW3 6NP, UK. [13]Mammalian Genetics Unit, MRC Harwell Institute, Didcot OX11 0RD, UK.
*Present address: Centre for Developmental Neurobiology, New Hunt's House, Guy's Campus, King's College London, London SE1 1UL, UK.

‡Author for correspondence (c.dean@imperial.ac.uk)

C.H.D., 0000-0002-8846-5472

Received 6 October 2016; Accepted 16 February 2017

Scratch assay

Human alveolar adenocarcinoma A594 cells (obtained from ATCC, 2015) were seeded at 50,000 cells/well in eight-well chamber slides (Thermo Scientific), and cultured for 72 h in Dulbecco's minimum essential medium (DMEM) supplemented with 10% foetal bovine serum (FBS) and penicillin and streptomycin (Life Technologies). For VANGL2-knockdown studies, cells were cultured with either VANGL2 (GTC CGA ACG CCG TGC CTT GTA GC), or control (CCT CTT ACC TCA GTT ACA ATT TAT A) antisense morpholino (MO) (GeneTools, Philomath, OR) at a final concentration of 10 µM. After 72 h of MO treatment, a single scratch was made through the centre of each well using a p1000 pipette tip. For VANGL2-knockdown studies A549s were then cultured for a further 24 h in culture medium supplemented with 10 µM of the appropriate MO. For WNT5A stimulation studies, A549 cells were cultured with DMEM supplemented with 0.5% FBS, penicillin and streptomycin, and 1 µg/ml recombinant WNT5A (R&D Systems) for a further 18 h. Wells were imaged using a Zeiss Axiovert 200 microscope at t=0 and t=24 h for VANGL2 knockdown, and at t=0 and t=18 h for WNT5A stimulation study. The area of the wound healed was calculated by drawing around the outline of the scratch using the freehand tool in Fiji and subtracting the area at t=24 or t=18 from the area at t=0 h.

For siRNA experiments, A549 cells were treated with 5 nM ON-TARGETplus SMARTpool VANGL2 siRNA (Dharmacon) or ON-TARGETplus Non-targeting Pool for 72 h for knockdown. Cells were then scratched using p200 tips and cultured for 18 h. Wells were imaged using JuLi Stage real-time cell recorder (NanoEnTek Inc.) at t=0 and t=18 h.

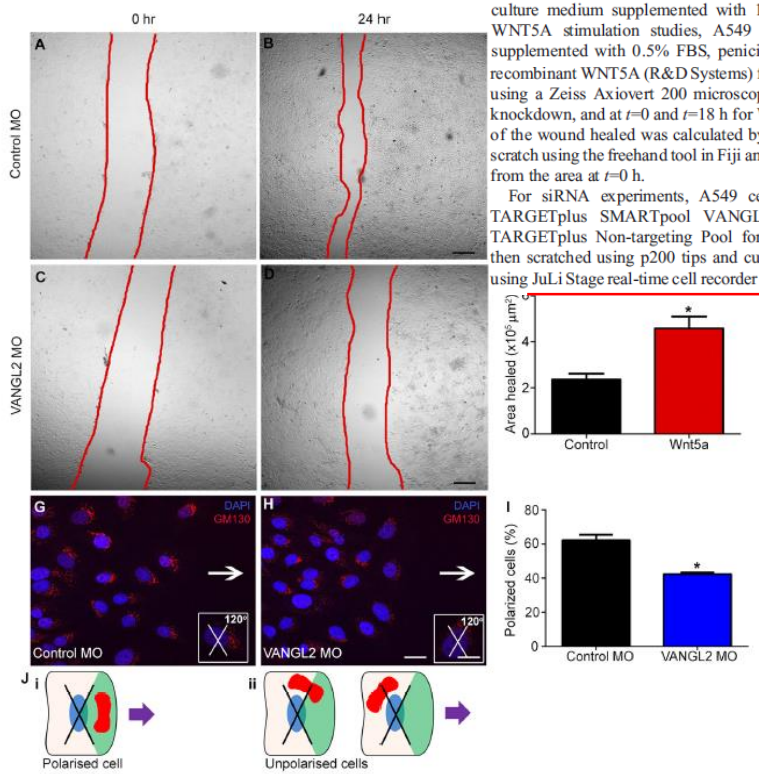

Fig. 5. VANGL2 knockdown in A549 cells leads to impaired wound healing. (A-D) Representative images showing wound edges (red lines), in A549 cells treated with (A,B) control or (C,D) anti-VANGL2 morpholino oligonucleotide (MO), (A,C) 0 h and (B,D) 24 h post scratch. (E) VANGL2 knockdown led to a 30% reduction in the area healed at 24 h compared with controls (mean±s.e.m., n=5 per treatment, with at least three technical repeats for each condition per experiment; Student's t-test, *P<0.05). (F) A549 cells stimulated for 18 h with WNT5A showed a 94% increase in the rate of wound healing compared with controls following scratch injury (n=3 per treatment, with at least three technical repeats for each condition per experiment; Student's t-test, *P<0.05). (G,H) Immunofluorescence staining for the Golgi marker (GM130) to assess cell polarity during directed cell migration at the leading edge. Insets show crosses with a 120° arc facing the direction of travel (white arrow) placed on individual cell nuclei; cells with Golgi situated within that arc were classified as polarized. (I) Quantification of percentage of polarized cells showed a significant reduction following VANGL2 knockdown compared with controls (n=3 per treatment; Student's t-test, *P<0.05). (J) Schematic illustrating the position of the 120° arc on the nucleus (blue) of cells at the leading edge. Purple arrow shows the direction of migration. (i) Golgi (red) that are located within the forward-facing 120° arc (green quadrant) were classed as polarized, (ii) cells where either the whole or majority of the Golgi body lies outside the area 120° arc were classed as not polarized. Scale bars: 322 µm (A-D), 21 µm (G,H) and 11.3 µm (insets).

www.impactjournals.com/oncotarget/ Oncotarget, 2017, Vol. 8, (No. 42), pp: 71400-71417

Research Paper

Inhibition of extracellular matrix mediated TGF-β signalling suppresses endometrial cancer metastasis

Subhransu S. Sahoo[1], Min Yuan Quah[2], Sarah Nielsen[3], Joshua Atkins[4], Gough G. Au[2], Murray J. Cairns[4], Pravin Nahar[5], Janine M. Lombard[6] and Pradeep S. Tanwar[1]

[1] Gynaecology Oncology Group, School of Biomedical Sciences and Pharmacy, University of Newcastle, Callaghan, New South Wales, Australia

[2] The Picornaviral Research Unit, School of Biomedical Sciences and Pharmacy, University of Newcastle, Callaghan, New South Wales, Australia

[3] Hunter Cancer Biobank, University of Newcastle, Callaghan, New South Wales, Australia

[4] Discipline of Pharmacy and Experimental Pharmacology, School of Biomedical Sciences and Pharmacy, University of Newcastle, Callaghan, New South Wales, Australia

[5] Department of Maternity and Gynaecology, John Hunter Hospital, New Lambton Heights, New South Wales, Australia

[6] Department of Medical Oncology, Calvary Mater Newcastle, Waratah, New South Wales, Australia

Correspondence to: Pradeep S. Tanwar, email: pradeep.tanwar@newcastle.edu.au

Keywords: microenvironment, ECM, endometrial cancer, TGF-β signalling, metastasis

Received: May 05, 2017 *Accepted*: May 07, 2017 *Published*: May 22, 2017

ABSTRACT

Although aggressive invasion and distant metastases are an important cause of morbidity and mortality in patients with endometrial cancer (EC), the requisite events determining this propensity are currently unknown. Using organotypic three-dimensional culture of endometrial cancer cell lines, we demonstrated anti-correlated TGF-β signalling gene expression patterns that arise among extracellular matrix (ECM)-attached cells. TGF-β pathway seemed to be active in EC cells forming non-glandular colonies in 3D-matrix but weaker in glandular colonies. Functionally we found that out of several ECM proteins, fibronectin relatively promotes Smad phosphorylation suggesting a potential role in regulating TGF-β signalling in non-glandular colonies. Importantly, alteration of TGF-β pathway induced EMT and MET in both type of colonies through slug protein. The results exemplify a crucial role of TGF-β pathway during EC metastasis in human patients and inhibition of the pathway in a murine model impaired tumour cell invasion and metastasis depicting an attractive target for therapeutic intervention of malignant tumour progression. These findings provide key insights into the role of ECM-derived TGF-β signalling to promote endometrial cancer metastasis and offer an avenue for therapeutic targeting of microenvironment derived signals along with tumour cells.

INTRODUCTION

The extracellular matrix (ECM) is a major component of the cellular microenvironment and regulates normal tissue development and homoeostasis. Stromal-epithelial communication in early development and steroid signalling is important for normal uterine functions. ECM of female reproductive tract undergoes extensive structural remodelling for decidualization, implantation and endometrial regeneration [1]. In contrast, abnormal ECM dynamics contributes to the pathological processes such as endometriosis, infertility, cancer and metastasis. The signalling alteration in uterine stroma or ECM that regulates remodelling of the differentiated endometrium to a disease or metastatic cancerous state is currently unclear. Studies have shown the crucial role of stromal signals in controlling the proliferative potential of endometrial epithelium [2-4]. Epi-genome wide methylation analysis revealed hypermethylation of Hand2 gene in endometrial stroma significantly contributes to endometrial cancer

In vitro metastatic spread assay and time-lapse imaging

RFP-expressing endometrial cancer cell spheroids were grown by culturing 100 epithelial cells (Ishikawa RFP$^+$ or MFE-296 RFP$^+$) in hanging drop fashion [41] with 3% matrigel. After 72 hr, oncospheres were transferred to 90% confluent monolayer of GFP-expressing endometrial stromal fibroblast cells (HESC GFP$^+$). Images were obtained every 24 hr using 10x objective on JuLi^{TM} Stage Real-Time Cell History Recorder (NanoEnTek) in an incubator at 37^{0}C and humidified 5% CO_2.

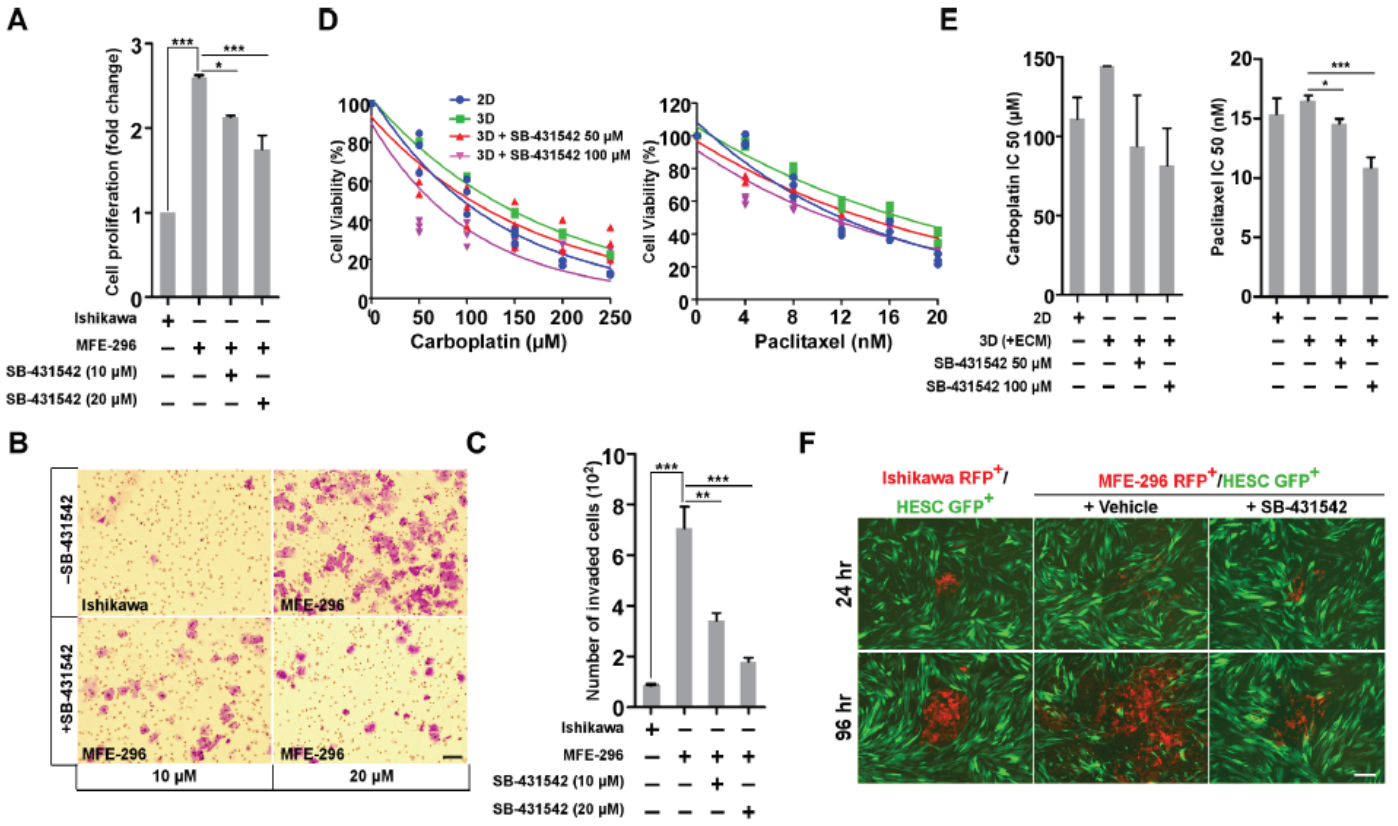

Figure 5: SB-431542 inhibits cell proliferation, invasion, chemo-resistance and metastasis *in vitro*. A. Ishikawa and MFE-296 cells were cultured in 3D matrix, treated with SB-431542 at indicated concentration and assayed for cell proliferation ($n = 3$). **B.** Ishikawa and MFE-296 cells (1 x10^5) were seeded onto the upper chamber of Transwell inserts and incubated for 24 hr with or without SB-431542 in the lower chamber to inhibit TGF-β signalling activity. Invasion of treated cells was determined by crystal violet staining. Cells in ten fields were imaged and counted to cover the entire filter in each group. **C.** Bar graphs represent the number of cells invaded in individual and treated groups ($n = 3$). **D.** Ishikawa and MFE-296 cells were cultured in monolayer and 3D (+ECM), treated with carboplatin (left) and paclitaxel (right) at indicated concentration with or without SB-431542 and were assayed for cell viability after 48 hr. **E.** IC50 values of carboplatin (left) and paclitaxel (right) were determined in different treatment groups from linear regression equation. **F.** Ishikawa RFP⁺ and MFE-296 RFP⁺ cells were grown in hanging drop 3D (+ECM) with or without SB-431542, spheroids transferred to monolayer of HESC GFP⁺ cells and time-lapse images were taken at indicated times. Scale bar, 200 μm. Error bars represent mean ± SD; $*P < 0.05$, $**P < 0.01$, $***P < 0.001$.

Journal of Molecular Neuroscience (2018) 64:262–272
https://doi.org/10.1007/s12031-017-1018-6

YAP Promotes Migration and Invasion of Human Glioma Cells

Yu Zhang[1] · Peng Xie[1,2] · Xu Wang[3] · Peng Pan[1] · Yan Wang[3] · Hao Zhang[1] · Yu Dong[1] · Yi Shi[1] · Yang Jiang[1] · Rutong Yu[3,4] · Xiuping Zhou[3,4]

Received: 4 September 2017 / Accepted: 15 December 2017 / Published online: 6 January 2018

Abstract
Previously, we have reported that Yes-associated protein (YAP) is upregulated in human glioma tissues and its level is positively correlated with patient prognosis. However, the role and mechanism of YAP in the highly invasive nature of human gliomas were largely unknown. In this study, examined by wound healing assay, transwell assay, or live-imaging, we found that YAP downregulation inhibited glioma cell migration and invasion, while YAP over-expression promoted them. Interestingly, the above effect of YAP on immortalized glioma cells was recapitulated in cultured primary glioma cells. In addition, the protein level of N-cadherin and Twist, two important proteins involved in tumor invasion, increased after YAP over-expression. Meanwhile, YAP over-expression significantly increased the F-actin level and changed the distribution of F-actin, leading to cytoskeletal reorganization, which plays an important role in cell motility. Furthermore, the promotion effect of YAP over-expression on glioma cell migration and invasion was partially abolished by Twist downregulation. Taken together, our findings show that YAP contributes to glioma cell migration and invasion by regulating N-cadherin and Twist, as well as cytoskeletal reorganization.

Keywords Glioma · YAP · Migration · F-actin · N-cadherin · Twist

Introduction

Glioblastoma (GBM) is the most common adult human primary malignant intracranial tumor (Ricard et al. 2012). Despite advances in surgery and adjuvant therapy, patients with GBM still only have a median overall survival of 12~15 months (Van Meir et al. 2010). One of the major reasons for the failure of treatments is the highly invasive nature of glioma cells (Manji et al. 2003). The highly migratory and invasive nature of glioma promotes the tumor cells' extensive invasion into the nearby normal brain tissues, leading to recurrence of the tumor (LACROIX et al. 2001). Therefore, it is urgent to explore the mechanism of glioma cell migration and invasion.

The Hippo signaling pathway, initially identified in *Drosophila*, is a highly conserved potent regulator of organ size, cell growth, and apoptosis (Dong et al. 2007; Huang et al. 2005). Yes-associated protein (YAP), the key effector of the Hippo pathway, plays an important role in organ size control by functioning as a transcription co-activator (Edgar 2006) that interacts with transcription factors, including ErbB4, P73, TEAD, P53BP-2, and Runx2 (Espanel and Sudol 2001; Howell et al. 2004; Komuro et al. 2003; SK et al. 2004; Strano et al. 2005; Strano et al. 2001; Yagi et al. 1999) and consequently orchestrating cell proliferation and death. Several reports have shown that *yap* is a candidate oncogene in the human chromosome 11q22 amplicon (Modena et al. 2006; Overholtzer et al. 2006; Zender et al. 2006), and its expression

Yu Zhang and Peng Xie contributed equally to this work.

Electronic supplementary material The online version of this article (https://doi.org/10.1007/s12031-017-1018-6) contains supplementary material, which is available to authorized users.

✉ Rutong Yu
yu.rutong@163.com

✉ Xiuping Zhou
xpzhou@xzhmu.edu.cn

[1] The Graduate School, Xuzhou Medical University, Xuzhou, Jiangsu, China

[2] Present address: Department of Neurosurgery, Huaian Second People's Hospital, Huaian 223002, China

[3] Brain Hospital, Affiliated Hospital of Xuzhou Medical University, 99 West Huai-hai Road, Xuzhou 221002, Jiangsu, People's Republic of China

[4] Institute of Nervous System Diseases, Xuzhou Medical University, 84 West Huai-hai Road, Xuzhou 221002, Jiangsu, People's Republic of China

Live-Imaging

Cells were cultured in 6 well plate on the platform of JuLI-Stage automated cell imaging system, which was put into the incubator. Images of each group with four randomly selected fields were collected as one frame per 10 min and the recording last for 24 h to make movies. The video was played at 6 fps.

OPEN

Experimental & Molecular Medicine (2018) 50, e430; doi:10.1038/emm.2017.241
Official journal of the Korean Society for Biochemistry and Molecular Biology
www.nature.com/emm

ORIGINAL ARTICLE

Proangiogenic functions of an RGD-SLAY-containing osteopontin icosamer peptide in HUVECs and in the postischemic brain

Hahnbie Lee[1,2], Yin-Chuan Jin[1,3], Seung-Woo Kim[1,2], Il-Doo Kim[1,2], Hye-Kyung Lee[1,2] and Ja-Kyeong Lee[1,2]

Osteopontin (OPN) is a phosphorylated glycoprotein secreted into body fluids by various cell types. OPN contains arginine-glycine-aspartate (RGD) and serine-leucine-alanine-tyrosine (SLAY) motifs that bind to several integrins and mediate a wide range of cellular processes. In the present study, the proangiogenic effects of a 20-amino-acid OPN peptide (OPNpt20) containing RGD and SLAY motifs were examined in human umbilical vein endothelial cells (HUVECs) and in a rat focal cerebral ischemia model. OPNpt20 exerted robust proangiogenic effects in HUVECs by promoting proliferation, migration and tube formation. These effects were significantly reduced in OPNpt20-RAA (RGD->RAA)-treated cells, but only slightly reduced in OPNpt20-SLAA (SLAY->SLAA)-treated cells. Interestingly, a mutant peptide without both motifs failed to induce these proangiogenic processes, indicating that the RGD motif is crucial and that SLAY also has a role. In OPNpt20-treated HUVEC cultures, AKT and ERK signaling pathways were activated, but activation of these pathways and tube formation were suppressed by anti-$\alpha_v\beta_3$ antibody, indicating that OPNpt20 stimulates angiogenesis via the $\alpha_v\beta_3$-integrin/AKT and ERK pathways. The proangiogenic function of OPNpt20 was further confirmed in a rat middle cerebral artery occlusion model. Total vessel length and vessel densities were markedly greater in OPNpt20-treated ischemic brains, accompanied by induction of proangiogenic markers. Together, these results demonstrate that the 20-amino-acid OPN peptide containing RGD and SLAY motifs exerts proangiogenic effects, wherein both motifs have important roles, and these effects appear to contribute to the neuroprotective effects of this peptide in the postischemic brain.
Experimental & Molecular Medicine (2018) **50**, e430; doi:10.1038/emm.2017.241; published online 19 January 2018

INTRODUCTION

Osteopontin (OPN) is a secretory phosphoprotein expressed in various tissues, including the brain, and it has been reported that OPN has important roles in various physiological processes, such as anchoring osteoclasts to the mineral bone matrix during bone resorption[1] and attaching calcium oxalate crystals to renal tubules in stone formation.[2] Elevation of OPN expression has been observed in various pathological conditions, including atherosclerosis,[3] multiple sclerosis,[4] rheumatoid arthritis[5] and most cancers,[6] which suggests that OPN has an important role in these conditions. In the normal brain, OPN expression is weak, but under pathological conditions, it is markedly upregulated in microglia and astrocytes.[7] In particular, delayed but significant induction of OPN has been reported in ischemic stroke; for example, in a rat model of transient forebrain ischemia and in a mouse model of permanent focal ischemia, OPN induction began at 12 h after injury and peaked at 5 days, respectively.[8,9]

OPN contains a highly conserved arginine-glycine-aspartic acid (RGD) motif in its N-terminal region, which interacts with $\alpha_v\beta_1$-, $\alpha_v\beta_3$- and $\alpha_v\beta_5$-integrin.[10] In addition, the SVVYGLR motif, which is adjacent to the RDG motif, is exposed by thrombin cleavage and binds to $\alpha_9\beta_1$-, $\alpha_4\beta_1$-, $\alpha_4\beta_7$- and $\alpha_4\beta_3$-integrin.[11,12] These OPN–integrin interactions mediate cell–cell and cell–matrix interactions and modulates a wide range of cellular processes, including adhesion, migration and survival,[13] and have therefore been implicated in various diseases. In addition to integrins, OPN also binds to CD44 hyaluronate receptor, a transmembrane glycoprotein known to mediate inflammatory processes, cell adhesion, and cell migration[14] via its CD44-binding domain located in the C-terminal region.[15]

In our previous study, we reported that an intranasally delivered RGD and serine-leucine-alanine-tyrosine (SLAY) motif-containing OPN icosamer peptide (20-amino-acid OPN peptide (OPNpt20)) exerted a robust neuroprotective

[1]Department of Anatomy, Inha University School of Medicine, Inchon, Republic of Korea; [2]Medical Research Center, Inha University School of Medicine, Inchon, Republic of Korea and [3]Department of Histology and Embryology, Binzhou Medical University, Yantai, China
Correspondence: Professor J-K Lee, Department of Anatomy, Inha University School of Medicine, Inharo 100 Nam-gu, Inchon 22212, Republic of Korea.
E-mail: jklee@inha.ac.kr
Received 8 December 2016; revised 5 July 2017; accepted 7 July 2017

Wound healing assay

HUVECs were seeded at 2.0×10^5/well onto gelatin-coated 12-well plates and starved for 12 h after reaching 90% confluency. Wells were then scratched longitudinally and horizontally with a yellow tip. After washing two times with M199, cultures were treated with the same medium containing 1% FBS with or without OPNpt20. Cell migration was assayed 12 h after M199 treatment using a real-time cell history recorder (JuLi Stage; NanoEnTek, Seoul, South Korea). Wound widths were measured by using the ImageJ software MRI Wound Healing Tool (National Institute of Health (NIH), Bethesda, MD, USA), and percent cell motility was calculated using the following equation: ((area at 0 h − area at 12 h)/area at 0 h) × 100.

Tube formation assay

HUVECs (5.0×10^4) were seeded on Matrigel-coated wells of a 96-well plate with or without peptides for 12 h. Tube formation was quantified by measuring tube numbers and total tube lengths in four random × 3 magnification fields per well using a real-time cell history recorder (JuLi stage; NanoEnTek, Seoul, South Korea). The data analysis was performed using the Angiogenesis Analyzer in ImageJ (NIH).

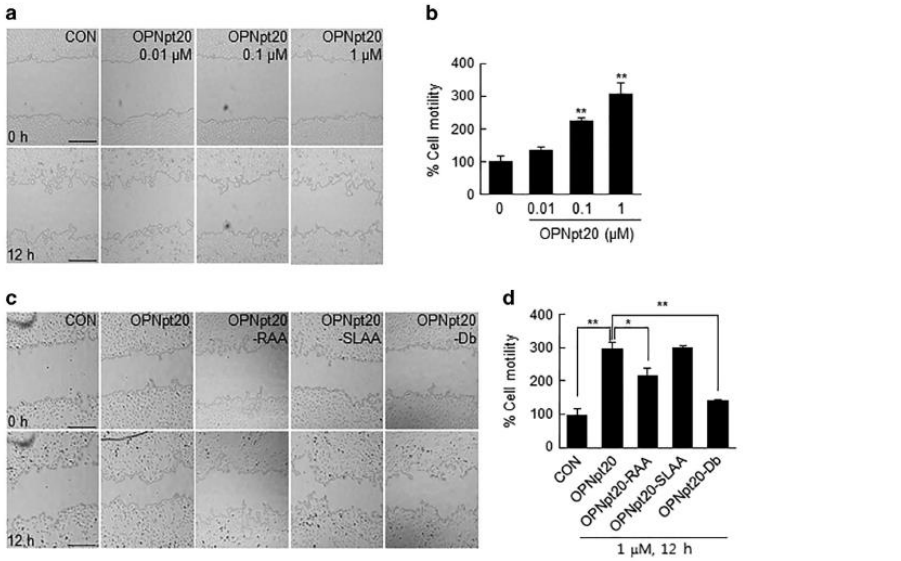

Figure 2 Induction of cell migration by 20-amino-acid OPN peptide (OPNpt20) and its mutants in human umbilical vein endothelial cell (HUVEC) cultures. (**a**, **b**) Cell migration was evaluated using a wound healing assay in HUVEC cultures after incubation with OPNpt20 (0.01, 0.1 or 1 μM) for 12 h. (**b**) Cell motility was assessed by measuring wound widths at 0 and 12 h. The results are presented as the mean ± s.e.m. ($n=4$). (**c**, **d**) HUVEC migration was measured after treatment with the three mutant peptides (1 μM) for 12 h. Representative images are presented (**a**, **c**), and results are presented as the mean ± s.e.m. ($n=3$) (**b**, **d**). Scale bars, 400 μm. $^{*}P<0.05$, $^{**}P<0.01$ between the indicated groups.

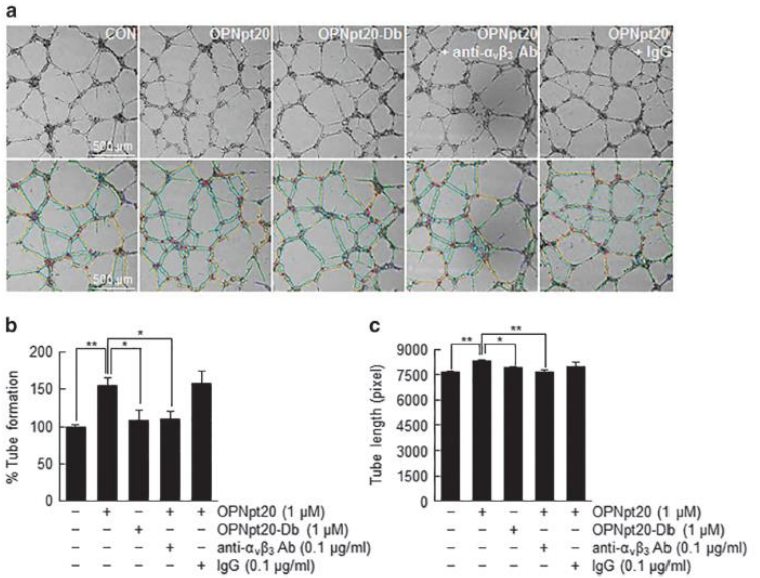

Figure 3 Induction of tube formation by 20-amino-acid OPN peptide (OPNpt20) in human umbilical vein endothelial cell (HUVEC) cultures. OPNpt20 (1 μM)-induced tube formation was examined in HUVECs treated with OPNpt20 (1 μM) or OPNpt20-Db (mutant OPN peptide with both RGD and SLAY replaced; 1 μM) for 12 h in the presence or absence of anti-$\alpha_v\beta_3$ antibody or immunoglobulin G (IgG). Representative images obtained from Image J analyzer (National Institute of Health, Bethesda, MD, USA) are presented (green, branches; yellow, master segments; blue, tubes; red, master junctions) (**a**). Tube numbers were counted (**b**), and tube lengths were measured (**c**). The results are presented as the mean ± s.e.m. ($n=3$). Scale bars, 500 μm. $^{*}P<0.05$, $^{**}P<0.01$ between the indicated groups.

nature COMMUNICATIONS

ARTICLE

DOI: 10.1038/s41467-018-02912-x OPEN

Desensitized chimeric antigen receptor T cells selectively recognize target cells with enhanced antigen expression

Chungyong Han[1], Su-Jung Sim[1], Seon-Hee Kim[1], Rohit Singh[1], Sunhee Hwang[2], Yu I. Kim[3], Sang H. Park[1], Kwang H. Kim[1], Don G. Lee[4], Ho S. Oh[2], Sangeun Lee[1], Young H. Kim[2,4], Beom K. Choi[4] & Byoung S. Kwon[2,5]

Chimeric antigen receptor (CAR) T cell therapy is an effective method for treating specific cancers. CARs are normally designed to recognize antigens, which are highly expressed on malignant cells but not on T cells. However, when T cells are engineered with CARs that recognize antigens expressed on the T cell surface, CAR T cells exhibit effector function on other T cells, which results in fratricide, or killing of neighboring T cells. Here, using human leukocyte antigen-DR (HLA-DR)-targeted CAR T cells, we show that weak affinity between CAR and HLA-DR reduces fratricide and induces sustained CAR downregulation, which consequently tunes the avidity of CAR T cells, leading to desensitization. We further demonstrate that desensitized CAR T cells selectively kill Epstein-Barr virus-transformed B cells with enhanced HLA-DR expression, while sparing normal B cells. Our study supports an avidity-tuning strategy that permits sensing of antigen levels by CAR T cells.

[1] Immunotherapeutics Branch, Division of Convergence Technology, Research Institute, National Cancer Center, Goyang 10408, Republic of Korea. [2] Eutilex Institute for Biomedical Research, Eutilex Co., Ltd., Seoul 08594, Republic of Korea. [3] Graduate School of Cancer Science and Policy, National Cancer Center, Goyang 10408, Republic of Korea. [4] Biomedicine Production Branch, Research Institute, National Cancer Center, Goyang 10408, Republic of Korea. [5] Department of Medicine, Tulane University Health Sciences Center, New Orleans, LA 70118, USA. Correspondence and requests for materials should be addressed to B.S.K. (email: bskwon@eutilex.com)

Live imaging of apoptotic cells. The kinetics of EBV LCL apoptosis were measured with a JuLI Stage real-time cell history recorder (NanoEnTek, Inc., Gyeonggi-do, Korea). Target EBV LCLs were labeled with a CellTrace violet cell proliferation kit (C34557, Thermo Fisher Scientific, Inc.). Samples of 1×10^5 T cell and EBV LCL at a T cell:EBV LCL ratio of 1:1 were incubated in 96-well flat-bottom plates in the presence of IncuCyte caspase-3/7 reagent to induce apoptosis (4440, Essen BioScience, Ann Arbor, MI, USA). DAPI- and RFP-filtered images were taken every 5 min for 90 min. Three areas of each well were analyzed. Because of the blue fluorescence of violet-labeled EBV LCLs, apoptotic EBV LCLs can be identified by observing magenta-colored cells in merged images (blue fluorescence of violet label combined with red fluorescence of apoptotic cells). The percentage of apoptotic EBV LCLs was determined and converted into a numerical value with ImageJ v1.50i software and JuLI STAT (NanoEnTek, Inc.). The proportion of apoptotic EBV LCLs was calculated from the equation: % apoptotic EBV LCLs = apoptotic EBV LCLs (magenta colored)/total EBV LCLs (blue or magenta colored).

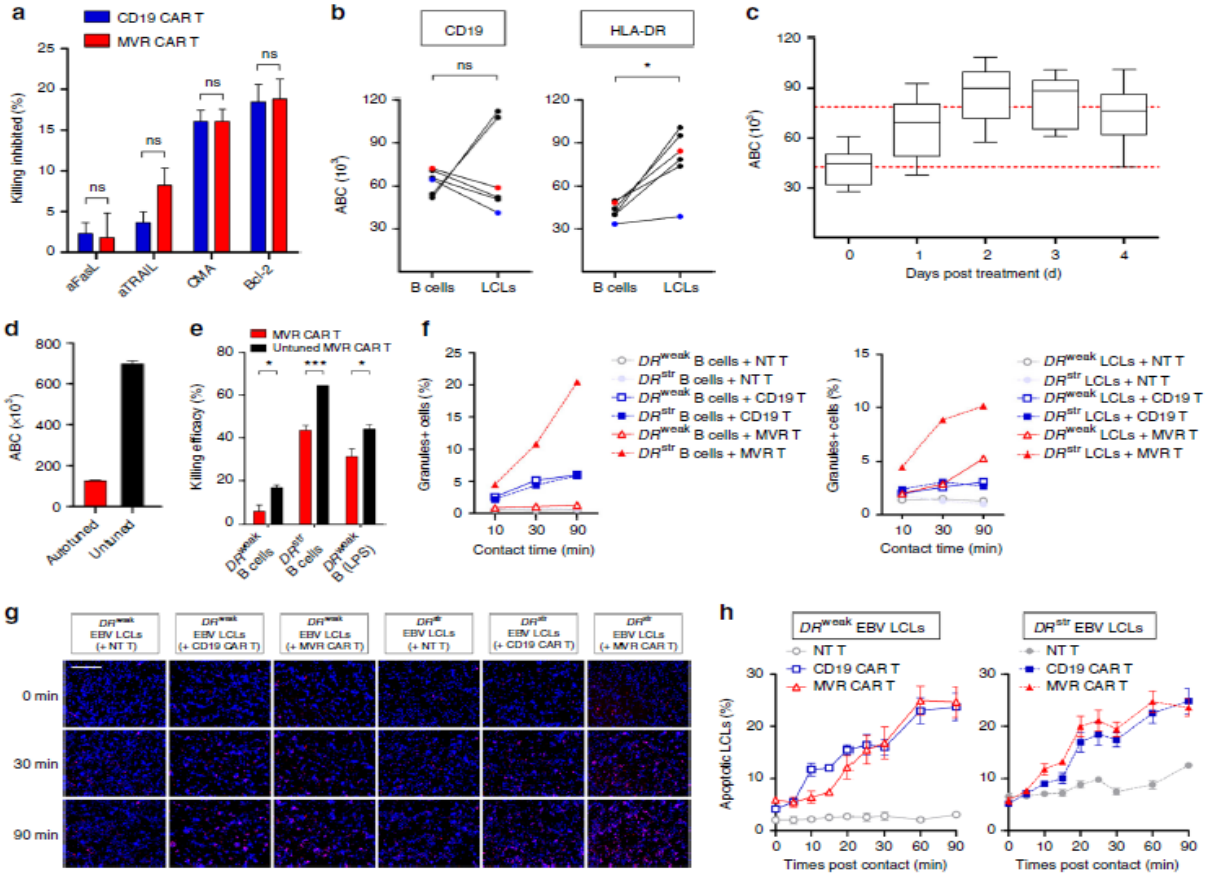

Fig. 4 MVR CAR T cells selectively kill HLA-DR-upregulated EBV LCLs by sensing antigen level. Cells from donors with different *HLA-DRB1* alleles exhibiting strong or weak binding to MVR (DR^{str} or DR^{weak}, respectively; Fig. 1a) were used as follows. **a** Killing inhibition in the presence of the indicated blocking agents. DR^{weak} EBV LCL killing by each CAR T cell type was measured as in Fig. 3f ($n = 3$). **b** Expression of CD19 and HLA-DR on B cells and EBV LCLs. Antibody binding capacity (ABC) is an index of numbers of target molecules. Dots connected by the same line involve the same donor ($n = 6$). Red and blue dots indicate DR^{weak} and DR^{str} cells, respectively. **c** HLA-DR expression on lipopolysaccharide-stimulated B cells. Cells were analyzed as in **b** for 4 days ($n = 6$). Upper and lower dotted lines indicate average HLA-DR levels of EBV LCLs and B cells, respectively, measured in **b**. Whiskers indicate minimum and maximum values. **d** MVR CAR expression on the surface of untuned and autotuned DR^{weak} MVR CAR T cells (day 2 and 12 in Fig. 2c) evaluated as in **b** ($n = 4$). **e** Killing efficacies of untuned and tuned DR^{weak} MVR CAR T cells evaluated as in Fig. 3f. DR^{weak} B cells, DR^{str} B cells, and DR^{weak} B cells treated with lipopolysaccharide for 3 days were used as target cells ($n = 3$). **f** Proportions of B cells and EBV LCLs containing transferred granules after contact with T cells. Cells contacted for indicated times were analyzed as shown in Supplementary Fig. 6. NT non-transduced. **g**, **h** Time-lapse analysis of apoptotic EBV LCLs after contact with T cells. **g** EBV LCLs (blue) undergoing apoptosis (red) identified by detecting magenta color (scale bar indicates 250 μm). **h** Proportions of apoptotic EBV LCLs at indicated time points. Three different areas of each sample were analyzed. **a** Representative of three independent experiments. **f**, **h** Representative of two independent experiments. **a**, **d**, **e** *n* indicates biological replicates. **a**, **d**, **e**, **h** Mean ± s.e.m. **b** Two-tailed Wilcoxon matched pairs test. **a**, **e** Unpaired two-tailed *t*-test; ns not significant; $^{*}p < 0.05$; $^{***}p < 0.001$

SCIENTIFIC REPORTS

OPEN

Fibroblast-associated tumour microenvironment induces vascular structure-networked tumouroid

Received: 18 September 2017
Accepted: 24 January 2018
Published online: 05 February 2018

Sang Woo Lee[1,2], Hyeong Seob Kwak[2], Myoung-Hee Kang[2], Yun-Yong Park[2,3] & Gi Seok Jeong[1,2]

In vitro **three-dimensional (3D) tumour models mimic natural cancer tissue *in vivo*, bridging the gap between conventional 2D *in vitro* testing and animal models. Stromal and cancer tissues with extracellular matrix (ECM) can provide a tumour microenvironment (TME) with cell-to-cell and cell-to-ECM interactions. These interactions induce the exchange of biophysical factors, contributing to the progression, metastasis, and drug resistance of cancer. Here, we describe a 3D *in vitro* lung cancer model cultured in a microfluidic channel that is able to confirm the role and function of various stromal cells in tumourigenesis, thereby representing an *in vivo*-like TME. We founded that biophysical factors contribute to the role of fibroblast cells in tumour formation, especially, producing a nascent vessel-like tubular structure, resulting in the formation of vascularized tumour tissue. Fibroblast cells altered the gene expression of the cancer cells to enhance metastasis, survival, and angiogenesis. The device could be used for developing and screening anti-cancer drugs through the formation of the same multicellular tumour spheroids under TME interactions. We believe this microfluidic system provides interaction of TME for cancer research by culturing stromal tissue.**

In vitro three-dimensional (3D) tumour models mimic *in vivo* natural cancer tissue. *In vitro* models of cancer have played important roles in research, ranging from their use in basic cancer research to their use in anti-cancer drug discovery[1]. For decades, conventional two-dimensional (2D) culturing platforms have been used in anti-cancer drug development, drug screening, cancer therapies, and other cancer research[2]. Although 2D systems are still actively used for such purposes, in monolayer culture, these systems lack the complex 3D cell-to-cell and cell-to-extracellular matrix (ECM) networks of cancer, which limits their usefulness and can lead to misleading or unexpected results[3]. The 3D tumour model is, therefore, widely considered to fill the gap between conventional 2D *in vitro* testing and animal models[4–6].

Cancer tissue that includes stromal cells and ECM can provide a tumour microenvironment (TME), *in vivo* and *in vitro*, in which cell-to-cell and cell-to-ECM interactions occur[2]. Through these interactions, cancer and stromal tissue induce the exchange of various biophysical and biochemical factors that contribute to the progression[7], metastasis[8], and drug resistance of cancer[1,9–13]. In particular, cancer-associated fibroblasts (CAFs) regulate the biophysical and biochemical factors of the TME that contribute to promoting the initiation and development of tumour formation[14,15]. Thus, a 3D *in vitro* tumour model with integrated ECM and stromal cells can play an important role, reflecting the *in vivo* TME[16–19].

There is much published research regarding ways to improve both *in vivo* and *in vitro* strategies for developing *in vitro* tumour models[20–23]. One approach has been the creation of 3D multicellular tumour spheroids (MCTSs) with physiological characteristics similar to tumour tissue, replicating the *in vivo* TME[24]. Although these characteristics provide an *in vivo*-like environment similar to that of natural tumour tissue, there is still a considerable need for *in vitro* studies of tumour formation and growth processes in 3D tumour tissue for a range of applications, from basic studies to the screening of potential anti-cancer agents. As a result, there is growing interest in the development of a well-organized *in vitro* tumour model in which the long-term effects of anti-cancer drugs can be assessed[3,9,25], in which the metabolic environment is similar to the natural tumour tissue environment and can be managed in real time[3], and in which close interactions between cancer and stromal tissue within the TME can be maintained[17,19,26,27].

[1]Biomedical Engineering Research Center, Asan Medical Center, Seoul, Korea. [2]Asan Institute for Life Sciences, Asan Medical Center, Seoul, Korea. [3]Department of Convergence Medicine, University of Ulsan College of Medicine, Seoul, Korea. Correspondence and requests for materials should be addressed to G.S.J. (email: gsjeong@amc.seoul.kr)

Live image capture for movie during MCTSs and vascular tube formation. The movies for tumour and vascular formation were taken using JuLI™ stage (NanoEnTek, Seoul, Korea) for the live cell imaging system. Images for the movies were captured at 30-minutes intervals for 7 days.

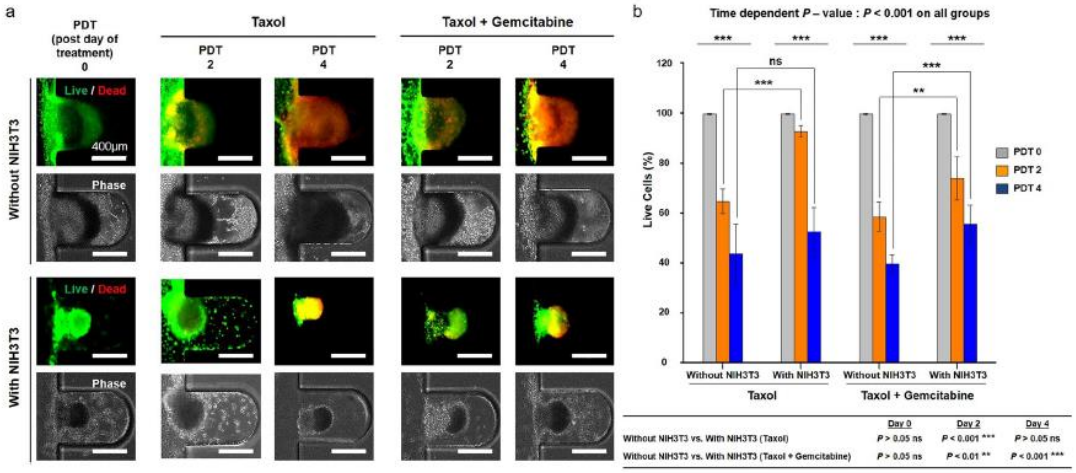

Figure 5. Screening of anti-cancer drugs on multicellular tumour spheroids (MCTSs) without and with fibroblasts. (**a**) Live and dead cells (green represents calcein-AM staining, indicating live cells, and red represents ethidium homodimer staining, indicating dead cells) after treatment of MCTSs with paclitaxel (Taxol) or a drug combination (paclitaxel + gemcitabine), administered as part of the medium flowing through the microfluidic device, without and with NIH3T3 fibroblasts. Both with- and without NIH3T3 fibroblasts, the tumour spheroid morphology remained after administration of paclitaxel or the drug combination. The proportion of live cells gradually decreased over 4 days of post-day of treatment (PDT). (**b**) After treatment with anti-cancer drugs, there was a gradual decrease in live cells in all groups, depending on the time period of drug treatment. The percentage of live cells was lower in combination treatment groups than in paclitaxel-only groups. The percentage of live cells was higher with fibroblasts than without. (**$p < 0.01$; ***$p < 0.001$).

PLOS BIOLOGY

RESEARCH ARTICLE

Olig2 and Hes regulatory dynamics during motor neuron differentiation revealed by single cell transcriptomics

Andreas Sagner[1☯], Zachary B. Gaber[2☯], Julien Delile[1☯], Jennifer H. Kong[2], David L. Rousso[2], Caroline A. Pearson[2], Steven E. Weicksel[3], Manuela Melchionda[1], S. Neda Mousavy Gharavy[1], James Briscoe[1]*, Bennett G. Novitch[2,3]*

1 The Francis Crick Institute, London, United Kingdom, 2 Department of Neurobiology, Eli and Edythe Broad Center of Regenerative Medicine and Stem Cell Research, David Geffen School of Medicine at UCLA, University of California, Los Angeles, Los Angeles, California, United States of America, 3 Department of Cell and Developmental Biology, University of Michigan Medical School, Ann Arbor, Michigan, United States of America

☯ These authors contributed equally to this work.
* james.briscoe@crick.ac.uk (JB); bnovitch@ucla.edu (BGN)

OPEN ACCESS

Citation: Sagner A, Gaber ZB, Delile J, Kong JH, Rousso DL, Pearson CA, et al. (2018) Olig2 and Hes regulatory dynamics during motor neuron differentiation revealed by single cell transcriptomics. PLoS Biol 16(2): e2003127. https://doi.org/10.1371/journal.pbio.2003127

Academic Editor: Marianne Bronner, California Institute of Technology, United States of America

Received: May 25, 2017

Accepted: January 5, 2018

Published: February 1, 2018

Data Availability Statement: Single cell RNA sequencing data are available via ArrayExpress (http://www.ebi.ac.uk/arrayexpress/experiments/E-MTAB-5466). All other relevant data has been uploaded as Supporting information files.

Funding: Wellcome Trust (grant number FC001051; WT098326MA). The funder had no role in study design, data collection and analysis, decision to publish, or preparation of the manuscript. EMBO Long-term fellowship (grant number 1438-2013). The funder had no role in

Abstract

During tissue development, multipotent progenitors differentiate into specific cell types in characteristic spatial and temporal patterns. We addressed the mechanism linking progenitor identity and differentiation rate in the neural tube, where motor neuron (MN) progenitors differentiate more rapidly than other progenitors. Using single cell transcriptomics, we defined the transcriptional changes associated with the transition of neural progenitors into MNs. Reconstruction of gene expression dynamics from these data indicate a pivotal role for the MN determinant Olig2 just prior to MN differentiation. Olig2 represses expression of the Notch signaling pathway effectors Hes1 and Hes5. Olig2 repression of Hes5 appears to be direct, via a conserved regulatory element within the Hes5 locus that restricts expression from MN progenitors. These findings reveal a tight coupling between the regulatory networks that control patterning and neuronal differentiation and demonstrate how Olig2 acts as the developmental pacemaker coordinating the spatial and temporal pattern of MN generation.

Author summary

How are the right types of cells produced in the right place, at the right time and in the correct numbers, in a developing tissue? One example of where progress has been made towards answering this question is the embryonic spinal cord. In this tissue, extracellular signals, such as the morphogen sonic hedgehog (Shh), control the pattern of generation of molecularly distinct sets of neural progenitors, from which different classes of motor neurons and interneurons are generated. Motor neurons differentiate at a much higher rate than the adjacent interneurons, and this ensures that more motor neurons than interneurons are generated and in an appropriate temporal sequence. To understand the

Single cell sequencing

NPs were dissociated using 0.05% Trypsin (Gibco) spun down in ES-medium, resuspended, washed, and spun down in 10 ml PBS (Gibco). Afterwards, cells were resuspended in 1 ml N2B27 and filtered into a FACS tube (Falcon). The Fluidigm C1 platform was used to capture individual cells using 96 small or medium IFC chips. Cells were diluted in the range of 250,000–400,000 cells per ml for chip loading. Capturing efficiency was evaluated by manually inspecting each capture site on the chip using the automated NanoEntek JuLi cell imager. Only capture sites containing single cells were processed for library preparation and sequencing. Single cell full-length cDNA was generated using the Clontech SMARTer Ultra Low RNA kit on the C1 chip using manufacturer-provided protocol. ArrayControl RNA Spikes (AM1780) were added to the cell lysis mix, as recommended in the Fluidigm protocol. Libraries were prepared using the Illumina Nextera XT DNA Sample Preparation kit, according to a protocol supplied by Fluidigm, and sequenced on Illumina Hiseq 2500 or 4000 using 50- or 75-bp paired-end runs.

Life Sciences 198 (2018) 128–135

Contents lists available at ScienceDirect

Life Sciences

journal homepage: www.elsevier.com/locate/lifescie

Assessment of the TRPM8 inhibitor AMTB in breast cancer cells and its identification as an inhibitor of voltage gated sodium channels

Kunsala T.D.S. Yapa[a], Jennifer Deuis[b], Amelia A. Peters[a,c], Paraic A. Kenny[d], Sarah J. Roberts-Thomson[a], Irina Vetter[b], Gregory R. Monteith[a,c,*]

[a] The School of Pharmacy, The University of Queensland, Brisbane, QLD, Australia
[b] Institute for Molecular Bioscience, The University of Queensland, Brisbane, QLD, Australia
[c] Mater Research, The University of Queensland, Translational Research Institute, Brisbane, QLD, Australia
[d] Kabara Cancer Research Institute, Gundersen Medical Foundation, La Crosse, WI, USA

ARTICLE INFO

Keywords:
AMTB
Breast cancer
TRPM8
Sodium channels

ABSTRACT

Aims: To assess levels of the calcium permeable transient receptor potential cation channel, subfamily melastatin, member 8 (TRPM8) in breast cancer molecular subtypes and to assess the consequences of TRPM8 pharmacological inhibition with AMTB (an inhibitor of TRPM8) on breast cancer cell lines.

Materials and methods: Cell viability and migration of breast cancer cells was determined using MTS assays and wound healing assays, respectively. RNA-Seq analysis of breast tumours and qPCR in breast cancer cell lines were used to assess mRNA levels of ion channels. Membrane potential assays were employed to assess the effects of AMTB against specific voltage gated sodium channels (Na_V).

Key findings: TRPM8 levels were significantly higher in breast cancers of the basal molecular subtype. AMTB decreased viable cell number in MDA-MB-231 and SK-BR-3 breast cancer cell lines (30 and 100 μM), and also reduced the migration of MDA-MB-231 cells (30 μM). However, these effects were independent of TRPM8, as no TRPM8 mRNA was detected in MDA-MB-231 cells. AMTB was identified as an inhibitor of Na_V isoforms. $Na_V1.1$–1.9 were expressed in a number of breast cancer cell lines, with $Na_V1.5$ mRNA highest in MDA-MB-231 cells compared to the other breast cancer cell lines assessed.

Significance: TRPM8 levels may be elevated in basal breast cancers, however, TRPM8 expression appears to be lost in many breast cancer cell lines. Some of the effects of AMTB attributed to TRPM8 may be due to effects on Na_V channels.

1. Introduction

Changes in cytosolic free calcium ($[Ca^{2+}]_{CYT}$) are often critical for events important in cancer progression [1,2]. Altered expression of specific calcium permeable ion channels has been widely reported in cancers and/or cancer cell lines originating from the lung, prostate and breast [3–7]. In some cases, such changes are even specific to the cancer clinical subtype, such as the overexpression of the transient receptor potential cation channel subfamily V member 6 (TRPV6) channel in estrogen receptor negative breast cancers and those of the basal molecular subtype [8]. The basal molecular subtype of breast cancer is of particular interest due to its overlap with breast cancers that lack the expression of receptors representing current targets for targeted therapies, such as the estrogen and human epidermal growth factor 2 (HER2) receptors [9,10].

TRPM8 is a member of the TRP ion channel family and is expressed in primary sensory neurons where it plays an important role in cold sensation [11]. The properties of TRPM8 in specific neuronal sensory pathways have seen its identification as a target for a diverse range of conditions including pain, migraine and cough [12–14]. However, despite the importance of TRPM8 as a sensor in neurons, it was actually first identified through a study assessing the overexpression of proteins in the prostate, which also demonstrated elevated levels in cancers of the prostate, lung, colon and breast [15]. Subsequent to this report, a variety of studies have explored in great depth the contribution of TRPM8 to prostate cancer cell growth and invasion and the potential role of TRPM8 modulators to control prostate cancer disease progression and/or TRPM8 as a biomarker [16–20].

Despite the first report of TRPM8 overexpression in breast cancer occurring in 2001 [15], there have been limited studies of TRPM8 in the context of possible associations with breast cancer subtypes, the role of TRPM8 in breast cancer cells and the suitability of this ion

* Corresponding author at: The School of Pharmacy and Mater Research, The University of Queensland, Brisbane, QLD, Australia.
E-mail address: gregm@uq.edu.au (G.R. Monteith).

https://doi.org/10.1016/j.lfs.2018.02.030
Received 27 November 2017; Received in revised form 11 February 2018; Accepted 23 February 2018
Available online 26 February 2018
0024-3205/

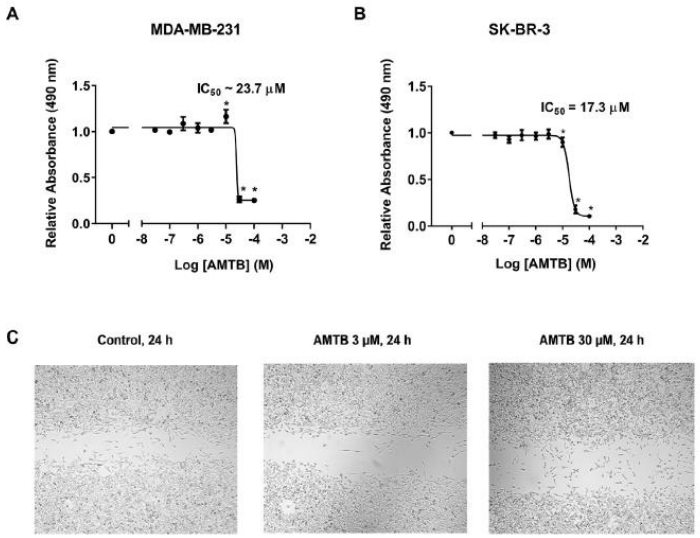

Fig. 2. AMTB reduces cell viability and migration of breast cancer cells.
Concentration-response curves for AMTB in MDA-MB-231 (A) and SK-BR-3 (B) breast cancer cells. Cells were incubated with AMTB (0–100 μM) for 72 h and an MTS assay was used to approximate viable cell number. Absorbance values (490 nm) were normalised to control treated cells and plotted using non-linear regression curve fit: log (inhibitor) vs response – variable slope (four parameters). Data show mean ± SD, $n = 3$. Statistical analysis was performed using a one-way ANOVA with Dunnett's multiple comparisons test; $^*P < 0.05$ compared to control. C: In vitro scratch assays were performed on MDA-MB-231 cells in the absence (control, 0) and presence of AMTB (3 μM, 30 μM). AMTB (30 μM) decreased the migration of MDA-MB-231 cells by ~20%. Representative images from one experiment after initial scratch (0 h) and 24 h post-treatment. Bar graph represents the relative confluency of each treatment group normalised to control well (24 h with media only); mean ± SD, $n = 3$, $^*P < 0.05$.

2.5. In vitro scratch assay

MDA-MB-231 cells (17,000 cells per well) were seeded in 96-well plates and incubated at 37 °C, 5% CO_2 for 48 h. The WoundMaker™ instrument (Essen Biosciences) was used to produce an equal sized scratch in the cell monolayer of all wells of the plate. Cells were washed twice with fresh media and immediately treated with various concentrations of AMTB for 24 h. Images of the centre of each well were acquired with a JuLI™ Stage live cell imaging system (NanoEntek) (10× objective), 24 h post-treatment. Analysis of wound closure (confluence) was performed using JuLI™ Stage automated cell imaging system software (V0.0, NanoEntek). Confluency results were normalised to a control well (media treatment) representing the highest confluence at 24 h.

Cell Calcium 72 (2018) 39–50

Contents lists available at ScienceDirect

Cell Calcium

journal homepage: www.elsevier.com/locate/ceca

Assessment of cytosolic free calcium changes during ceramide-induced cell death in MDA-MB-231 breast cancer cells expressing the calcium sensor GCaMP6m

John J. Bassett[a], Alice H.L. Bong[a], Ellen K. Janke[a], Mélanie Robitaille[a], Sarah J. Roberts-Thomson[a], Amelia A. Peters[a,b], Gregory R. Monteith[a,b,*]

[a] School of Pharmacy, The University of Queensland, Brisbane, Queensland, Australia
[b] Mater Research Institute, The University of Queensland, Translational Research Institute, Brisbane, Queensland, Australia

ARTICLE INFO

Keywords:
GCaMP6
Ceramide
Calcium signaling
Breast cancer
MDA-MB-231
Cell death

ABSTRACT

Alterations in Ca^{2+} signaling can regulate key cancer hallmarks such as proliferation, invasiveness and resistance to cell death. Changes in the regulation of intracellular Ca^{2+} and specific components of Ca^{2+} influx are a feature of several cancers and/or cancer subtypes, including the basal-like breast cancer subtype, which has a poor prognosis. The development of genetically encoded calcium indicators, such as GCaMP6, represents an opportunity to measure changes in intracellular free Ca^{2+} during processes relevant to breast cancer progression that occur over long periods (e.g. hours), such as cell death. This study describes the development of a MDA-MB-231 breast cancer cell line stably expressing GCaMP6m. The cell line retained the key features of this aggressive basal-like breast cancer cell line. Using this model, we defined alterations in relative cytosolic free Ca^{2+} ($[Ca^{2+}]_{CYT}$) when the cells were treated with C2-ceramide. Cell death was measured simultaneously *via* assessment of propidium iodide permeability. Treatment with ceramide produced delayed and heterogeneous sustained increases in $[Ca^{2+}]_{CYT}$. Where cell death occurred, $[Ca^{2+}]_{CYT}$ increases preceded cell death. The sustained increases in $[Ca^{2+}]_{CYT}$ were not related to the rapid morphological changes induced by ceramide. Silencing of the plasma membrane Ca^{2+} ATPase isoform 1 (PMCA1) was associated with an augmentation in ceramide-induced increases in $[Ca^{2+}]_{CYT}$ and also cell death. This work demonstrates the utility of GCaMP6 Ca^{2+} indicators for investigating $[Ca^{2+}]_{CYT}$ changes in breast cancer cells during events relevant to tumor progression, which occur over hours rather than minutes.

1. Introduction

Changes in intracellular Ca^{2+} dynamics are a feature of several cancers [1–3], including those of the prostate [4], colon [5] and breast [6]. Such alterations are often associated with augmentation of cancer-related processes, including cell migration, proliferation and/or evasion of cell death [7]. The remodeling of Ca^{2+} homeostasis in cancer can be driven by changes in the expression of Ca^{2+} permeable ion channels and Ca^{2+} pumps, resulting in alterations to the magnitude of relative cytosolic free Ca^{2+} ($[Ca^{2+}]_{CYT}$) increases, as well as potential changes in the spatial and temporal aspects of the Ca^{2+} signal [2,8]. For example, global $[Ca^{2+}]_{CYT}$ oscillations mediated *via* store-operated Ca^{2+} entry can promote WM793 melanoma cell invasion *via* activation of invadopodia assembly [9]. Investigating $[Ca^{2+}]_{CYT}$ changes occurring during cell death may improve our understanding of the consequence of $[Ca^{2+}]_{CYT}$ remodeling and cancer cell survival.

Measuring $[Ca^{2+}]_{CYT}$ changes during processes important in cancer that occur over hours has been difficult, due to limitations of small molecule fluorescent Ca^{2+} indicators, which have been predominantly used for the measurement of $[Ca^{2+}]_{CYT}$ in studies of breast cancer cells. These are generally unsuited to long-term (hours, days) studies, due to dye leakage and sequestration [10,11]. Recent improvements in genetically encoded Ca^{2+} indicators (see reviews [12–16]) including the GCaMP6 series [17], now provide the opportunity to reliably define changes in calcium signaling in cancer cells for cellular events that occur over hours or even days. Studies using genetically encoded Ca^{2+} sensors have provided new insights into brain physiology, as exemplified by the recent identification of distinct Ca^{2+} oscillations present during astrocyte neuronal cell death using the membrane targeted Lck-GCaMP6 sensor [18]. The application of GCaMP6 sensors to cancer cells coupled with recent advances in automated epifluorescence microscopy (automated liquid addition, improvements in cell tracking,

* Corresponding author at: School of Pharmacy, The University of Queensland, 20 Cornwall Street, Woolloongabba, 4102, Brisbane, Queensland, Australia.
E-mail address: gregm@uq.edu.au (G.R. Monteith).

https://doi.org/10.1016/j.ceca.2018.02.003
Received 24 November 2017; Received in revised form 12 February 2018; Accepted 19 February 2018
Available online 02 March 2018
0143-4160/

2.6. Brightfield imaging

Brightfield imaging was performed using a JuLI Stage Real-Time Cell History Recorder (NanoEntek), placed in a humidified incubator maintained at 37 °C and 5% CO_2. Cells were seeded at 5×10^3 cells/well in 96-well plates for morphological assessment of ceramide-induced cell death. After 24 h, following an initial pre-treatment image, cells were treated with 100 µM ceramide and returned to the JuLI Stage where images were captured every 5 min for 48 h using a 20X objective. For migration assessment, MDA-MB-231 or GCaMP6m-MDA-MB-231 cells were seeded at 2×10^4 cells/well in 96-well plates and 24 h later the cell monolayer was scratched uniformly using a WoundMaker™ scratch device (Essen Biosciences). Cells were then washed twice with media and 100 µL of fresh media was added. Wound closure was imaged every 5 min for 24 h using a 4X objective. Gap closure was determined using MRI Wound Healing Tool macro for ImageJ software (version 1.49). Proliferation rates of MDA-MB-231 cells and GCaMP6m-MDA-MB-231 cells were investigated by seeding cells at 4×10^3 cells/well in 96-well plates and after 24 h assessing cell confluence using brightfield imaging every 6 h for 72 h. Cell area measurements were performed using ImageJ software (version 1.49).

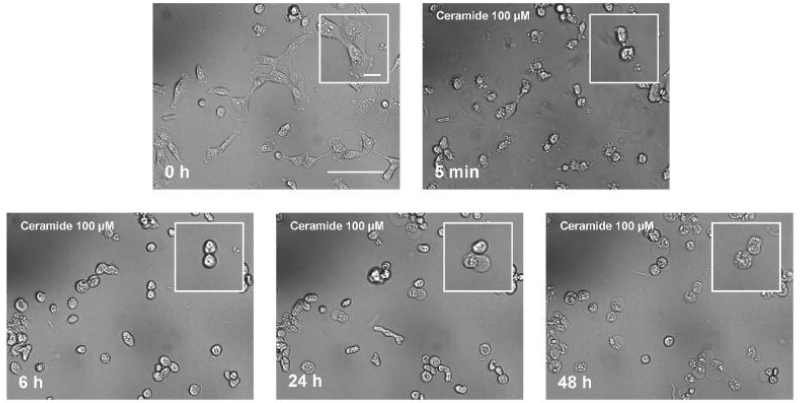

Fig. 3. Brightfield imaging of morphology changes and cell death in ceramide treated GCaMP6m-MDA-MB-231 cells.
Following a baseline image (0 h), ceramide 100 µM was added to cells and imaged every 5 min for 48 h. Representative images at t = 0, 5 min, 6 h, 24 h and 48 h (scale bar = 100 µm), with inset highlighting example cell morphology changes (scale bar = 20 µm).

SCIENTIFIC REPORTS

OPEN

MicroRNA-21 in cancer-associated fibroblasts supports lung adenocarcinoma progression

Received: 15 March 2018
Accepted: 30 May 2018
Published online: 11 June 2018

Akiko Kunita[1], Shigeki Morita[1], Tomoko U. Irisa[1], Akiteru Goto[2], Toshiro Niki[3], Daiya Takai[4], Jun Nakajima[5] & Masashi Fukayama[1]

Cancer-associated fibroblasts (CAFs) interact closely with cancer cells, supporting their growth and invasion. To investigate the role of microRNA-21 (miR-21) in lung adenocarcinoma, and especially in its CAF component, *in situ* hybridisation was applied to samples from 89 invasive lung adenocarcinoma cases. MiR-21 expression was observed in both cancer cells and CAFs. When the patients were stratified by expression, miR-21 levels in CAFs (n = 9), but not in cancer cells (n = 21), were inversely correlated with patient survival; patients with miR-21^{high} CAFs exhibited lower survival than those with miR-21^{low} CAFs. The underlying mechanism was investigated *in vitro*. Conditioned medium (CM) from A549 lung cancer cells increased miR-21 expression in MRC-5 and IMR-90 lung fibroblasts through the transforming growth factor-β pathway, and induced CAF-like morphology and migratory capacity. MiR-21 up-regulation in lung fibroblasts induced a novel CAF-secreted protein, calumenin, as well as known CAF markers (periostin, α-smooth muscle actin, and podoplanin). Moreover, CM from the lung fibroblasts increased A549 cell proliferation in a calumenin-dependent manner. Thus, miR-21 expression in lung fibroblasts may trigger fibroblast trans-differentiation into CAFs, supporting cancer progression. Therefore, CAF miR-21 represents a pivotal prognostic marker for this scar-forming cancer of the lungs.

Cancer-stromal interactions play critical roles in cancer cell growth, invasion, metastasis, angiogenesis, and chemoresistance[1–3]. Cancer-associated fibroblasts (CAFs), or activated fibroblasts, are essential constituents of the cancer stroma that contribute to cancer progression and promote cancer cell growth. Although their origin remains controversial, CAFs are thought to be mainly derived from resting fibroblasts[4], which are activated to trans-differentiate into myofibroblasts/CAFs by paracrine signalling initiated by cancer cells. Transforming growth factor β (TGF-β) is the most potent activator of fibroblast trans-differentiation. In a previous study, we identified sub-epithelial myofibroblasts (SMFs) located within the alveolar septa and beneath the *in situ* proliferation of lung adenocarcinoma cells. We postulated that at least some of these SMFs transform into CAFs at the "central scar"[5], the central region of lung adenocarcinoma, which contains myofibroblasts/CAFs. CAFs have only recently been investigated with respect to their molecular, genetic, and epigenetic abnormalities in various organs, including the lungs. Since CAF abnormalities may represent a useful indicator for cancer prognosis, their complete characterisation should be pursued.

MicroRNAs (miRNAs) are a class of small (20–25 nucleotides in length), non-coding RNA species that play important roles in tuning various cellular functions, through the post-transcriptional regulation of target mRNAs. The roles of miRNAs in the development and progression of cancer cells are currently being intensively investigated. Although CAFs represent an attractive target for the development of novel drugs, studies have mainly focused on cancer cell-derived miRNAs, while the roles of stromal-derived miRNAs remain to be elucidated. Bronisz *et al.* demonstrated that the down-regulation of miR-320 in mammary stromal fibroblasts reprograms the tumour microenvironment by activating the pro-oncogenic secretome[6]. Moreover, Mitra *et al.* identified a set of three miRNAs (miR-31, miR-214, and miR-155) that reprogram normal fibroblasts into CAFs in ovarian cancer[7].

[1]Department of Pathology, Graduate School of Medicine, University of Tokyo, Tokyo, Japan. [2]Department of Cellular and Organ Pathology, Akita University Graduate School of Medicine, Akita, Japan. [3]Department of Integrative Pathology, Jichi Medical University, Tochigi, Japan. [4]Department of Clinical Laboratory, University of Tokyo Hospital, Tokyo, Japan. [5]Department of Thoracic Surgery, University of Tokyo Hospital, Tokyo, Japan. Akiko Kunita and Shigeki Morita contributed equally to this work. Correspondence and requests for materials should be addressed to M.F. (email: mfukayama-tky@umin.ac.jp)

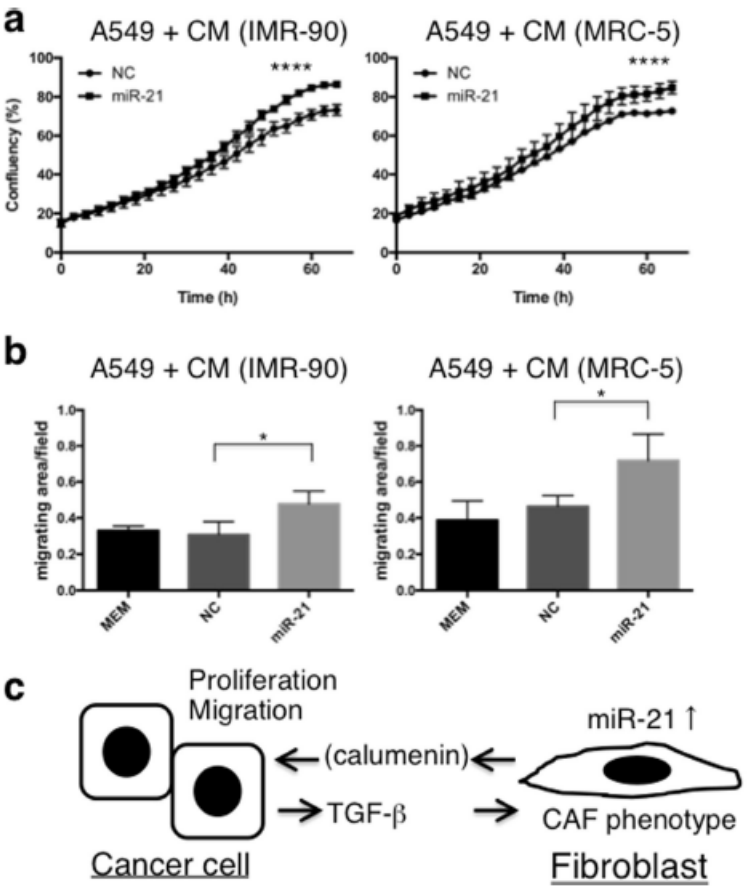

Figure 6. MiR-21-expressing lung fibroblasts affect the growth and migration of lung cancer cells through secretory molecules. (**a**) Cell proliferation assay for A549 cells following treatment with CM from miR-21-overexpressing IMR-90 and MRC5 fibroblasts (mean ± SD, n = 3, **** $P < 0.0001$). The proliferative capacity of lung cancer cells, cultured in CM from fibroblasts transfected with miR-21, was increased compared with the control group (NC). (**b**) A549 cell migration assay following treatment with CM from miR-21-overexpressing IMR-90 or MRC5 fibroblasts. Cell migration was analysed with the IncuCyte® ZOOM live cell imager and expressed as the area occupied by A549 cells on the bottom surface, normalised to the initial top value (mean ± SD, n = 4). (**c**) Schema of the interactions between cancer cells and fibroblasts in lung adenocarcinoma.

Proliferation assay. To examine the growth of monolayer cultures, 5×10^4 cells/well were seeded in 6-well plates, and cell confluence was monitored with the JuLI Stage automated cell imaging system and software (NanoEnTek, Seoul, Korea).

www.oncotarget.com Oncotarget, 2018, Vol. 9, (No. 43), pp: 27268-27279

Research Paper

Discovery and optimization of cardenolides inhibiting HSF1 activation in human colon HCT-116 cancer cells

Alina D. Nikotina[1], Lidia Koludarova[1], Elena Y. Komarova[1], Elena R. Mikhaylova[1], Nikolay D. Aksenov[1], Roman Suezov[1,3], Viktor G. Kartzev[2], Boris A. Margulis[1] and Irina V. Guzhova[1]

[1]Laboratory of Cell Protection Mechanisms, Institute of Cytology of Russian Academy of Sciences, St. Petersburg 194064, Russia

[2]InterBioscreen, Chernogolovka 142432, Russia

[3]Saint Petersburg Technical University, St. Petersburg 190013, Russia

Correspondence to: *Irina V. Guzhova,* ***email:*** *irina.guzh@gmail.com*

Keywords: *heat shock factor 1 (HSF1); Hsp70; anticancer drugs; combined antitumor therapy*

Received: *February 19, 2018* ***Accepted:*** *May 19, 2018* ***Published:*** *June 05, 2018*

ABSTRACT

Combinational anticancer therapy demonstrates increased efficiency, as it targets different cell-survival mechanisms and allows the decrease of drug dosages that are often toxic to normal cells. Inhibitors of the heat shock response (HSR) are known to reduce the efficiency of proteostasis mechanisms in many cancerous cells, and therefore, may be employed as anti-tumor drug complements. However, the application of HSR inhibitors is limited by their cytotoxicity, and we suggested that milder inhibitors may be employed to sensitize cancer cells to a certain drug.

We used a heat-shock element-luciferase reporter system and discovered a compound, CL-43, that inhibited the levels of heat shock proteins 40, 70 (Hsp70), and 90 kDa in HCT-116 cells and was not toxic for cells of several lines, including normal human fibroblasts. Consequently, CL-43 was found to reduce colony formation and motility of HCT-116 in the appropriate assays suggesting its possible application in the exploration of biology of metastasizing tumors. Importantly, CL-43 elevated the growth-inhibitory and cytotoxic activity of etoposide, cisplatin, and doxorubicin suggesting that the pro-drug has broad prospect for application in a variety of anti-tumor therapy schedules.

INTRODUCTION

Traditional anticancer drugs used for chemotherapy are often inefficient because tumor cells possess a powerful protective system based on molecular chaperones [1]. The expression of molecular chaperones, many of which belong to various families of heat shock proteins (Hsps), is controlled by heat shock transcription factors (HSFs) in most cases by HSF1 [2]. HSF1 governs the function of more than 1000 genes, some of which are functionally linked to tumor progression [3]. Typical products of HSF1 activation are heat shock proteins (Hsps) Hsp27, Hsp40, Hsp70 and Hsp90. Most Hsps are involved in a cell proteostasis mechanism that corrects the consequences of improper polypeptide synthesis-modification-transport and promotes the proteolytic elimination of irreversibly damaged proteins in proteasome/lysosome machineries [4].

The majority of HSF1 molecules are maintained in an inactive state in cytosol through binding to the complex containing Hsp90, Hsp70, and Hsp40; upon heat shock, HSF1 is phosphorylated, trimerizes, and migrates to the nucleus [5]. There the factor induces the expression of certain genes by binding to their 5′-upstream DNA motifs,

Wound-healing assay

HCT-116 cells were serum-deprived, and CL-43 at a concentration of 250 nM was added to the confluent monolayer. After 20 h of incubation, the HCT-116 monolayer was wounded by scratching with a 5 ml pipet tip. Wound-healing was monitored for 24 h with aid of JuLI Stage microscope (NanoEnTek, South Korea) and monitored by JuLi Software.

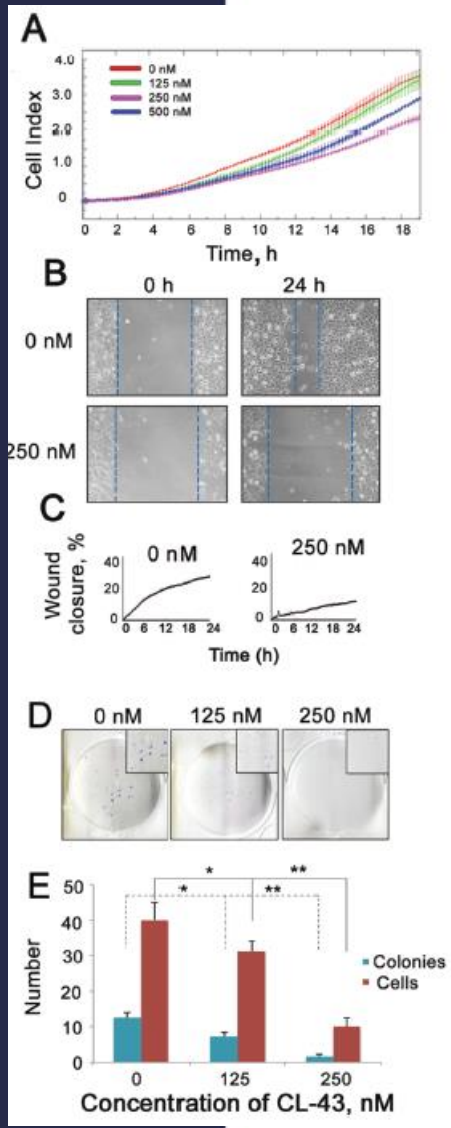

Figure 3: CL-43 reduces migratory and colony formation capacities. (**A**) HCT-116 cells were treated with CL-43 in various concentrations for 18 h, then collected, transferred to serum-free medium and seeded into the upper wells of CIM plates of the xCELLigence system. Lower chambers of CIM plates were filled with complete medium. Recording of cells migrated through the microporous membrane of CIM plates lasted 20 h. Representative data from three independent experiments is shown. (**B**, **C**) Wound healing assay was performed with the aid of a JuLI Stage microscope. Cells were cultivated in serum-free medium for 24 h in the presence of vehicle or 250 nM CL-43 before the monolayer was scratched. Recording lasted 24 h. The wound closure was detected with microscopy (B) and monitored by JuLi Software (C). (**D**) Colony formation assay obtained with HCT-116 cells in the presence of CL-43 in concentrations of 125 and 250 nM. (**E**) The number of colonies and average number of cells in each single colony were calculated with an aid of CQ1Confocal Quantitative Image Cytometer (Yokogawa, Japan).

Cold Spring Harbor Laboratory

bioRxiv
THE PREPRINT SERVER FOR BIOLOGY

New Results

Lineage tracing using a Cas9-deaminase barcoding system targeting endogenous L1 elements

Byungjin Hwang, Wookjae Lee, Sooyoung Yum, Yujin Jeon, Namjin Cho, Goo Jang, Duhee Bang

doi: https://doi.org/10.1101/367177

This article is a preprint and has not been peer-reviewed [what does this mean?].

Abstract | Info/History | Metrics | Supplementary material | Preview PDF

Abstract

Determining cell lineage and function is critical to understanding human physiology and pathology. Although advances in lineage tracing methods have provided new insight into cell fate, defining cellular diversity at the mammalian level remains a challenge. Here, we developed a genome editing strategy using a cytidine deaminase fused with inactive Cas9 (dCas9) to specifically target endogenous interspersed repeat regions in mammalian cells. The resulting mutation patterns served as a genetic barcode, which was induced by targeted mutagenesis with single-guide RNA (sgRNA), leveraging substitution events, and subsequent read out by a single primer pair. By analyzing interspersed mutation signatures, we show the accurate reconstruction of cell lineage using both bulk cell and single-cell data. We envision that our genetic barcode system will enable fine-resolution mapping of organismal development in healthy and diseased mammalian states.

Manual cell picking and monitoring for time-lapse imaging

All of the single-cell manipulations were conducted using a micromanipulator device (Nikon-Narishige, Tokyo, Japan) during observation under an inverted microscope. One day after transfection, the cells were trypsinized and washed in phosphate-buffered saline (PBS; Gibco, USA). To manually pick single-cells, the cell suspensions were placed in a drop of PBS with 0.5% FBS and covered by mineral oil (Sigma, USA). A single RFP-positive only cell was aspirated using a micro-injection pipette (diameter: 20 μm, ORIGIO, Charlottesville, VA) under fluorescence exposure. The aspirated single-cell was transferred to a 4 μl droplet of DMEM supplemented with 1% P/S, 1% NEAA, 100 mM 2-ME, and 10% FBS in a 100-mm dish and overlaid with mineral oil at a ratio of one cell to each droplet. The single-cells were cultured for 4 hours in a CO_2 incubator at 37□ and then moved to an incubator equipped with a JuLI™ Stage real-time cell history recorder (NanoEnTek), which enables the observation of cell growth using live, time-lapse imaging.

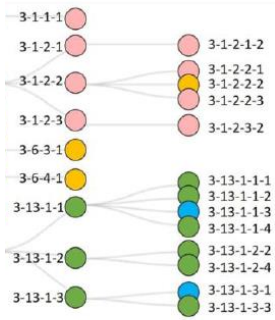

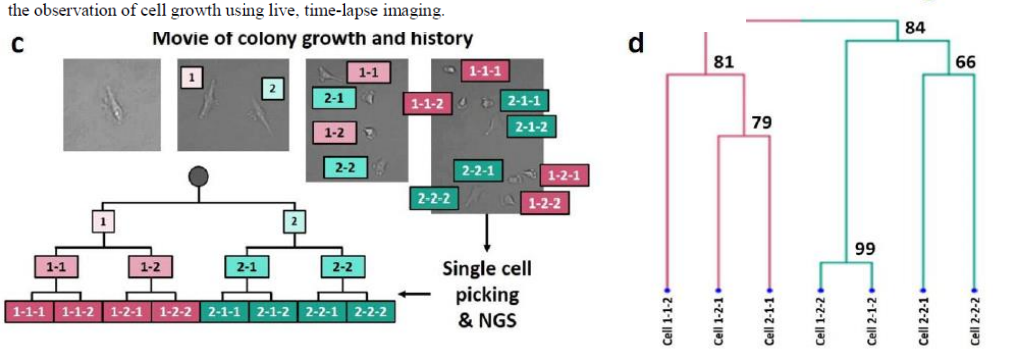

Figure 1. Targeted deaminase system for lineage tracing. a) Schematic overview of the targeted deaminase system. Red arrows indicate the single flanking primer pair used to amplify the targeted regions. The substitution pattern in the target region served as the cell barcode for tree reconstruction. b) Pairwise alignment of five representative target sites for sgRNA-1 and sgRNA-3 design. These regions were amplified using a single primer pair and alignment distinguished each target site by the different surrounding sequences. c) Editing efficiency of the two selected sgRNAs in the target region for HEK293T and HeLa cells. d) Correlation of editing efficiency between the first and second base 'C' in a specific window (4-8) within the sgRNA-3 spacer sequence in HEK293T cells (Spearman's correlation = 0.6 for HeLa cells).

Cellular and Molecular Life Sciences
https://doi.org/10.1007/s00018-018-2904-y

Cellular and Molecular Life Sciences

ORIGINAL ARTICLE

Pharmacological inhibition of store-operated calcium entry in MDA-MB-468 basal A breast cancer cells: consequences on calcium signalling, cell migration and proliferation

Iman Azimi[1,2,3] · Alice H. Bong[1] · Greta X. H. Poo[1] · Kaela Armitage[1] · Dawn Lok[1] · Sarah J. Roberts-Thomson[1] · Gregory R. Monteith[1,2]

Received: 4 February 2018 / Revised: 8 August 2018 / Accepted: 9 August 2018

Abstract
Store-operated Ca^{2+} entry is a pathway that is remodelled in a variety of cancers, and altered expression of the components of store-operated Ca^{2+} entry is a feature of breast cancer cells of the basal molecular subtype. Studies of store-operated Ca^{2+} entry in breast cancer cells have used non-specific pharmacological inhibitors, complete depletion of intracellular Ca^{2+} stores and have mostly focused on MDA-MB-231 cells (a basal B breast cancer cell line). These studies compared the effects of the selective store-operated Ca^{2+} entry inhibitors Synta66 and YM58483 (also known as BTP2) on global cytosolic free Ca^{2+} ($[Ca^{2+}]_{CYT}$) changes induced by physiological stimuli in a different breast cancer basal cell line model, MDA-MB-468. The effects of these agents on proliferation as well as serum and epidermal growth factor (EGF) induced migration were also assessed. Activation with the purinergic receptor activator adenosine triphosphate, produced a sustained increase in $[Ca^{2+}]_{CYT}$ that was entirely dependent on store-operated Ca^{2+} entry. The protease activated receptor 2 activator, trypsin, and EGF also produced Ca^{2+} influx that was sensitive to both Synta66 and YM58483. Serum-activated migration of MDA-MB-468 breast cancer cells was sensitive to both store-operated Ca^{2+} inhibitors. However, proliferation and EGF-activated migration was differentially affected by Synta66 and YM58483. These studies highlight the need to define the exact mechanisms of action of different store-operated calcium entry inhibitors and the impact of such differences in the control of tumour progression pathways.

Keywords Breast cancer · Orai1 · Store-operated Ca^{2+} entry · Synta66 · YM58483

Abbreviations

ATP	Adenosine triphosphate
CM	Complete media
CPA	Cyclopiazonic acid
DMEM	Dulbecco's modified Eagle's medium
EGF	Epidermal growth factor
EGFR	Epidermal growth factor receptor
ER	Endoplasmic reticulum
FBS	Foetal bovine serum
IP_3	Inositol 1,4,5-trisphosphate
PAR2	Protease-activated receptor 2
PBS	Phosphate-buffered saline
PLC	Phospholipase C
SOCE	Store-operated Ca^{2+} entry
SRM	Serum-reduced media
STIM1	Stromal interaction molecule 1
STR	Short tandem repeat

Electronic supplementary material The online version of this article (https://doi.org/10.1007/s00018-018-2904-y) contains supplementary material, which is available to authorized users.

✉ Gregory R. Monteith
gregm@uq.edu.au

[1] School of Pharmacy, The University of Queensland, Brisbane, QLD, Australia

[2] Mater Research Institute, Translational Research Institute, The University of Queensland, Brisbane, QLD, Australia

[3] Division of Pharmacy, College of Health and Medicine, University of Tasmania, Hobart, TAS, Australia

Introduction

The existence of a mechanism by which the depletion of intracellular Ca^{2+} stores triggers a Ca^{2+} influx pathway that is then used to refill Ca^{2+} stores was proposed by Putney in 1986 [1], with store-operated Ca^{2+} entry, one of the terms

Published online: 13 August 2018

Cell migration assay

Cell motility was measured using a collagen-based single cell migration assay and a live cell imaging system. 96-well plates were coated with 50 µL of collagen solution containing sterile-filtered 10× phosphate-buffered saline (PBS) (8% v/v), cell culture media (24% v/v), type I collagen from bovine skin, buffered to physiological pH with 1 M NaOH. After incubating plates at 37 °C and 5% CO_2 in humidified incubator for 1 h to allow collagen gel to solidify, cells were plated on top of the gel (500 cells, 100 µL volume per well). Post seeding (24 h), cell culture media were replaced with serum-reduced media (SRM, 0.5% FBS) containing Synta66 (10 µM) or YM58483 (10 µM) or DMSO control (0.1%) for 24 h. Media were replaced with either complete media (CM, 10% FBS) or SRM with EGF (50 ng/mL), containing DMSO control, Synta66 or YM58483. Plates were then placed in a JuLi™ Stage Live Cell Imaging System (NanoEnTek Inc. Seoul, South Korea) housed in a 37 °C and 5% CO_2 humidified incubator for 24 h with bright-field images acquired every 15 min. Single cell tracking was performed on images acquired 12 h after addition of EGF or complete media for a period of 12 h. ImageJ 1.49q software (NIH, Bethesda, MD, https://imagej.nih.gov/ij/) was used to track cells. Accumulated distance travelled by each cell was calculated and illustrated by Chemotaxis and Migration Tool V2.0 (Ibidi, Munich, Germany). Strict criteria were employed regarding exclusion of cells from analysis. Cells which died (loss of plasma membrane integrity or formation of apoptotic bodies), or moved into or out of the field of view during the period of migration assessment was excluded from analysis. Cells which clumped together were also excluded as only single cell motility was assessed.

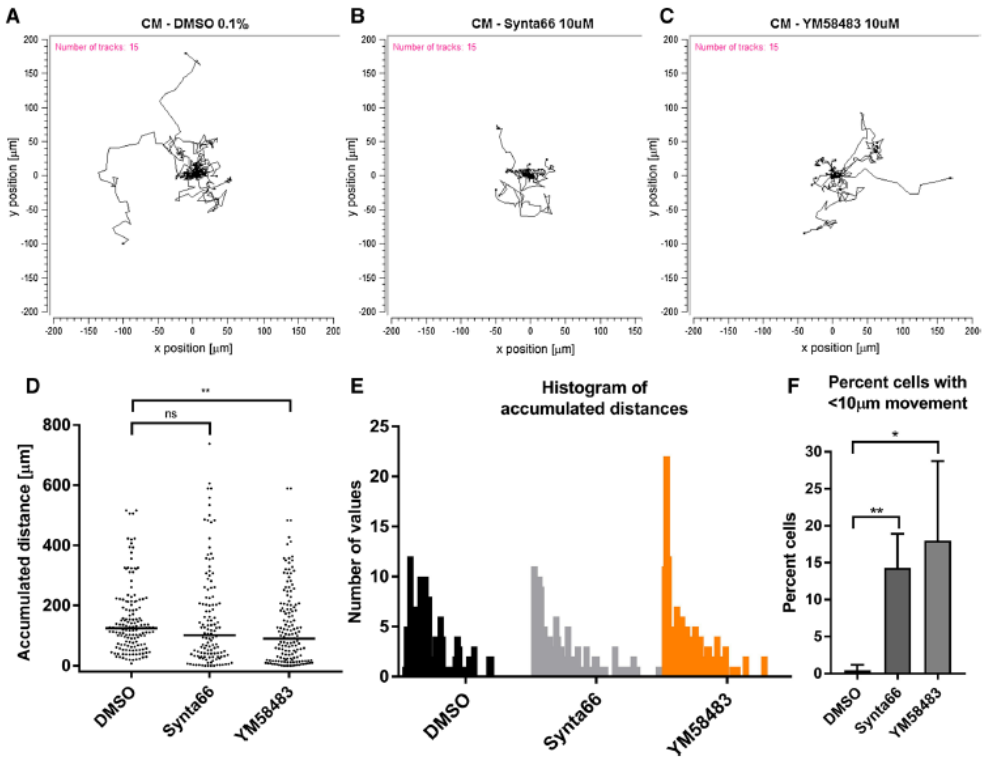

Fig. 4 Assessment of the effect of Synta66 and YM58483 on a complete media (CM)-model of cell migration. Cells were serum-deprived (0.5% FBS) for 24 h prior to addition of complete media (10% FBS) containing DMSO (0.1%), Synta66 (10 µM) or YM58483 (10 µM) for 24 h. Cell migration was analysed from 12 h to 24 h after addition of complete media. Representative spatial plots of DMSO control (**a**), Synta66 (**b**) and YM58483 (**c**) of 15 randomised cells from one experiment. **d** Quantitative analysis of the median accumulated distance travelled by all the cells from three independent experiment (duplicate wells) treated with DMSO control (total 152 cells), Synta66 (total 126 cells) or YM58483 (total number of 156 cells). *ns* not significant ($P > 0.05$), $^{**}P < 0.01$ (nonparametric Mann–Whitney test). **e** Histograms of accumulated distances travelled by cells binned at 10 µm intervals. **f** Percent of cells with accumulated distance travelled of less than 10 µm. Data are the mean ± SD from three independent experiments ($n = 3$). *ns* not significant ($P > 0.05$), $^{*}P < 0.05$, $^{**}P < 0.01$ (unpaired *t* test compared to the DMSO control)

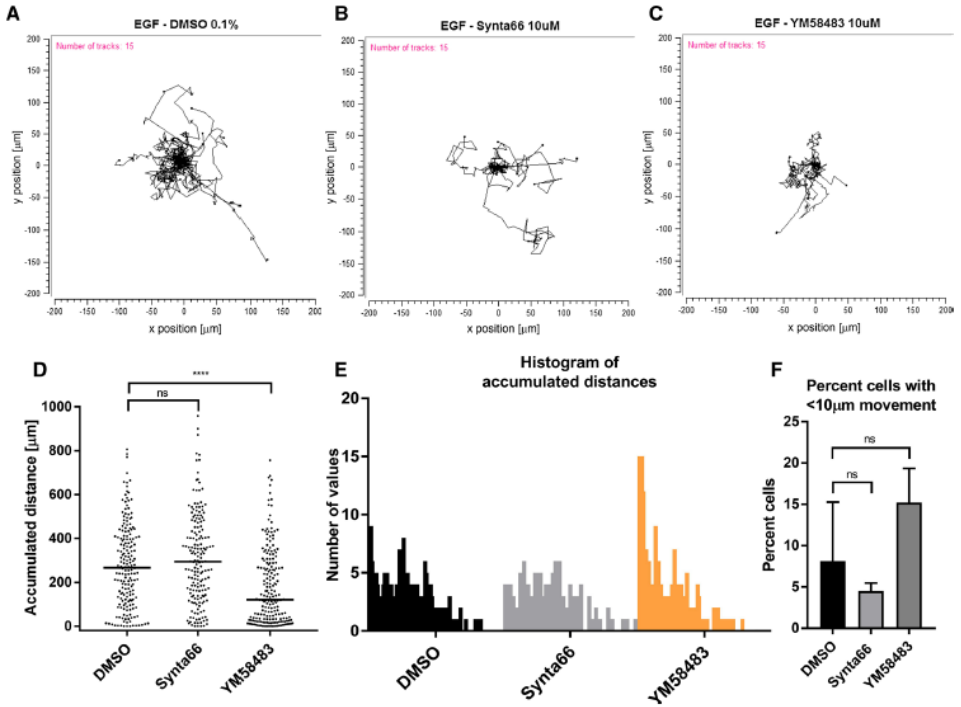

Fig. 5 Assessment of the effect of Synta66 and YM58483 on an EGF-model of cell migration. Cells were serum-deprived (0.5% FBS) for 24 h prior to addition of EGF (50 ng/mL) containing DMSO (0.1%), Synta66 (10 µM) or YM58483 (10 µM) for 24 h. Cell migration was analysed from 12 h to 24 h after EGF addition. Representative spatial plots of DMSO control (**a**), Synta66 (**b**) and YM58483 (**c**) of 15 randomised cells from one experiment. **d** Quantitative analysis of the median accumulated distance travelled by cells from three independent experiment (duplicate wells) treated with DMSO control (total number of 185 cells), Synta66 (total number of 176 cells) or YM58483 (total number of 198 cells). *ns* not significant ($P > 0.05$), $^{****}P < 0.0001$ (nonparametric Mann–Whitney test). **e** Histograms of accumulated distances travelled by cells binned at 10 µm intervals. **f** Percent of cells with accumulated distance travelled of less than 10 µm. Data are the mean ± SD from three independent experiments ($n = 3$). *ns* not significant ($P > 0.05$), $^{***}P < 0.0001$ (unpaired *t* test compared to the DMSO control)

SCIENTIFIC REPORTS

OPEN

Nuclear connectin novex-3 promotes proliferation of hypoxic foetal cardiomyocytes

Received: 23 April 2018
Accepted: 8 August 2018

Ken Hashimoto[1], Aya Kodama[1], Miki Sugino[1], Tomoko Yobimoto[1], Takeshi Honda[1,2], Akira Hanashima[1], Yoshihiro Ujihara[1] & Satoshi Mohri[1]

Loss of cardiomyocyte proliferative capacity after birth is a major obstacle for therapeutic heart regeneration in adult mammals. We and others have recently shown the importance of hypoxic in utero environments for active foetal cardiomyocyte proliferation. Here, we report the unexpected expression of novex-3, the short splice variant of the giant sarcomeric protein connectin (titin), in the cardiomyocyte nucleus specifically during the hypoxic foetal stage in mice. This nuclear localisation appeared to be regulated by the N-terminal region of novex-3, which contains the nuclear localisation signal. Importantly, the nuclear expression of novex-3 in hypoxic foetal cardiomyocytes was repressed at the postnatal stage following the onset of breathing and the resulting elevation of oxygen tension, whereas the sarcomeric expression remained unchanged. Novex-3 knockdown in foetal cardiomyocytes repressed cell cycle-promoting genes and proliferation, whereas novex-3 overexpression enhanced proliferation. Mechanical analysis by atomic force microscopy and microneedle-based tensile tests demonstrated that novex-3 expression in hypoxic foetal cardiomyocytes contributes to the elasticity/compliance of the nucleus at interphase and facilitates proliferation, by promoting phosphorylation-induced disassembly of multimer structures of nuclear lamins. We propose that novex-3 has a previously unrecognised role in promoting cardiomyocyte proliferation specifically at the hypoxic foetal stage.

While foetal cardiomyocytes (fCMs) in mammals actively proliferate in utero to form the primitive heart, they stop dividing soon after birth. For this reason, understanding the molecular mechanisms of active fCM proliferation is fundamental for therapeutic regeneration in adult hearts. Recently, we and others have shown that activation of fCM proliferation requires a low oxygen (O_2) condition in foetal hearts, prior to the onset of breathing at birth[1,2]. However, the underlying molecular mechanism of this activation is unknown. One study has shown that proliferation of mouse fCMs during the mid-embryonic stage (embryonic day, E12.5–E14.5) was maintained by hypoxia inducible factor-1α (Hif-1α)[3]. We have recently identified family with sequence similarity 64, member A (Fam64a; also known as Pimreg) as an essential molecule for hypoxic fCM proliferation[2]. However, the regulatory networks occurring among these and other unidentified molecules under hypoxic foetal conditions remain poorly understood.

Connectin (also known as titin; Ttn) is the largest protein discovered to date (3–4 MDa) and spans from the Z-disk, I-band and A-band to the M-band region of the sarcomere of cardiac and skeletal muscle[4,5]. It has 4 major isoforms, N2A, N2B, N2BA and foetal cardiac connectin, as well as numerous isoforms, including shorter fragments that are produced through complex alternative splicing pathways. Generally, connectin functions as an elastic molecular spring, and in cardiac muscle, it defines myocardial passive stiffness in diastole. However, connectin has recently been recognised to have additional functions, including acting as a structural and signalling molecule[6].

Our recent work on connectins has focused on their nuclear localisation. In *C. elegans* embryos, two connectin homologues, TTN-1/Ce-titin (2.2 MDa) and kettin (500–550 KDa), were detected at the interphase nuclear envelope[7], and kettin was also localised to mitotic spindles during mitosis. A similar nuclear localisation of kettin was observed in very early embryos[8,9]. In *Drosophila* embryos, a nuclear connectin was identified that differed from the major isoform found in the muscle sarcomere[10,11]. This protein was 1.9 MDa in size and showed significant homology to the N-terminal half of vertebrate connectin; it was named D-titin (also called Sls protein[12] or

[1]First Department of Physiology, Kawasaki Medical School, Kurashiki, Japan. [2]Department of Cardiovascular Surgery, Kawasaki Medical School, Kurashiki, Japan. Correspondence and requests for materials should be addressed to K.H. (email: khashimo@med.kawasaki-m.ac.jp)

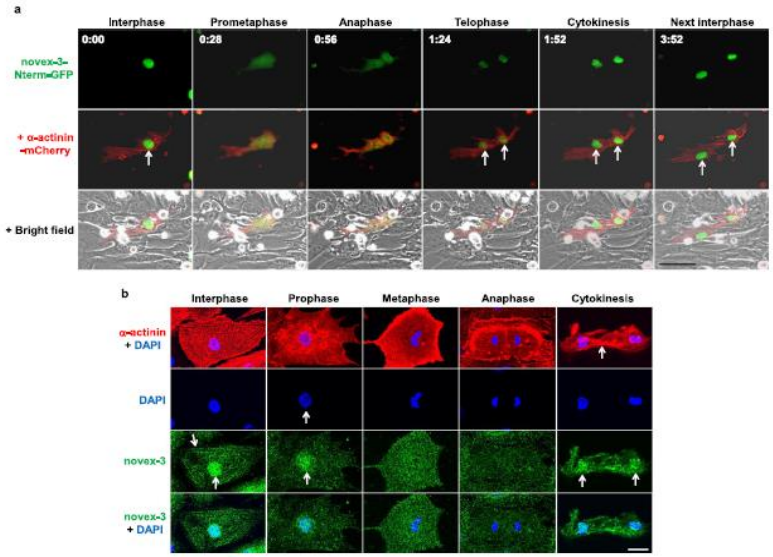

Figure 6. Nuclear function of novex-3 as a cell cycle promoter is ascribed to that in interphase, but not during mitosis. (**a**) A representative time-lapse recording of cell division dynamics of the E16 fCM doubly expressing novex-3-Nterm-GFP and sarcomeric α-actinin-mCherry (as a CM marker). In contrast to the clear nuclear expression observed during interphase (arrow), novex-3-Nterm expression was not localised to specific structures (spindles, spindle matrix, centrioles, or chromosomes) during mitosis; instead, it was diffusely spread throughout the cytoplasm following nuclear envelope breakdown at prometaphase. At telophase, when the nuclear envelope reassembled, the novex-3-Nterm re-accumulated in the newly formed daughter nuclei (arrows in telophase and cytokinesis), where it was maintained over the next interphase (arrows). The number on each panel indicates the time in (hours: minutes) elapsed from the time indicated in the first panel. Scale bar = 50 µm. (**b**) Cultured fCMs (E17–E18) were triple-stained with novex-3, sarcomeric α-actinin (as a CM marker), and DAPI. DAPI staining clearly defined each phase in mitosis, including prophase, metaphase, anaphase, and subsequent cytokinesis. In interphase fCMs, novex-3 was expressed both in nuclei and sarcomere (arrows). At this time point, sarcomere structure was intact, as indicated by α-actinin staining. In prophase, when chromosome condensation was visible as dot-like puncta by DAPI staining (arrow), novex-3 was still expressed in fCM nuclei (arrow), while sarcomere structure has begun to disassemble. After the nuclear envelope breakdown at prometaphase, novex-3 did not localise to the specific structures such as spindles, spindle matrix, centrioles, or chromosomes; instead it diffused throughout the cytoplasm. When the nuclear envelope reassembled during cytokinesis, novex-3 re-accumulated in the newly formed daughter nuclei (arrows). Scale bar = 20 µm.

Time-lapse imaging analysis. Isolated fCMs expressing novex-3-Nterm-GFP and sarcomeric α-actinin-mCherry were placed on the stage of an inverted fluorescence microscope (All-in-One Fluorescence Microscope; Keyence, Japan) equipped with a stage incubation system. The molecular dynamics of both proteins during fCM cell division were recorded at 28 min intervals by time-lapse imaging. In separate experiments, time-lapse images were similarly obtained with the microscopic live cell analyser (JuLI Stage; NanoEnTek, Korea) to quantify the rate of fCM cell division. Complete fCM cell division events, in which mitosis was followed by cytokinesis and resulted in the generation of two daughter cells (an example shown in Fig. 6a), were manually counted and presented as the percentage of total fCMs.

SCIENCE TRANSLATIONAL MEDICINE | RESEARCH ARTICLE

ASTHMA

An extracellular matrix fragment drives epithelial remodeling and airway hyperresponsiveness

Dhiren F. Patel[1], Teresa Peiró[1,2], Amelia Shoemark[3], Samia Akthar[1], Simone A. Walker[1], Aleksander M. Grabiec[4,5], Patricia L. Jackson[6,7], Tracy Hussell[4], Amit Gaggar[6,7], Xin Xu[6,7], Jennifer L. Trevor[6,7], Jindong Li[6,7], Chad Steele[6], Gael Tavernier[8,9], J. Edwin Blalock[6], Robert M. Niven[8,9], Lisa G. Gregory[1], Angela Simpson[8,9], Clare M. Lloyd[1], Robert J. Snelgrove[1]*

It is anticipated that bioactive fragments of the extracellular matrix (matrikines) can influence the development and progression of chronic diseases. The enzyme leukotriene A_4 hydrolase (LTA_4H) mediates opposing proinflammatory and anti-inflammatory activities, through the generation of leukotriene B_4 (LTB_4) and degradation of pro-neutrophilic matrikine Pro-Gly-Pro (PGP), respectively. We show that abrogation of LTB_4 signaling ameliorated inflammation and airway hyperresponsiveness (AHR) in a murine asthma model, yet global loss of LTA_4H exacerbated AHR, despite the absence of LTB_4. This exacerbated AHR was attributable to a neutrophil-independent capacity of PGP to promote pathological airway epithelial remodeling. Thus, we demonstrate a disconnect between airway inflammation and AHR and the ability of a matrikine to promote an epithelial remodeling phenotype that negatively affects lung function. Subsequently, we show that substantial quantities of PGP are detectable in the sputum of moderate-severe asthmatics in two distinct cohorts of patients. These studies have implications for our understanding of remodeling phenotypes in asthma and may rationalize the failure of LTA_4H inhibitors in the clinic.

INTRODUCTION

Tissue inflammation and remodeling are cardinal features of many chronic diseases, as exemplified within the lungs, whereby they are hallmarks of genetic disorders such as cystic fibrosis (CF), as well as common lung diseases such as asthma and chronic obstructive pulmonary disease (COPD), which have emerged as a leading cause of morbidity and mortality worldwide. It had traditionally been hypothesized that chronic inflammation was driving the airway remodeling, but it is increasingly accepted that these features of disease can develop in parallel and that remodeling can even develop independently of the inflammation (*1*). Consequently, the mediators and mechanisms that instigate airway remodeling are still incompletely understood but are critical in dictating future efforts to develop effective treatment strategies.

Leukotriene B_4 (LTB_4) is generated intracellularly by the enzyme leukotriene A_4 hydrolase (LTA_4H) (*2*) and upon release binds to leukotriene B_4 receptor 1 (BLT1) (*3*). LTB_4 functions as a potent chemotactic factor and activator for various inflammatory cells and instigates pathological inflammation observed in a multitude of chronic diseases (*4*–*6*). Consequently, there has been a concerted pharmaceutical effort to develop LTA_4H inhibitors to ameliorate LTB_4-mediated pathology, but these inhibitors have failed to demonstrate efficacy in the clinic (*7*). Most recently, the LTA_4H inhibitor JNJ-40929837 was assessed in a human bronchial allergen challenge model of asthma, but despite demonstrating clear target engagement and reducing LTB_4, this drug failed to show any clinical benefit over placebo (*8*).

The extracellular matrix (ECM) is the noncellular component of tissues that provides a scaffold for constituent cells and is critical in the provision of biological cues that dictate development, homeostasis, inflammation, and repair. Degradation of the ECM can liberate biologically active fragments, termed matrikines, which can dictate the progression of inflammation and injury seen in chronic lung diseases (*9*). One such matrikine is the tripeptide Pro-Gly-Pro (PGP) that is liberated from ECM collagen via the sequential enzymatic activity of matrix metalloproteinases (MMPs) and prolylendopeptidase (*10*). Once liberated, PGP can subsequently be chemically acetylated through the action of reactive aldehydes to a species that displays enhanced in vivo stability, AcPGP (N-acelytated PGP) (*11*). PGP and AcPGP function as neutrophil chemoattractants by mimicking key sequences found in glutamic acid, leucine, arginine–positive (ELR^+) chemokines and binding to CXCR1/2 (*10*, *12*). Previously, we demonstrated that LTA_4H has a second anti-inflammatory activity, whereby it degrades PGP to facilitate the resolution of neutrophilic inflammation (*11*, *13*, *14*). Conversely, AcPGP is resistant to this LTA_4H-mediated degradation (*11*). Accordingly, it seems that the LTA_4H-PGP degradation pathway is perturbed in chronic lung diseases leading to the accumulation of PGP, which may subsequently be converted to AcPGP (*11*, *15*), with both species subsequently driving inflammation and pathology (*10*, *15*, *16*). LTA_4H therefore represents a highly unusual enzyme with opposing proinflammatory and anti-inflammatory activities that dictate the amplitude and persistence of inflammation, potentially accounting for the failure of LTA_4H inhibitors in a clinical setting.

Here, we assessed this dual functionality of LTA_4H in defining the pathogenesis of asthma. We demonstrate that global deletion of LTA_4H abolished LTB_4-driven inflammation but paradoxically exacerbated airway hyperresponsiveness (AHR) owing to PGP accumulation and a

[1]Inflammation Repair and Development, National Heart and Lung Institute, Imperial College London, London SW7 2AZ, UK. [2]Departamento de Ciencias Biomédicas, Universidad Cardenal Herrera–CEU, CEU Universities, Valencia 46115, Spain. [3]Royal Brompton and Harefield National Health Service (NHS) Trust, London SW3 6NP, UK. [4]Manchester Collaborative Centre for Inflammation Research, University of Manchester, Manchester M13 9NT, UK. [5]Department of Microbiology, Faculty of Biochemistry, Biophysics and Biotechnology, Jagiellonian University, Kraków 30-387, Poland. [6]Division of Pulmonary, Allergy and Critical Care Medicine, Program in Protease and Matrix Biology, Gregory Fleming James Cystic Fibrosis Centre and Lung Health Center, University of Alabama at Birmingham, Birmingham, AL 35294, USA. [7]Birmingham VA Medical Center, Birmingham, AL 35233, USA. [8]Division of Infection, Immunity and Respiratory Medicine, School of Biological Sciences, Faculty of Biology, Medicine and Health, University of Manchester, Manchester Academic Health Science Centre, Manchester M13 9NT, UK. [9]Manchester University NHS Foundation Trust, Manchester M23 9LT, UK. *Corresponding author. Email: robert.snelgrove@imperial.ac.uk

Assessment of human bronchial epithelial cell proliferation

Primary human normal bronchial epithelial cells (Lonza) were cultured for expansion in a 75-cm^3 flask (Corning), coated with type 1 collagen (30 μg/ml; Sigma-Aldrich), in Lonza bronchial epithelial growth medium (BEGM). Once more than 90% confluence was achieved, the cells were removed with trypsin (TrypLE Express Enzyme, Gibco) and plated onto a 96-well plate at a density of 5000 cells per well. The cells were supplemented with BEGM or with BEGM containing AcPGP (10 μg/ml, 1 μg/ml, 100 ng/ml, or 10 ng/ml). For assessment of a CXCR1/2-dependent mechanism, epithelial cells were incubated for 1 hour at 37°C with anti-CXCR1 and anti-CXCR2 antibodies (1 μg/ml; R&D Systems) or IgG2a isotype control antibodies (2 μg/ml; R&D Systems) before addition of AcPGP (10 ng/ml). The cells were placed in an incubator for 4 hours for acclimatization and to avoid potential condensation on the lid. Snapshots of each well were recorded at 30-min intervals over 72 hours using the JuLI Stage Real-Time Cell History Recorder (NanoEnTek Inc.). Percentage cell confluence was automatically recorded for every snapshot of each respective well. At the end of the experiment, the cells were fixed in 10% neutral buffered formalin (Sigma-Aldrich) for subsequent analysis. Ki-67 staining was performed using a rat anti-mouse Ki-67 primary antibody diluted 1:500 (eBioscience). A Cy3-conjugated goat anti-rat antibody (Jackson ImmunoResearch) diluted 1:500 was subsequently added to enumerate Ki-67 positively stained cells. The cells were then counterstained with a DAPI dye (Sigma-Aldrich) diluted 1:1000. The number of DAPI-positive cells and the number of DAPI and Ki-67 double-positive cells were counted to determine the percentage Ki-67–positive cells per well.

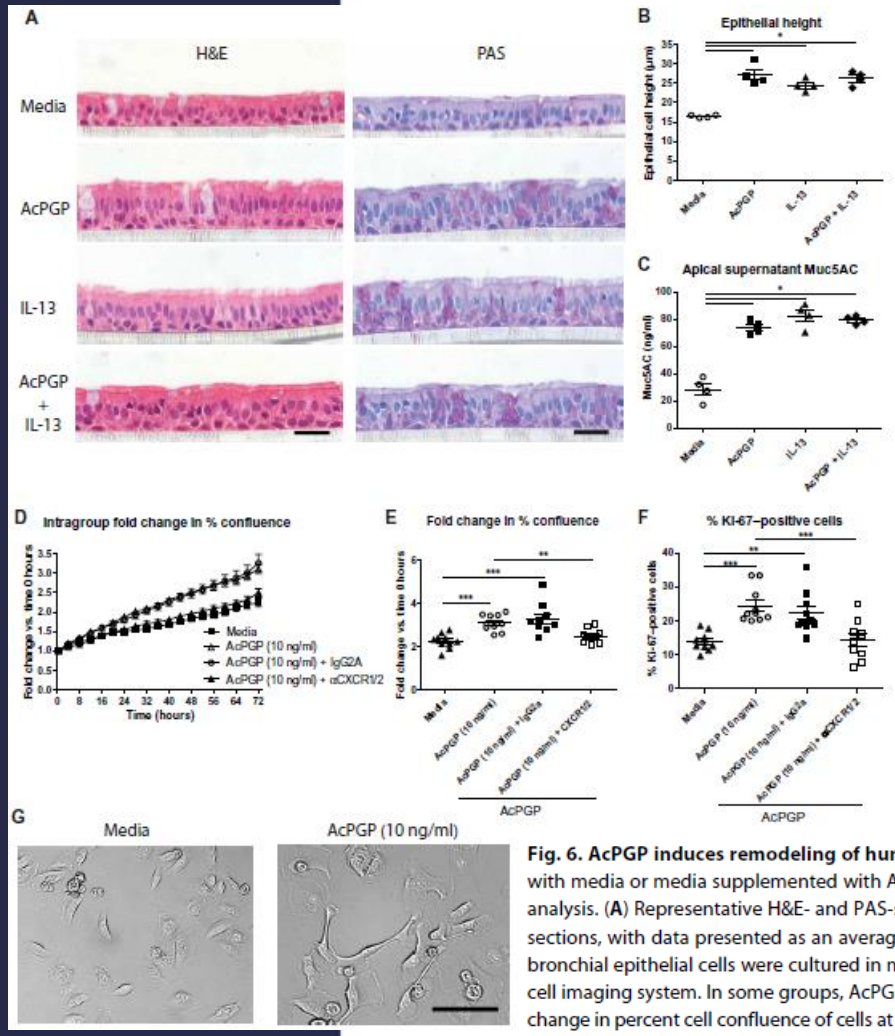

Fig. 6. AcPGP induces remodeling of human bronchial epithelial cells. Normal human bronchial epithelial cells were cultured at ALI. Respective wells were treated with media or media supplemented with AcPGP (10 μg/ml) and/or IL-13 (10 ng/ml) for 7 days. Apical supernatants were collected, and cells were fixed for histological analysis. (**A**) Representative H&E- and PAS-stained sections of ALI culture epithelium after 7 days of treatment. (**B**) Epithelial cell height was assessed from H&E-stained sections, with data presented as an average per well. (**C**) Apical supernatant Muc5AC was assessed by ELISA at day 7 after treatment. Undifferentiated normal human bronchial epithelial cells were cultured in media or media supplemented with AcPGP (10 ng/ml) and visualized over a period of 72 hours using a JuLI Stage automated cell imaging system. In some groups, AcPGP-treated cells were preincubated with either anti-CXCR1/2 antibodies or IgG2a isotype control antibody. (**D**) Intragroup fold change in percent cell confluence of cells at 72 hours after each treatment relative to 0 hours. (**E**) Fold change in cell confluence over 72-hour period depicted for individual wells in each treatment group. (**F**) After 72 hours, the cells were fixed and stained for Ki-67, with Ki-67–positive cells expressed as a percentage of 4′,6-diamidino-2-phenylindole (DAPI)–positive cells. (**G**) Bright-field image of epithelial cells treated with media or AcPGP (10 ng/ml) after 72 hours. Figures (A) to (C) present combined data from two independent experiments with two wells per group in each experiment. Figures (D) to (F) represent data combined from two independent experiments with five wells per group in each experiment. Results depicted as means ± SEM. $*P < 0.05$, $**P < 0.01$, $***P < 0.001$, using Mann-Whitney statistical test (B and C) or analysis of variance (ANOVA) with Bonferroni correction (E and F). Scale bars, 20 μm.

Materials Science & Engineering C 93 (2018) 429–436

Contents lists available at ScienceDirect

Materials Science & Engineering C

journal homepage: www.elsevier.com/locate/msec

Synthesis of fluorescent silicon quantum dots for ultra-rapid and selective sensing of Cr(VI) ion and biomonitoring of cancer cells

Le Minh Tu Phan[a], Seung Hoon Baek[a], Thang Phan Nguyen[a], Kyoung Yeol Park[a], Siyoung Ha[a], Rafia Rafique[a], Suresh Kumar Kailasa[a,b], Tae Jung Park[a,*]

[a] Department of Chemistry, Institute of Interdisciplinary Convergence Research, Research Institute of Halal Industrialization Technology, Chung-Ang University, 84 Heukseok-ro, Dongjak-gu, Seoul 06974, Republic of Korea
[b] Department of Applied Chemistry, S. V. National Institute of Technology, Surat 395 007, Gujarat, India

ARTICLE INFO

Keywords:
Si QDs
Cr(VI) detection
Cell imaging
Fluorescence quenching
Water samples

ABSTRACT

A facile one-step synthetic approach was developed for fabrication of fluorescent silicon quantum dots (Si QDs) and used as a probe for fluorescence detection of hexavalent chromium (Cr (VI)) in environmental water samples. The as-prepared Si QDs exhibit a strong fluorescence emission peak at 520 nm with a quantum yield of 14.2%. The fluorescent Si QDs were rapidly produced by using ascorbic acid as a reductant at 55 °C. The emission peak of Si QDs at 420 nm was effectively quenched upon the addition of Cr(VI). The Si QDs acted as the best fluorescent probe for the detection of Cr(VI) at PBS pH 7.4. The developed probe possessed a good linear correlation (R^2 = 0.992) between Cr(VI) concentration (1.25–40 μM) and the $(F_0\text{-}F)/F_0$ values with a detection limit of 0.65 μM. Furthermore, the Si QDs served as a bio-probe for fluorescence imaging of A549 lung cancer cells and cell viability results confirmed the good biocompatible nature of Si QDs. The as-fabricated Si QDs show several advantages such as rapidity, selectivity and biocompatibility for sensing of Cr(VI) and imaging of A549 cells, which opens a facile analytical platform for environmental and bioimaging applications.

1. Introduction

In the past several decades, the amount of heavy metals has been increased in the environment due to the rapid industrialization and other anthropogenic activities [1]. Chromium pollution is mainly due to the various industrial processes that includes coal-burning power plants, chrome plating, gold mining, volcanic emissions, and waste combustion [2]. Mostly, chromium exists in two oxidation states, i.e., Cr(III) and Cr(VI). Among these, Cr(VI) poses a serious threat to human health and environment compared to Cr(III), because of its high solubility and carcinogenic activity towards nucleic acids even at ultra-trace level [3]. Biochemical studies revealed that Cr(VI) ion was easily entered cell membranes and reduced to Cr(III), generating intermediate species of chromium, which leads to form the radicals of various chemical species [4]. Due to its high cellular uptake, it inhibits several biochemical pathways in cells, which can induce the toxicity to various cells and cause chemical-DNA damage via DNA-reactive mechanism [5]. As a result, the maximum allowable concentration for Cr(VI) in drinking water is at a lower micromolar level, which were set by many nations [6]. In this connection, the development of a simple and rapid analytical system is highly desirable for the detection of Cr(VI) in environmental and food samples.

Several analytical techniques including atomic absorption spectroscopy [7], UV–visible spectroscopy [8], fluorescence spectroscopy [9,10], high pressure liquid chromatography- inductively coupled plasma mass spectrometry [11], X-ray fluorescence spectrometry [12], and atomic emission spectrometry [13] have been used for the detection of Cr(IV) in various samples. These methods exhibited superior accuracy and precision. However, they usually suffer from disadvantages such as sophisticated pretreatment, requirement of professional operation, and also high-cost, which render them unsuitable for real-time field monitoring.

Recently, semiconductor nanocrystals, or quantum dots (QDs) have widely attracted in various fields of science because of their special optoelectronic properties including, strong absorption, high quantum yield, size-tunable photoluminescent (PL) emission, and high stability [14]. However, toxic inorganic precursors are commonly used in the synthesis of traditional QDs that may cause toxic effects to various biological systems [15]. Similarly, carbon dots have also been served as effective fluorescent probes for assaying of various metal ions including Cr(VI), Fe(III) and Al(III) ions in various samples [16–19]. Although the CDs-based fluorescence methods have proved as simple analytical

* Corresponding author.
E-mail address: tjpark@cau.ac.kr (T.J. Park).

https://doi.org/10.1016/j.msec.2018.08.024
Received 26 January 2018; Received in revised form 12 July 2018; Accepted 7 August 2018
Available online 08 August 2018
0928-4931/

2.6. Cell imaging using Si QD as bioimaging probes

For imaging studies, A549 lung cancer cells were cultured in 5% CO_2 humidified incubator at 37 °C. The cultured A549 cells (1×10^5) were placed on cover slips and rinsed twice with PBS. The cells were treated with Si QDs for 1 h. The cover slips of Si QDs-treated A549 cells were mounted onto glass slides. The bio-imaging nature of Si QDs was examined by fluorescence microscopy (Automated cell imaging system, JuLI Stage, NanoEnTek, Seoul, Korea).

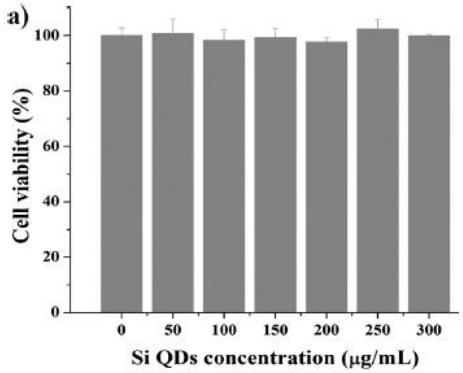

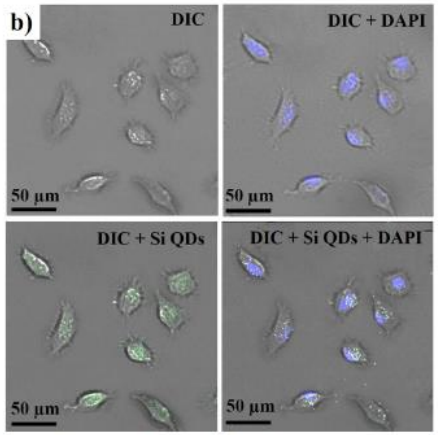

Fig. 7. (a) Cytotoxicity studies of Si QDs at different concentrations (50, 100, 150, 200, 250, 300, μg/mL) on A549 lung cancer cells. (b) Differential interference contrast (DIC) and fluorescence images of A549 cell line after incubation with Si QDs and 4′,6-diamidino-2-phenylindole (DAPI), respectively.

Zorea et al. *Cell Death and Disease* (2018)9:944
DOI 10.1038/s41419-018-1025-8

Cell Death & Disease

ARTICLE Open Access

IGF1R upregulation confers resistance to isoform-specific inhibitors of PI3K in *PIK3CA*-driven ovarian cancer

Jonatan Zorea[1], Manu Prasad[1], Limor Cohen[1], Nan Li[2,3], Roman Schefzik[2], Susmita Ghosh[1], Barak Rotblat[4], Benedikt Brors[5] and Moshe Elkabets[1]

Abstract

Genomic alterations (GA) in *PIK3CA* leads to the hyper-activation of the phosphatidylinositol-4, 5-bisphosphate 3-kinase (PI3K) pathway in more than 20% of ovarian cancer (OC) patients. Therefore, PI3K therapies are under clinical evaluation for this subset of patients. Evidently, in clinical trials testing the efficacy of isoform-specific inhibitors of PI3K (PI3Ki), patients having a stable disease eventually relapse, as tumors become resistant to treatment. Hence, there is an urgent clinical need to develop new therapeutic combinations to improve the efficacy of PI3Ki in PIK3CA-driven OC patients. Here we identified the molecular mechanism that limits the efficacy of the beta-sparing PI3Ki, Taselisib (GDC0032), in *PIK3CA*-mutated OC cell lines (IGROV1 and OAW42) that acquired resistance to GDC0032. By comparing the molecular profile of GDC0032-sensitve and -resistant OC cell lines, we found that AKT/mTOR inhibition is required for GDC0032 efficacy. In resistant cells, the sustained activation of AKT/mTOR was regulated by the upregulation of the insulin growth factor 1 receptor (IGF1R). Knockdown of IGF1R re-sensitized cells to GDC0032 in vitro, and the combination of AEW541, an IGF1R inhibitor, with GDC0032 exhibited potent anti-tumor activity in vitro and in vivo. We further demonstrated that IGF1R regulates tumor cell proliferation in IGROV1 cells, whereas in OAW42, it determines autophagy as well. Overall, our findings suggest that the dual inhibition of PI3K and IGF1R may be considered as a new therapeutic strategy in *PIK3CA*-driven OC.

Introduction

The phosphatidylinositol 3-kinase (PI3K) pathway is a key regulator of the survival, growth, and metabolism of normal and malignant cells[1,2]. This pathway is often hyperactivated due to genomic alterations (GA) in PI3K pathway-related genes such as deletions in *PTEN*, and mutations or amplifications in *PIK3CA, AKT3, AKT2, and AKT1*[3–7]. In ovarian cancer (OC) patients, point mutations or amplifications of the *PIK3CA* gene, which encodes the p110α catalytic subunit of the PI3K complex, are present in >20% of all OC types[3–6]. Around 240,000 OC patients are diagnosed annually; of these, ~50,000 harbor GA in *PIK3CA*[8]. Therefore, identifying potent anti-cancer therapies for this subset of OC patients is essential.

Cancer cells with GA in *PIK3CA* have been shown to be more susceptible to isoform-specific inhibitors of the PI3K pathway (PI3Ki) in vitro, in vivo, and in patients than tumor cells with wild-type *PIK3CA*[9–19]. One of the most promising PI3Ki is GDC0032, a small molecule that blocks p110α, p110δ, and p110γ (p110β sparing). GDC0032 has exhibited clinical activity in tumors harboring *PIK3CA* alterations in early clinical trials[14,15], but eventually all patients relapsed and developed resistance. Such results suggest that treating *PIK3CA*-driven OC with PI3Ki is a good therapeutic strategy, but new therapeutic

Correspondence: Moshe Elkabets (moshee@bgu.ac.il)
[1]The Shraga Segal Dept. of Microbiology, Immunology and Genetics, Faculty of Health Sciences, Ben-Gurion University of the Negev, Beer-Sheva 84105, Israel
[2]Division of Somatic Evolution and Early Detection, German Cancer Research Center (DKFZ), Heidelberg, Germany
Full list of author information is available at the end of the article.
Edited by: I. Amelio

Official Journal of the Cell Death Differentiation Association

SPRINGER NATURE
CDDpress

Imaging

Live cell imaging and time series recording were performed using the Juli™ Stage Real-Time Cell History Recorder. Punctate structures were imaged using both the ImageStream and Zeiss Axio Observer 7. IHC slides were scanned using the Panoramic MIDI II scanner, 3DHISTECH.

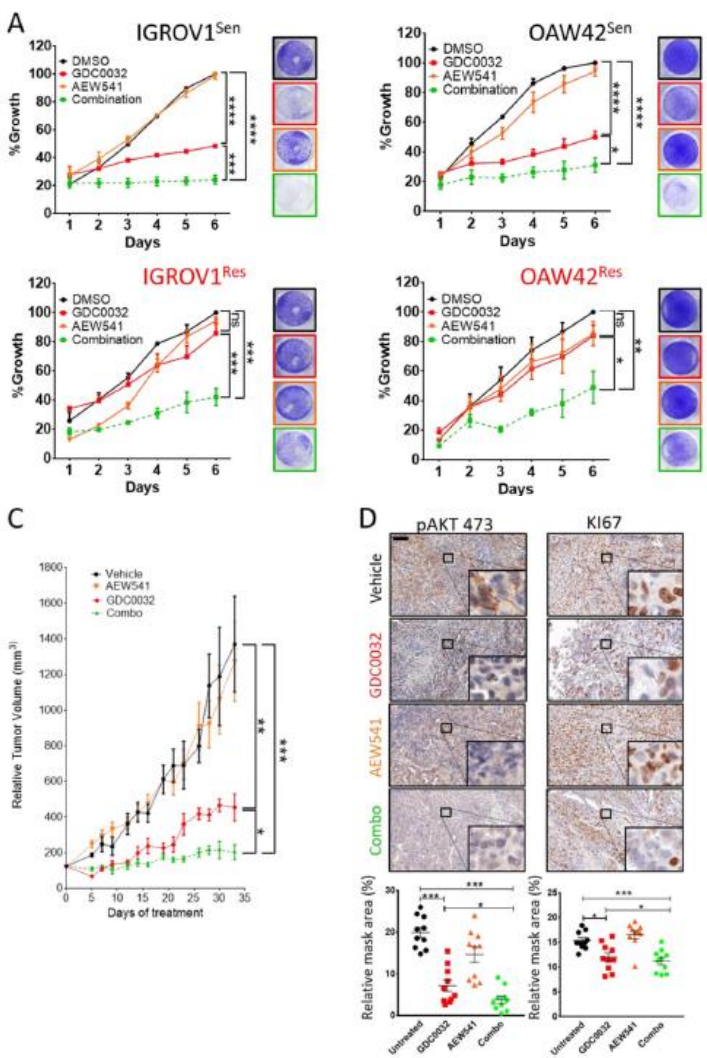

Fig. 3 Combining GDC0032 and AEW541 enhances tumor growth arrest. **A** The growth of IGROV1 and OAW42, sensitive and resistant cells, treated with DMSO (black), GDC0032 (red), AEW541 (orange), or AEW541-GDC0032 (green) was monitored by a live cell imager every 24 h and quantified by JuliStat. After 6 days of incubation, cells were fixed and stained using crystal violet (mean ± S.E.M. $n = 3$, $^{*}P < 0.05$, $^{**}P < 0.01$, $^{***}P < 0.01$, $^{****}P < 0.0001$). **B** Whole-cell lysate western blot analysis of AKT, and S6 from both cell lines, sensitive and resistant, treated for 24 h as indicated. **C** Four arms of tumor-bearing mice were treated daily as indicated. Tumor dimensions were measured every 2 days using a caliper and the relative tumor volume was calculated using the formula $V = (L \times W \times W) / 2$, where V is the tumor volume, W is the tumor width, and L is the tumor length. (mean ± S.E.M. n (of mice in a group) $>= 4$, $^{*}P < 0.05$, $^{**}P < 0.01$, $^{***}P < 0.01$). **D** KI67 and pAKT473 IHC staining of tumors from the four arms as indicated (scale bar of 100um). The relative mask area of each arm was calculated and presented in a bar graph below each image panel. (mean ± S.E.M. $n = 10$, $^{**}P < 0.01$, $^{***}P < 0.01$, $^{****}P < 0.0001$)

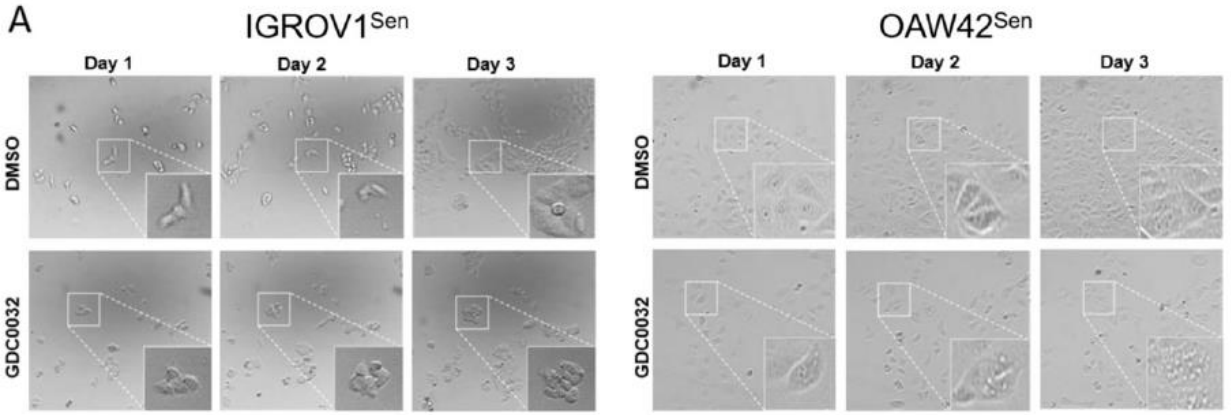

Fig. 4 IGF1R determines autophagy in OAW42 cells. **A** Live cell imaging showing the formation of punctate structures in OAW42^{Sen} cells treated with GDC0032 over time. **B** The changes in LC3B levels in both OAW42^{Sen} and IGROV1^{Sen} cells were first quantified by whole-cell lysate western blot analysis in a time series (hours) of 50 nM GDC0032 treatment. Second, punctate structures were stained after 24 h of treatment, using the Cyto-id kit and the average number of punctate structures per nucleus was calculated using the ImageStream count feature (mean ± S.E.M. $n > 1000$, $^{***}P < 0.01$). Last, punctate structures were imaged using a Zeiss inverted microscope (×40). **C** OAW42^{Res} cells treated as indicated and the average number of punctate structures per nucleus was imaged using an Zeiss inverted microscope (X40) and calculated using the ImageStream count feature. (mean ± S.E.M. $n > 1000$, $^{***}P < 0.01$). **D** A scheme summarizing the resistance mechanism involving IGF1R in OAW42^{Res} cells

BIOMOLECULES & THERAPEUTICS

Original Article
Biomol Ther 26(5), 474-480 (2018)

Two-Cell Spheroid Angiogenesis Assay System Using Both Endothelial Colony Forming Cells and Mesenchymal Stem Cells

Sajita Shah and Kyu-Tae Kang*

College of Pharmacy, Duksung Innovative Drug Center, Duksung Women's University, Seoul 01369, Republic of Korea

Abstract

Most angiogenesis assays are performed using endothelial cells. However, blood vessels are composed of two cell types: endothelial cells and pericytes. Thus, co-culture of two vascular cells should be employed to evaluate angiogenic properties. Here, we developed an *in vitro* 3-dimensional angiogenesis assay system using spheroids formed by two human vascular precursors: endothelial colony forming cells (ECFCs) and mesenchymal stem cells (MSCs). ECFCs, MSCs, or ECFCs+MSCs were cultured to form spheroids. Sprout formation from each spheroid was observed for 24 h by real-time cell recorder. Sprout number and length were higher in ECFC+MSC spheroids than ECFC-only spheroids. No sprouts were observed in MSC-only spheroids. Sprout formation by ECFC spheroids was increased by treatment with vascular endothelial growth factor (VEGF) or combination of VEGF and fibroblast growth factor-2 (FGF-2). Interestingly, there was no further increase in sprout formation by ECFC+MSC spheroids in response to VEGF or VEGF+FGF-2, suggesting that MSCs stimulate sprout formation by ECFCs. Immuno-fluorescent labeling technique revealed that MSCs surrounded ECFC-mediated sprout structures. We tested vatalanib, VEGF inhibitor, using ECFC and ECFC+MSC spheroids. Vatalanib significantly inhibited sprout formation in both spheroids. Of note, the IC_{50} of vatalanib in ECFC+MSC spheroids at 24 h was 4.0 ± 0.40 μM, which are more correlated with the data of previous animal studies when compared with ECFC spheroids (0.2 ± 0.03 μM). These results suggest that ECFC+MSC spheroids generate physiologically relevant sprout structures composed of two types of vascular cells, and will be an effective pre-clinical *in vitro* assay model to evaluate pro- or anti-angiogenic property.

Key Words: Angiogenesis, Endothelial colony forming cells, Mesenchymal stem cells, Two-cell spheroid

INTRODUCTION

Blood vessel formation relies on a highly controlled sequence of cellular events. Two fundamental processes by which blood vessels are formed are vasculogenesis and angiogenesis. Vasculogenesis refers to the *de novo* process of new vessel formation by migration and differentiation of endothelial progenitor cells (EPCs) into endothelial cells (ECs), whereas angiogenesis refers to the extension of a pre-existing blood vessels through ECs sprouting and subsequent stabilization by mural cells (Carmeliet, 2000). If either one or both of these processes are dysregulated, a number of pathological conditions can arise (Carmeliet and Jain, 2000).

Drugs that modify angiogenesis hold great promise as potential treatment options for vascular malformation-associated diseases. Many pharmaceutical companies and research institutes have spent considerable effort, time, and money on discovering angiogenesis-modulating drugs. Irrespective of the efforts made, few drugs have entered into the clinical trials. This may be because the preclinical *in vitro* assay systems do not have sufficient sensitivity for identifying potential drug candidates that can effectively modify *in vivo* angiogenic events. Until now, only a handful of drugs, such as Bevacizumab (Avastin, Genentech-Roche, CA, USA) and Sunitinib (Sutent, Pfizer, NY, USA), have been approved for clinical use.

Pro- or anti-angiogenic properties are initially evaluated by *in vitro* assay systems that measure the degree of proliferation, invasion, migration, and tubular structure formation of ECs seeded in two-dimensional (2D) culture dishes. Although these assay systems have contributed significantly to the discovery of angiogenesis modulators, 2D culture systems have some limitations and drawbacks. One of the major limitations of 2D culture systems is loss of originality of cells. For example, 2D-cultured ECs progressively lose their differentiated

Open Access https://doi.org/10.4062/biomolther.2018.134

Received Jul 19, 2018 **Revised** Aug 7, 2018 **Accepted** Aug 8, 2018
Published Online Sep 1, 2018

***Corresponding Author**
E-mail: ktkang@duksung.ac.kr
Tel: +82-2-901-8738, Fax: +82-2-901-8386

In vitro 3D angiogenesis assay using ECFC, MSC, and ECFC+MSC spheroids

Spheroids comprising ECFCs, MSCs, or ECFCs+MSCs were collected, suspended in the corresponding basal medium with 5% FBS (Atlas Biologicals) and 40% methocel (Sigma, MO, USA) to avoid sedimentation of the spheroids. The spheroid suspension was mixed with neutralized collagen solution (Corning, NY, USA) and quickly seeded into pre-warmed 24-well plates followed by polymerization in an incubator. In some experiments, vatalanib was added to the spheroid-containing collagen gel just before seeding. After 30 min of polymerization, 0.1 mL of corresponding basal medium in the presence and absence of pro-angiogenic factors (VEGF or VEGF+FGF-2) was added to the top of the gel. The plate was placed on a real-time cell recorder (JuLI stage; NanoEnTek, Seoul, Korea), which took microscope images of spheroids every 1 h for 24 h automatically. Sprout formation was analyzed by the average number and cumulative length of sprouts from at least five spheroids per group.

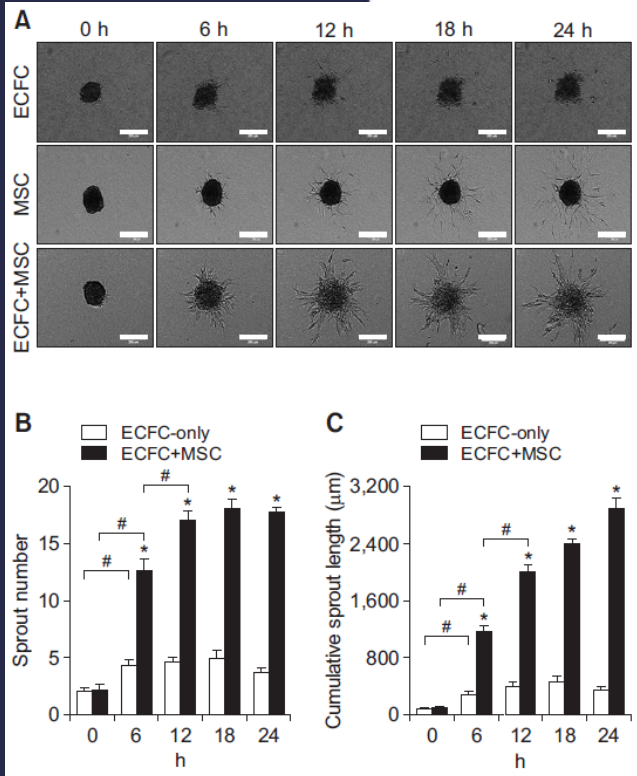

Fig. 1. Comparison of sprout formation between ECFC-only, MSC-only, and ECFC+MSC spheroids. ECFC-only spheroids, MSC-only spheroids, or ECFC+MSC spheroids were embedded in collagen gel and sprout formation was observed by real-time cell recorder every 1 h for 24 h. (A) Representative images of sprouts formed by ECFC-only, MSC-only, or ECFC+MSC spheroids at 0, 6, 12, 18, and 24 h time points (scale bar=250 μm). (B) Analysis of sprout number of ECFC-only or ECFC+MSC spheroids. (C) Analysis of cumulative sprout length of ECFC-only or ECFC+MSC spheroids. *Significant difference ($p \leq 0.05$) between groups. #Significant difference ($p \leq 0.05$) between groups indicated by a bracket (n=3).

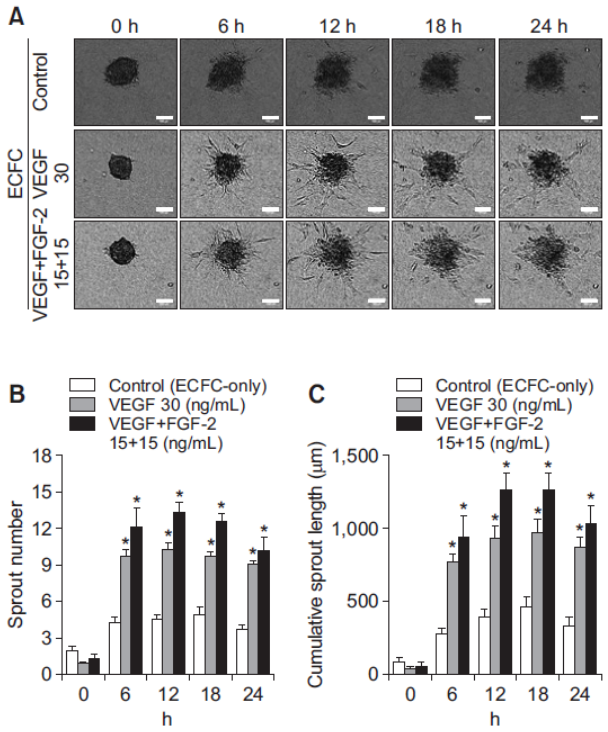

Fig. 2. Effect of exogenous angiogenic factors on sprout formation by ECFC-only spheroids. ECFC-only spheroids were treated with VEGF (30 ng/mL) or VEGF (15 ng/mL)+FGF-2 (15 ng/mL) followed by seeding in a plate. (A) Representative images of sprouts formed by ECFC-only spheroids in the presence and absence of angiogenic factors at 0, 6, 12, 18, and 24 h (scale bar=100 μm). (B) Analysis of sprout numbers of ECFC-only spheroids with/without angiogenic factors. (C) Analysis of cumulative sprout length of ECFC-only spheroids with/without angiogenic factors. *Significant difference ($p \leq 0.05$) from control group (not treated with angiogenic factors) (n=3).

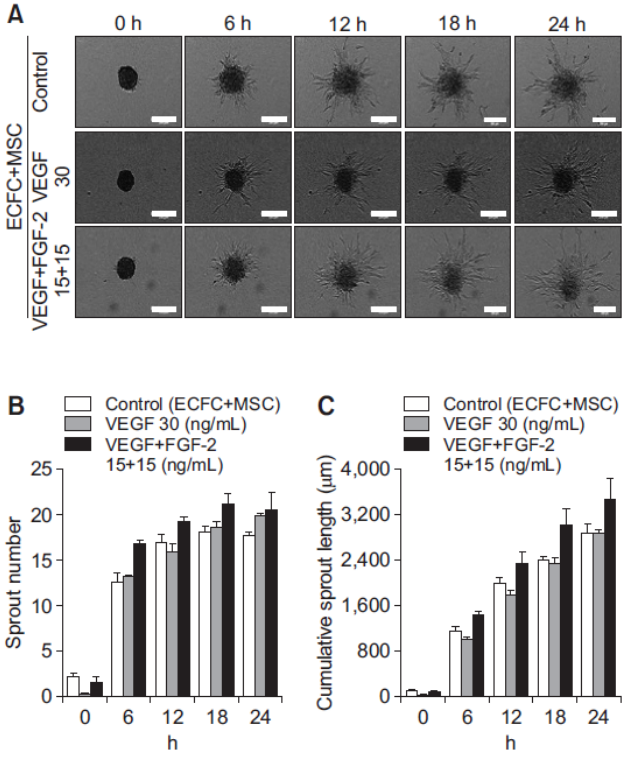

Fig. 3. Effect of exogenous angiogenic factors on sprout formation by ECFC+MSC spheroids. ECFC+MSC spheroids were treated with VEGF (30 ng/mL) or VEGF (15 ng/mL)+FGF-2 (15 ng/mL). (A) Representative images of sprouts formed by ECFC+MSC spheroids in the presence and absence of angiogenic factors at 0, 6, 12, 18, and 24 h (scale bar=250 μm). (B) Analysis of sprout number of ECFC+MSC spheroids with/without angiogenic factors. (C) Analysis of cumulative sprout length of ECFC+MSC spheroids with/without angiogenic factors (n=3).

JuLI™ Stage

Real-time live cell imaging system

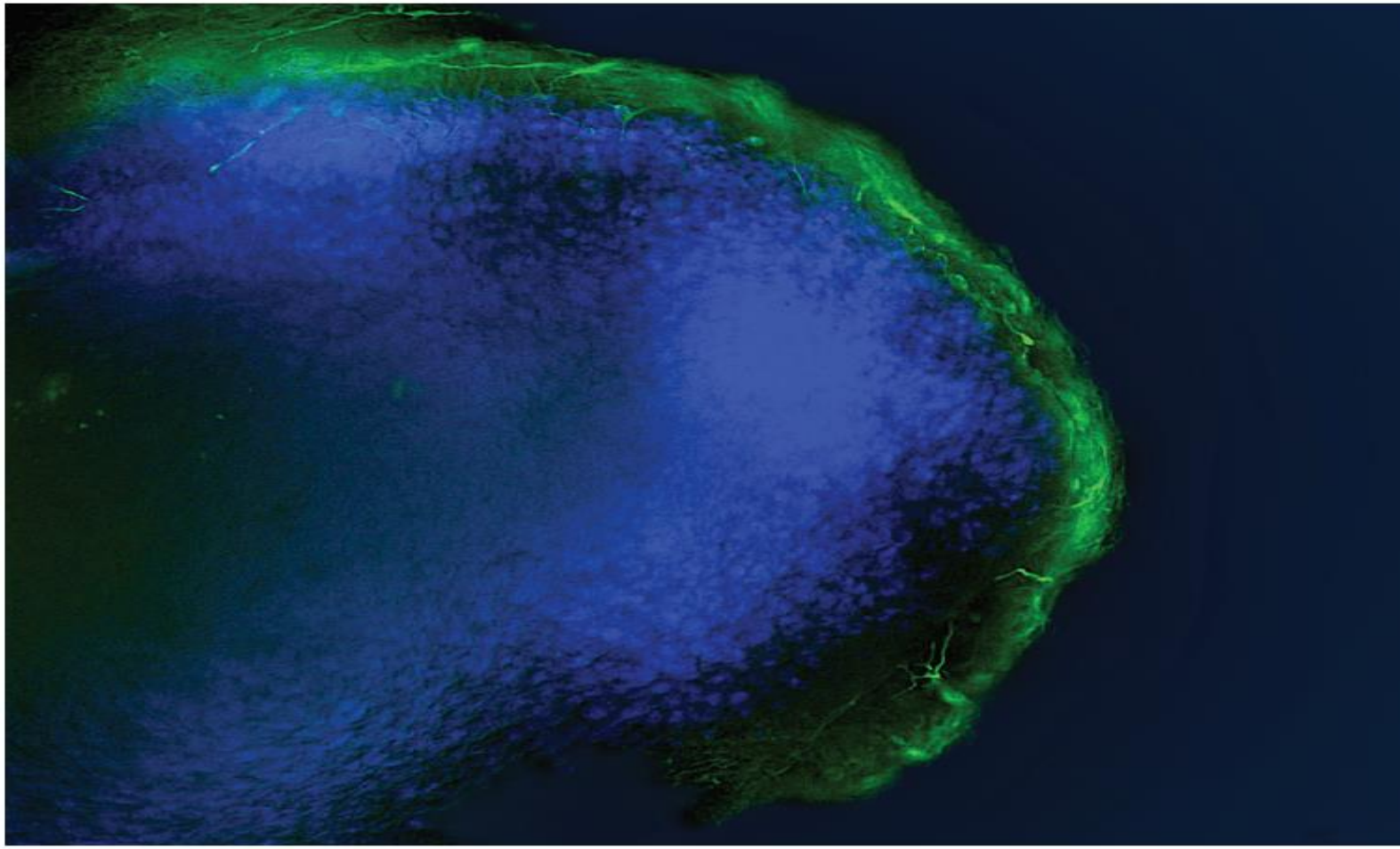

NanoEnTek

NESCT-RJST-001E (V.0.0)

NanoEnTek, Inc.
851-14, Seohae-ro, Paltan-myeon, Hwaseong-si, Gyeonggi-do, 18531, Korea
Tel : +82-2-6220-7940 / Fax : +82-2-6220-7999

NanoEnTek, Inc. (USA)
240 Bear Hill Road, Suite 101, Waltham, MA 02451, USA
Tel : +1-781-472-2558 / Fax : +1-781-790-5649

Email
sales@nanoentek.com

Website
www.julistage.com
www.nanoentek.com